Optical Characterization of Plasmonic Anisotropic Nanostructures by Modeling and Spectroscopic Verification

Stefan Stoenescu

A Thesis

in

the Department

of

Mechanical and Industrial Engineering

Presented in Partial Fulfillment of the Requirements

For the Degree of Doctor of Philosophy at

Concordia University

Montreal, Quebec, Canada

December 2013

Examining committee:

Chair:	Prof. Yuhong Yan
External:	Prof. Pandurang Ashrit:
Co-Supervisor:	Prof. Muthukumaran Packirisamy:
Co-Supervisor:	Prof. Vo-Van Truong:
Examiner:	Prof. Rama Bhat:
Examiner:	Prof. Saifur Rahaman:
Examiner:	Prof. Rolf Wüthrich:

ABSTRACT

Optical Characterization of Plasmonic Anisotropic Nanostructures through Modeling and Spectroscopic Verification

This thesis attempts to characterize the optical properties of plasmonic anisotropic nanostructures through modeling and verification. Two nanostructures with important applications are selected for characterization. First, uniaxially aligned gold nanorods (AuNRs) embedded in polyvinyl alcohol (PVA) films are realized by determining suitable heating conditions during stretching, using PVA of high molecular weight mixed with plasticizer to improve the plastic deformability, and stretching the composite film. A high stretch ratio of seven is attained and the induced alignment of the rods is quantified statistically by an order parameter of 0.92 and an average angle of 3.5°. The stretched composite film is shown to have dichroic optical properties, which confirmed the good alignment. Since the statistical quantification requires destructive examinations, a novel non-destructive method is developed based on a probabilistic approach, computational simulations, and spectrometric measurements. The new method yields results in agreement with the statistical method and applies to all dichroic particles. The second nanostructure is a gold nanostar (AuNS) – polydimethylsiloxane (PDMS) composite platform. This nanostructure is characterized by using a typical AuNS of average dimensions and idealized as consisting of a sphere and radially oriented truncated cones representing its core and branches. Using branches defined parametrically by their number, length, aperture angle and orientation, and gradually attaching branches to a core, their ensemble spectra of increasing complexity are simulated. The absorptive contribution of each component is analyzed, demonstrating the large tunability of the

AuNS and allowing for finding the most effective way to tune its fundamental resonant excitation. Using plasmon hybridization theory, the plasmonic interaction between structural elements is demonstrated in three different geometries.

This thesis is dedicated to my family,

for having always supported me

ACKOWLEDGEMENTS

At this point along my journey towards specializing in the fascinating field of nanophysics, I feel greatly indebted and I am expressing my deep gratitude in chronological order: to Professor Greene, for his Pulitzer prize finalist book “The Elegant Universe” introducing the string theory, which has unveiled the beauty of physics at scales even smaller than the nanoscale and has incited my interest; to Professor Packirisamy, my co-supervisor who has offered me the opportunity to start the journey in the first place and who has also suggested to concentrate on nanorods; to Professor Vo-Van, my co-supervisor, whose advice has shown me the direction to go at crossroads while giving me the perfect freedom of thinking in the same time; to Dr. Badilescu, whose advice in my first spectroscopic measurements and synthesis of nanoparticles was very helpful; to Professor Wüthrich, for his time, kind attention and advice in statistics; to Ms. MacDonald, physicist of the “Centre for Characterization and Microscopy of Materials” whose successful imaging of my samples of nanorods embedded in polymer has added great value to my thesis; to Dr. Xu of RSoft Design Group Inc. for his specialist advice in modeling of nanostructures; to Dr. Pottier for practical advice on using RSoft and interesting discussions in physics; finally and equally importantly to my colleagues: Mahmood Ghanbari, Jayan Ozhikandathil, Hamid SadAbadi, Amir Sanati Nezhad and Carlos Agudelo with whom I shared laboratory equipment, always helping each other in a motivating and joyful atmosphere.

CONTENTS

List of figures …… …… xi

List of tables……..…… xvii

List of illustrations…… xviii

Nomenclature …… xxiv

Chapter 1. Introduction and Overview…… 1

1.1. Introduction ……..…….. 1

1.2. Introductory nomenclature and selection criteria ……. 2

1.2.1. Application example 1: Optical limiter …….. 4

1.2.2. Application example 2: Biosensor. …… 8

1.3. Research objectives …….. 10

1.4. Overview of the remaining chapters……..…….. 10

Chapter 2. Theoretical background …… ……. 14

2.1. Electronic structure of metals ……14

2.2. The dielectric function ……. 17

2.2.1. The Drude-Lorentz classical model …….. 18

2.2.2. Comparison with experimental data …….. 20

2.3. Surface plasmon resonance (SPR) …….. 21

2.4. The size and shape adaption of dielectric function ……..24

2.5. Material selection …… 25

2.5.1. Chemical neutrality …… …….. 26

2.5.2. Chemical binding despite general nonreactivity …….. 27

2.5.3. Excitation of SPR in the VIS-NIR region ……. 27

2.5.4. Ongoing research on cell toxicity of AuNRs ……..…….. 28

2.6. Polarization of light …….. 28

2.6.1. Polarizer …….. 30

2.6.2. Dichroism …… 30

2.7. Numerical simulations of optical properties ……. 31

2.7.1. Governing equations and computation scheme …….. 32

2.7.2. The computation grid and boundary conditions ……. 34

Chapter 3. Aligned gold nanorods - Improving the matrix of the composite film .. 36

3.1. Introduction…….. 36

3.2. Review of aligning methods…… 37

3.3. Improving the plastic deformability…… … 38

3.4. Experimental – film preparation…… …… 40

3.5. Assessing the alignment of the AuNRs ……..…… 41

Chapter 4. Aligned gold nanorods - Characterization of the composite film…… 44

4.1. Introduction……...… 44

4.2. Temperature threshold ……...…….. 45

4.3. Characterization ……..……. 47

4.3.1. Statistically significant sample and average orientation angle 47

4.3.2. Optical characterization: dichroism ……. 50

4.3.3. Optical characterization: deviations from dichroism …….. 56

4.4. Numerical simulations ……. 58

4.4.1. Mesh convergence ……..…… 58

4.4.2. Size & shape adapted dielectric function …… .60

4.5. Device for stretching polymer films ……..…….. 61

Chapter 5. Aligned gold nanorods-Non-Destructive Quantification of Alignment.. 63

5.1. Introduction ……. 63

5.2. The non-destructive quantification method …….. 65

5.2.1. Qualitative understanding of the peak broadening ……. 65

5.2.2. Simplifying assumptions …….. 68

5.2.3. A unified probabilistic approach ……. 70

5.2.4. Problem formulation and its solution ……. 73

5.2.5. Implementation of the method for the discretized problem …. 78

a. Parameters defining the Gaussian distribution ……. 78

b. Discretization of the domain …….…… 79

c. Solving for the average orientational angle $\bar{\Phi}$ …… 79

i) Using the dielectric function of the bulk material …….. .80

ii) Using the dielectric function adapted for size and shape .. 84

d. Alternative faster graphical method of solving for B …….. 87

5.3. Summary and conclusions ……. 89

Chapter 6. Optical properties of gold nanostar-PDMS composite ……. 93

6.1. Introduction. ……...…… 93

6.2. Selection of the numerical method …… 96

6.3. The numerical solution and boundary conditions …… 99

6.4. Mesh convergence study …… …… 100

6.5. Results and discussion …….. 103

6.5.1. The “sphere-only” model, labeled “S”. ……..….. 103

6.5.2. The sphere and one branch model “S1B” …… 103

6.5.2.1. Influence of branch length. ……..…… …… 103

6.5.2.2. Influence of branch aperture …… 104

6.5.3. Influence of number (N) and orientation of the branches ….. 105

6.5.4. The tunability of AuNSs optical response ……109

6.5.5. Interaction of plasmons ……111

Chapter 7. Conclusions and suggestions for future work ……..……..116

7.1. Summary ……...116

7.2. Conclusions …….. 118

7.3. Suggestions for further research …… ……119

7.4. Contributions ……121

Appendix A: The size and shape adapted dielectric functions ……124

Appendix B: The cosine-squared law ……..126

References ……128

List of Figures

FIG.1.1 Ranges of electromagnetic spectrum where the SPR of nanoshells and the transverse and longitudinal SPR of the nanorods can be geometrically tuned.

FIG.1.2 (a) Ideal and real curves of transmitted vs. input energy of an optical limiter (b) Ideal and real curves of transmittance vs. input energy of an optical limiter

FIG. 1.3 Schematic of experimental set-up for testing the non-linear absorption (NLA) of a AuNRs-PVA composite film

FIG. 2.1 Comparison between the dielectric function calculated using equations (2.7 a & b) of the Drude-Lorentz model (continuous lines) and experimental data [Johnson & Christy, 1972] (marked by "plus" and "square" signs) for bulk gold.

FIG. 2.2 Bulk plasmon in a metal slab

FIG. 2.3 (a) propagating surface plasmon polariton (b) localized surface plasmon polariton

FIG. 2.4 Schematic showing the principle of non-uniform grid used to compute the properties of a one-branch nanostar 3D-model. The grid actually used was much finer, but it has been coarsened for clarity. The nanostructure is excited by a wavelight that is emitted from the launch pad, drawn in blue color. The monitor is shown as the black line rectangle and the PML as the outer gray strip.

FIG. 3.1 Normalized absorbance spectra of uniaxially stretched AuNR-PVA film illuminated by plane polarized light with the electric field parallel (E||) and perpendicular to the s' – s direction. (b) Linear trend of the dichroic ratio dependence on the stretch ratio.

FIG. 4.1 Absorbance spectra of AuNRs in aqueous solution and embedded in unstretched PVA film under different annealing conditions

FIG. 4.2 (a) SEM micrograph of a AuNR-PVA film stretched along the stretch axis (SA), depicted by the double-headed arrow. (b) Histogram of orientation angles Insets: (i) Spherical NP likely to have been formed by thermal reshaping of a AuNR or as a synthesis byproduct (ii) Definition of the orientational angle φ

FIG.4.3 Absorbance spectra. Uppermost: spectrum of unstreched film, shifted vertically for better visibility; middle and bottom: spectra of stretched film for different polarization angles θ (defined in FIG.4.4). Inset (i): schematic of the experimental set-up.

FIG.4.4 FDTD-simulated absorbance spectra of a single AuNR**. Insets:** (i) FDTD 3D-model, coated with surfactant. (ii) scaled-up TSPR absorbance peak.

FIG.4.5 (a) Experimental set-up. (b) Measured absorbance spectra at L- and TSPR wavelengths matched with the theoretical cosine-squared law, in cartesian coordinates and in (c) polar coordinates (d) Matching of simulated absorbance spectrum at LSPR peak wavelength with the theoretical cosine-squared law.

FIG.4.6 Schematic of a plane polarized light wave incident on the composite film at an angle θ with respect to the transmission axis (TA) of the film. TA is perpendicular to the stretch axis SA.

FIG.4.7 Mesh convergence: change of LSPR wavelength and intensity relative to their average of all iterations plotted with respect to the size of the edge grid.

FIG.4.8 Effect of size and shape of the NPs on the refractive and extinction coefficients of gold: bulk (black line, no marker), size-adapted (blue line, diamond marker). (a) refractive index (b) extinction coefficient.

FIG.4.9 (a) Exploded drawing of the device for stretching polymer films (b) Photograph of a stretched AuNR-PVA composite film still clamped in the device and allowed to dry at room temperature for 24 hours.

FIG. 5.1 (a) Micrograph component of the statistical significant sample (SSS). Inset (i) Schematic of typical AuNRs and definition of the orientation angle φ with respect to the stretch axis SA of the film. (b) Histogram of the orientation angles of the AuNRs measured based on micrographs of the SSS.

FIG. 5.2 (a) Polarized absorbance spectra of the reference stretched AuNR-PVA composite film. The angles θ and φ indicate the direction of polarization of the incident light beam and the orientation of a typical rod with respect to the SA of the film, respectively. (b) The measured LSPR spectrum for parallel polarization θ=0° superimposed on simulated spectra for two dielectric functions: of the bulk gold (asterisk marked black line) and size & shape adapted (blue thin line)

FIG. 5.3 Definition of interval centered at the average alignment angle of the rods used in the averaging of the total probability with respect to the orientational angle.

FIG. 5.4 Schematic of atomic transitions taking place within each illuminated AuNR: absorption of photons resulting in the excitation of the atoms by followed by their relaxation by spontaneous emission of photons. The emitted photons are captured superimposed on each other by the detector, which is recorded as an absorption

spectrum. The index k is associated with each illuminated nanorod, all assumed to lie far apart from each other such that not to interact electromagnetically.

FIG. 5.5 Simulated absorbance spectrum of an ensemble of AuNRs for the bulk dielectric function and B=1. (a) Normalized spectra of the seven categories of rods, denoted by their aspect ratios "η". (b) The Gaussian weights assigned to each η-category. (c) The spectra of panel (a) weighted by Gaussian weights. The spectrum of the ensemble, the blue dash-dotted line, was obtained by summing up the weighted spectra according to the definition relationship (14b).

FIG. 5.6 Two equivalent representations of ensemble spectra y0(λ,B) defined by (15) for $0 \leq B \leq 1$ and the bulk dielectric function of gold. (a) The peaks of the spectra are both allowed to vary with B. (b) The same y0 spectra of (a) translated and scaled in the y-direction to match the baseline and the peak of the experimental spectrum.

FIG. 5.7 (a) Normalized spectra of the seven categories of rods simulated for the size & shape adapted dielectric function using $\alpha = 0.33$ and B=1. (b) Gaussian weights assigned to each η-category. (c) Absorbance spectrum (dash-dotted line) of the rod ensemble.

FIG. 5.8 Equivalent absorbance spectra of the rod ensemble for the corrected dielectric function of gold, using $\alpha = 0.33$ (a) The peak and the width of the spectrum are both allowed to vary with B. (b) The same spectra translated and scaled in the y-direction to match the LSPR baseline and peak of the composite film.

FIG. 5.9 Graphically solving for B using the FWHM of the composite film and polydispersity of the rods.

FIG. 5.10 Schematic of main steps in solving the discretized equations for the average orientation angle of the ensemble of AuNRs

FIG. 5.A.1 (a) Bulk and corrected refractive index. (b) Extinction coefficient of gold.

FIG. 6.1 Microscopic image of AuNS - PDMS composite

FIG. 6.2 Components and definition of parameters used for the 3D model of an AuNS of average dimensions

FIG. 6.3 Mesh convergence study for the bulk domain: (a) Absorbance spectra for grid sizes 10, 7.5, 6 and 5 nm. (b) Change of the SPR peak wavelength as a function of the grid size.

FIG. 6.4 Mesh convergence study for the metal-dielectric interface region. (a) Not normalized absorbance spectra for grid size of the edge 1.25 and 1.0 nm. (b) Change of the SPR peak wavelength as a function of the grid size.

FIG. 6.5 Simulated absorbance spectra normalized with respect to the SPR wavelength of the spherical core.

FIG. 6.6 Absorbance spectra of the S1B models, semi-aperture angle $\alpha=10°$ and branch lengths L = 100 dotted/green curve, L=125 short-dashed/blue curve and L=150 nm long-dashed/red curve, normalized with respect to the peak intensity of the S model. The spectrum of the spherical core is included as the curve S for reference.

FIG. 6.7 Influence of the number of branches in two illumination cases inset (i) & (ii)

FIG. 6.8 Two experimental spectra of AuNSs embedded in PDMS composite prepared with two porogens

FIG. 6.9 Shift of peak wavelength of the second SPR mode (of the branch) with respect to the first SPR mode (of the sphere) for two cases: a) variable branch length

at constant aperture (α = 3° and α = 10°) and b) variable branch aperture at constant length (L = 100 nm)

FIG. 6.10 The energy level diagram of the hybridization theory of plasmons.

FIG. 6.11 Energy diagram of plasmon interaction in AuNS, model S1B where the branch parameter values are α=3°, L=100 nm and the electric field is parallel to the branch.

FIG. 6.12 Energy diagram of plasmon interaction in AuNS, model S1B where the branch parameter values are α=3°, L=125 nm and the electric field is parallel to the branch.

FIG. 6.13 Energy diagram of plasmon interaction in AuNS, model S1B where the branch parameter values are α=3°, L=125 nm and the electric field is parallel to the branch.

List of tables

Table 4.1 Coefficients defining the dependence relationship (4.3) of the peak wavelength of a AuNR on its aspect ratio

Table 5.1 Measured FWHM values for given polydispersities and values of the parameter B

Table 5.2 Adequacy of second vs. first order fitting polynomials

Table 5.A1 Line markers used in FIG. 5.A1 for dimensional categories "η"

Table 6.1 Values used for the geometric parameters defining the morphology of a AuNS simulation model

List of illustrations

FIG.1.1 Ranges of electromagnetic spectrum where the SPR of nanoshells and the transverse and longitudinal SPR of the nanorods can be geometrically tuned.

FIG.1.2 (a) Ideal and real curves of transmitted vs. input energy of an optical limiter (b) Ideal and real curves of transmittance vs. input energy of an optical limiter

FIG. 1.3 Schematic of experimental set-up for testing the non-linear absorption (NLA) of a AuNRs-PVA composite film

FIG. 2.1 Comparison between the dielectric function calculated using equations (2.7 a & b) of the Drude-Lorentz model (continuous lines) and experimental data [Johnson & Christy, 1972] (marked by "plus" and "square" signs) for bulk gold.

FIG. 2.2 Bulk plasmon in a metal slab

FIG. 2.3 (a) propagating surface plasmon polariton (b) localized surface plasmon polariton

FIG. 2.4 Schematic showing the principle of non-uniform grid used to compute the properties of a one-branch nanostar 3D-model. The grid actually used was much finer, but it has been coarsened for clarity. The nanostructure is excited by a wavelight that is emitted from the launch pad, drawn in blue color. The monitor is shown as the black line rectangle and the PML as the outer gray strip.

FIG. 3.1 Normalized absorbance spectra of uniaxially stretched AuNR-PVA film illuminated by plane polarized light with the electric field parallel (E||) and perpendicular to the s' – s direction. (b) Linear trend of the dichroic ratio dependence on the stretch ratio.

FIG. 4.1 Absorbance spectra of AuNRs in aqueous solution and embedded in unstretched PVA film under different annealing conditions

FIG. 4.2 (a) SEM micrograph of a AuNR-PVA film stretched along the stretch axis (SA), depicted by the double-headed arrow. (b) Histogram of orientation angles Insets: (i) Spherical NP likely to have been formed by thermal reshaping of a AuNR or as a synthesis byproduct (ii) Definition of the orientational angle φ

FIG.4.3 Absorbance spectra. Uppermost: spectrum of unstreched film, shifted vertically for better visibility; middle and bottom: spectra of stretched film for different polarization angles θ (defined in FIG.4.4). Inset (i): schematic of the experimental set-up.

FIG.4.4 FDTD-simulated absorbance spectra of a single AuNR**. Insets:** (i) FDTD 3D-model, coated with surfactant. (ii) scaled-up TSPR absorbance peak.

FIG.4.5 (a) Experimental set-up. (b) Measured absorbance spectra at L- and TSPR wavelengths matched with the theoretical cosine-squared law, in cartesian coordinates and in (c) polar coordinates (d) Matching of simulated absorbance spectrum at LSPR peak wavelength with the theoretical cosine-squared law.

FIG.4.6 Schematic of a plane polarized light wave incident on the composite film at an angle θ with respect to the transmission axis (TA) of the film. TA is perpendicular to the stretch axis SA.

FIG.4.7 Mesh convergence: change of LSPR wavelength and intensity relative to their average of all iterations plotted with respect to the size of the edge grid.

FIG.4.8 Effect of size and shape of the NPs on the refractive and extinction coefficients of gold: bulk (black line, no marker), size-adapted (blue line, diamond marker). (a) refractive index (b) extinction coefficient.

FIG.4.9 (a) Exploded drawing of the device for stretching polymer films (b) Photograph of a stretched AuNR-PVA composite film still clamped in the device and allowed to dry at room temperature for 24 hours.

FIG. 5.1 (a) Micrograph component of the statistical significant sample (SSS). Inset (i) Schematic of typical AuNRs and definition of the orientation angle φ with respect to the stretch axis SA of the film. (b) Histogram of the orientation angles of the AuNRs measured based on micrographs of the SSS.

FIG. 5.2 (a) Polarized absorbance spectra of the reference stretched AuNR-PVA composite film. The angles θ and φ indicate the direction of polarization of the incident light beam and the orientation of a typical rod with respect to the SA of the film, respectively. (b) The measured LSPR spectrum for parallel polarization θ=0° superimposed on simulated spectra for two dielectric functions: of the bulk gold (asterisk marked black line) and size & shape adapted (blue thin line)

FIG. 5.3 Definition of interval centered at the average alignment angle of the rods used in the averaging of the total probability with respect to the orientational angle.

FIG. 5.4 Schematic of atomic transitions taking place within each illuminated AuNR: absorption of photons resulting in the excitation of the atoms by followed by their relaxation by spontaneous emission of photons. The emitted photons are captured superimposed on each other by the detector, which is recorded as an absorption

spectrum. The index k is associated with each illuminated nanorod, all assumed to lie far apart from each other such that not to interact electromagnetically.

FIG. 5.5 Simulated absorbance spectrum of an ensemble of AuNRs for the bulk dielectric function and B=1. (a) Normalized spectra of the seven categories of rods, denoted by their aspect ratios "η". (b) The Gaussian weights assigned to each η-category. (c) The spectra of panel (a) weighted by Gaussian weights. The spectrum of the ensemble, the blue dash-dotted line, was obtained by summing up the weighted spectra according to the definition relationship (14b).

FIG. 5.6 Two equivalent representations of ensemble spectra y0(λ,B) defined by (15) for $0 \leq B \leq 1$ and the bulk dielectric function of gold. (a) The peaks of the spectra are both allowed to vary with B. (b) The same y0 spectra of (a) translated and scaled in the y-direction to match the baseline and the peak of the experimental spectrum.

FIG. 5.7 (a) Normalized spectra of the seven categories of rods simulated for the size & shape adapted dielectric function using $\alpha = 0.33$ and B=1. (b) Gaussian weights assigned to each η-category. (c) Absorbance spectrum (dash-dotted line) of the rod ensemble.

FIG. 5.8 Equivalent absorbance spectra of the rod ensemble for the corrected dielectric function of gold, using $\alpha = 0.33$ (a) The peak and the width of the spectrum are both allowed to vary with B. (b) The same spectra translated and scaled in the y-direction to match the LSPR baseline and peak of the composite film.

FIG. 5.9 Graphically solving for B using the FWHM of the composite film and polydispersity of the rods.

FIG. 5.10 Schematic of main steps in solving the discretized equations for the average orientation angle of the ensemble of AuNRs

FIG. 5.A.1 (a) Bulk and corrected refractive index. (b) Extinction coefficient of gold.

FIG. 6.1 Microscopic image of AuNS - PDMS composite

FIG. 6.2 Components and definition of parameters used for the 3D model of an AuNS of average dimensions

FIG. 6.3 Mesh convergence study for the bulk domain: (a) Absorbance spectra for grid sizes 10, 7.5, 6 and 5 nm. (b) Change of the SPR peak wavelength as a function of the grid size.

FIG. 6.4 Mesh convergence study for the metal-dielectric interface region. (a) Not normalized absorbance spectra for grid size of the edge 1.25 and 1.0 nm. (b) Change of the SPR peak wavelength as a function of the grid size.

FIG. 6.5 Simulated absorbance spectra normalized with respect to the SPR wavelength of the spherical core.

FIG. 6.6 Absorbance spectra of the S1B models, semi-aperture angle $\alpha=10°$ and branch lengths L = 100 dotted/green curve, L=125 short-dashed/blue curve and L=150 nm long-dashed/red curve, normalized with respect to the peak intensity of the S model. The spectrum of the spherical core is included as the curve S for reference.

FIG. 6.7 Influence of the number of branches in two illumination cases inset (i) & (ii)

FIG. 6.8 Two experimental spectra of AuNSs embedded in PDMS composite prepared with two porogens

FIG. 6.9 Shift of peak wavelength of the second SPR mode (of the branch) with respect to the first SPR mode (of the sphere) for two cases: a) variable branch length

at constant aperture (α = 3° and α = 10°) and b) variable branch aperture at constant length (L = 100 nm)

FIG. 6.10 The energy level diagram of the hybridization theory of plasmons.

FIG. 6.11 Energy diagram of plasmon interaction in AuNS, model S1B where the branch parameter values are α=3°, L=100 nm and the electric field is parallel to the branch.

FIG. 6.12 Energy diagram of plasmon interaction in AuNS, model S1B where the branch parameter values are α=3°, L=125 nm and the electric field is parallel to the branch.

FIG. 6.13 Energy diagram of plasmon interaction in AuNS, model S1B where the branch parameter values are α=3°, L=125 nm and the electric field is parallel to the branch.

Nomenclature

α = the linear coefficient of absorption,

β - the two photon absorption coefficient

γ – collision frequency of electrons

δ - size of edge grid at phase interface

Δ - grid size for bulk domain

η – aspect ratio of nanorod

ε - dielectric function

ε_0 - permittivity of vacuum

$\chi^{(i)}$ - material susceptibility of order "i"

λ_{deB} - de Broglie wavelength

μ - permeability of the material

μ_0 - permeability of vacuum

σ_{ex} - absorption cross section of the excited state

$\boldsymbol{\tau}$ – relaxation time (between two cp or eben teo;;isioj

ω – angular frequency

ω_0 - natural angular frequency an oscillator

ω_P –plasma frequency

b - damping coefficient due to electron collisions

c – speed of light in vacuum

e - electric charge of an electron

h – Planck's constant

k_B – Boltzmann's constant

k_{SHO} - spring stiffness of an oscillator

{h,k,l} - denotes a family of equivalent crystallographic planes, where h, k and l are Miller indices

m - effective mass of an electron

nm – nanometer or 10^{-9} m

x - electron displacement from equilibrium

B - magnetic induction

D - dielectric displacement

E - electric field

$\mathbf{E_L}$ - threshold of linear transmission

$\mathbf{E_D}$ - irreversible damage of the limiter

$\mathbf{E_{max}}$ - irreversible damage to receiver

$\mathbf{E_T}$ - transmitted energy

$\mathbf{E_0}$ - incident energy

H - magnetic field

I - irradiance;

K - wave vector

N – number density of electrons

N_{ex} = population density of the excited state

P – polarization

S – surface area of nanoparticle

T - transmittance = $(E_T/E_0)^2$; also absolute temperature (depending on context)

T_{min} - minimum transmittance

V – volume

V_C – volume of a crystal cell

Acronyms

ABC - absorbing boundary conditions

B – branch model of a nanostar

CTAB - cetyl trimethylammonium bromide, used in synthesis of nanoparticles

EM - electromagnetic

FWHM – full width half maximum

NIR – near infrared

NLA - non-linear absorption

NP – nanoparticle or particles of size in the 1-200 nm range

NR - nanorod

NS - nanostar

OL – optical limiter or limiting

PML - perfectly matched layer

PDMS – polydimethylsiloxane is a polymeric organo-silicon compound

S –spherical core model of a nanostar

S1B – NS model of sphere & one branch

S2B – NS model of sphere & two branches

SHO – single harmonic oscillator

SPR – surface plasmon resonance

LSPR - longitudinal SPR

TSPR - transverse SPR

VIS – visible range electromagnetic radiation: 390-770 nm wavelength

1. Introduction and Overview

Chapter outline

1.1. Introduction
1.2. Introductory nomenclature and selection criteria
    1.2.1. Optical limiter. Application example 1
    1.2.2. Biosensor. Application example 2
1.3. Research objectives
1.4. Overview of the remaining chapters

1.1. Introduction

In general lines, the main interest pursued in this research was light-matter interaction under the particular aspect of light-metal interaction at the nanometer (nm) scale, that is, the size of the illuminated object was of the 10^{-9} m order of magnitude.

More precisely, the focus was on the development and optical characterization through spectroscopic measurements and numerical simulations of two nanostructures based on one of the most tunable nanoparticle (NP) that has been synthesized so far, namely a nanorod (NR). The first nanostructure was a composite film consisting of uniaxially aligned gold nanorods (AuNRs) embedded in a polymer film, which has potential applications in optical limiting. The second nanostructure was a gold nanostar (AuNS) embedded in polydimethyl siloxane (PDMS), or a nanostructure resembling a star, which through its rod-like branches inherits the advantageous geometric tunability of the NRs and has potential applications in biosensing.

The presentation of the results starts with a brief introduction of some of the terms common in this field and the motivation behind my selection of these nanostructures.

1.2. Introductory nomenclature and selection criteria

The response of metallic nanoparticles (NPs) to light illumination defines their optical properties and plays an essential role in many different types of applications such as photonics (Wang, Teitel & Dellago, 2005), data encoding (Zijlstra, Chon, & Gu, 2009) optical limiting (Zhu, Bai, Zhao, & Li, 2009), biosensing (Willets & van Duyne, 2007), diagnostics and therapeutics (Zhang, Wang, & Chen, 2013).

Light illumination of gold nanoparticles (AuNPs) sets their conduction electrons into collective and coherent oscillation localized at the surface of the particle. When the incident light provides the exact energy difference between two of the quantized states of the atoms, the illuminated atoms absorb photons and jump to correspondingly higher energy levels, as assumed by the quantum theory of radiation. This transfer of energy from the incident electromagnetic (EM) field to the NPs defines a resonant interaction, also known as localized surface plasmon resonance (SPR) to differentiate it from a propagating SPR at a plane metallic surface. The localized SPR is characterized by a highly enhanced electric field inside and outside the particle while its intensity can be recorded by a spectrophotometer as a local maximum on a spectrum of absorption.

Besides the dielectric properties of the metal and of the surrounding medium, shape and size of NPs are important factors that control the peak wavelength and width of the localized SPR. The influence of shape becomes evident for NPs much smaller than the wavelength of the incident irradiation, which may be an actual or assumed condition known as the electrostatics approximation or quasistatics. Under this condition, a spherical NP can be resonantly excited in only one dipolar mode because of its high order symmetry while an optically anisotropic NP, such as a nanorod (NR), can be excited in

two dipolar SPR modes: a longitudinal (LSPR) and a transverse (TSPR) mode depending on the polarization of the incident electric field, parallel or perpendicular to the long-axis of the NR, respectively (Perez-Juste, Pastoriza-Santos, Liz-Marzan, & Mulvaney, 2005). From the application standpoint, the LSPR mode is more useful because its peak wavelength can be tuned by adjusting the aspect ratio of the rods, from mid-visible to near-infrared (NIR), which is a much larger tunability range than the range of the TSPR peak wavelength.

Tunability in the NIR interval of radiation is especially useful and has become a required property of the NPs used in biomedical applications, because in this region biological tissue and cells absorb light energy below damaging levels, which allows for the irradiation of the NPs to fulfill their intended role. Although other NPs, such as nanoshells, also have a similarly large tunability, as seen in FIG. 1.1, NRs are much more readily synthesized in batch with controlled geometry and high yield. In addition, they also have five geometric factors to adjust their peak absorption wavelength, as follows: aspect ratio, particle volume, end cap profile, convexity of waist and convexity of ends (Mohr, 2009). For this reason, a gold nanorod has been selected as the generic structural element of the nanostructures for this work.

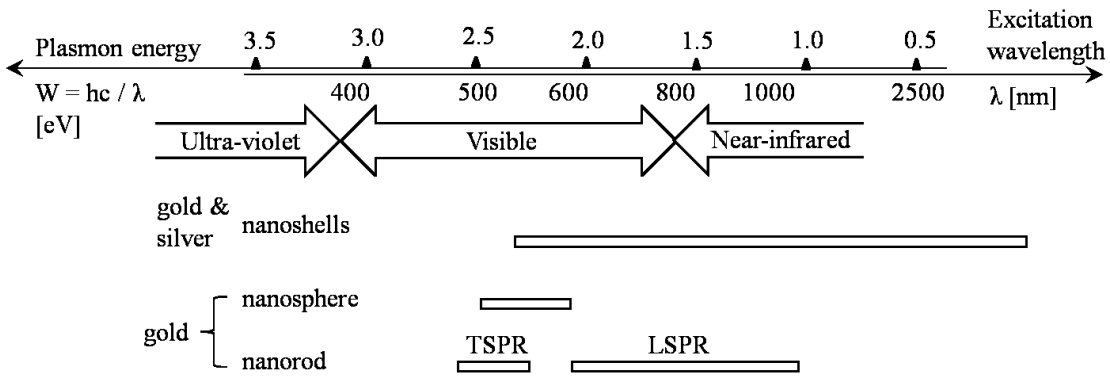

FIG. 1.1 Ranges of electromagnetic spectrum where the SPR of nanoshells and the transverse and longitudinal SPR of the nanorods can be geometrically tuned - adapted from (Steele, 2007).

Depending on the application, the constituent NPs of a nanostructure may be required to have specific optical properties, such as:

a) tunability of the SPR peak wavelength in a certain region, to allow for excitation at a well defined wavelength;

b) specific arrangement of the NPs within the nanostructure to allow for their individual or simultaneous excitation,

The following two examples are presented to clarify why these properties are necessary:

1.2.1. **Application example 1**: **Optical limiter**

An optical limiting device is a light receiver, the first in a sequence of subsystems that make up an optical system. The role played by an optical limiter is to take in light, assess and adjust its intensity and transmit only beams of intensity below a given allowable threshold in order protect the rest of the system that may be composed of sensitive optical instruments, such as the human eye, against light of excessive intensity, such as laser light. The ideal energy modulation of the transmitted light is plotted in the following diagram FIG. 1.2 from Hagan (2010):

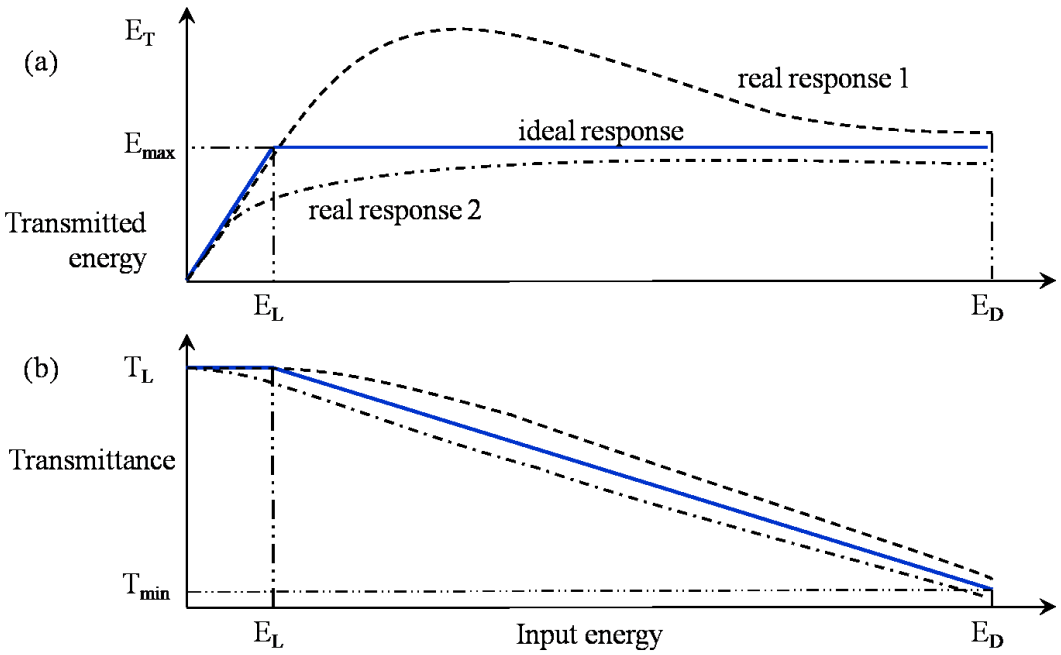

FIG. 1.2 (a) Ideal and real curves of transmitted vs. input energy of an optical limiter (b) Ideal and real curves of transmittance vs. input energy of an optical limiter – adapted from (Hagan, 2010)

where

E_L - threshold of linear transmission

E_D - irreversible damage of the limiter

E_{max} - irreversible damage to receiver

E_T - transmitted energy

E_0 - incident energy

T - transmittance = $(E_T/E_0)^2$

T_{min} - minimum transmittance

Two potential design solutions to this problem exist, as follows:

a) **An active system** consisting of a sensor that senses the power of the incident light which through a processor triggers a shutter or a modulator to control the transmitted power within allowable limits. Among the known systems, the human iris and the blink

mechanism have a duration of the response of about 0.1 seconds, which is too slow since it allows a pulse of light shorter than 0.1 s to be transmitted and damage the iris if the pulse intensity is high enough. The critical issue is the response speed, because the fastest electro-optic shutters are limited to about 1 ns, which is still not sufficient to guard against ultrafast intense pulses. Besides not being fast enough, the active systems also have the disadvantage of complexity and cost.

b) **A passive system** that would include a material able to absorb light linearly up to a threshold E_L that also defines the maximum transmitted energy E_{max} that the receiver can accept without suffering irreversible damage. Beyond this threshold the rate of absorption needs to increase much higher as a function of the of the incident light intensity. Therefore this material would need to have nonlinear optical properties reaching a large enough absorption rate in order to ensure the required safety limits for the transmitted light beam.

Thus, a passive optical limiter fulfills the sensing, processing and the shutter or modulating function, all in one. This would be a high speed, compact and less expensive solution. The difficulty here is to find materials that have strong enough optical nonlinearities, that is, materials whose electric polarization **P** depends non-linearly on the incident electric field **E**, according to the following expression: $\mathbf{P} = \varepsilon_0 \chi^{(1)}\mathbf{E} + \varepsilon_0 \chi^{(2)}\mathbf{EE} + \varepsilon_0 \chi^{(3)}\mathbf{EEE} + \ldots$ where the usually linear susceptibility of the material χ is generalized to $\chi^{(i)}$, i.e. a tensor of order "i", i ≥ 2 (Boyd, 2003). Non-linear absorption (NLA) is one among many nonlinear mechanisms proposed to be used for passive optical limiting. An approximate effective coefficient of NLA may be expressed as: $\alpha_{eff} = \alpha + \beta I + \sigma_{ex} N_{ex}$

where: I = the incident irradiance;

α = the linear coefficient of absorption,

β = the two photon absorption coefficient

σ_{ex}= absorption cross section of the excited state

N_{ex} = population density of the excited state

Two examples of the physical phenomena that enable NLA are:

a) **two photon absorption** which is a third order non-linear absorption process, in which two photons are absorbed simultaneously after the intensity of the electric field reaches a certain threshold.

b) **two step absorption process**, during which atomic excitation takes place by linear absorption up to a certain energy level, which triggers a second step absorption at a much higher rate.

However, for electric fields of low intensity all materials have linear optical properties obeying the usual linear relationship $\mathbf{P} = \varepsilon_0 \chi \mathbf{E}$ and only for high enough intensities does the response of the material become non-linear. NLA can likewise be triggered only for high enough electric fields, such as the pulsed laser light. Therefore, since the intensity of a laser beam is maximum at the focal plane, potential non-linear materials and prototypes of optical limiters are tested at this section, i.e. the focal plane, as shown in the schematic of FIG. 1.3, to obtain the largest non linear effect possible.

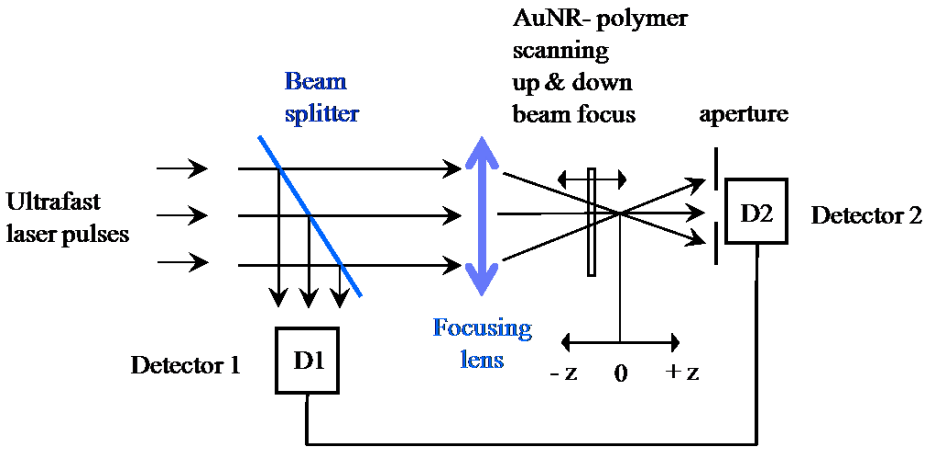

FIG. 1.3 Schematic of experimental set-up for testing the non-linear absorption (NLA) of a AuNRs-PVA composite film - adapted from (Li, 2010).

However, even in the focal plane of a laser beam, where the energy density is highest, the non-linearity of the known materials is just enough but not sufficient in the pupil plane, where the receiving system in need of protection is normally positioned. Thus, even under optimized optical conditions the difficulty in developing a passive optical limiter remains finding materials with strong enough NLA properties.

One possible solution for achieving a passive optical limiter is a gold nanorod-polymer composite film with strong enough NLA properties, which constitutes one of the research incentives of my first topic.

Some of the optical limiter applications include: protective goggles for people working with laser light in scientific laboratories, devices for laser power regulation or stabilization, or restoration of signal levels in optical data transmission or logic systems. (Hagan, 2004).

of signal levels in optical data transmission or logic systems

1.2.2. **Application example 2: Biosensor**

In human health care, an ideal preventive intervention that includes diagnosis and treatment or removal of cancer cells should be sensitive enough to be able to detect and destroy even a single mutated cell to prevent the genesis of cancer cells and their proliferation. The idea of such ultra-sensitive tests may seem farfetched but already today's advances in theranostics (biodiagnosis and therapeutics), have demonstrated the potential of nanoparticles in this regard (Huang, (2006); Alkilany (2012); Zhang (2013); Guo, (2013)].

The functioning principle of such applications is based on bioconjugated NPs i.e. NPs coated with specific chemicals for the recognition of target cells. These NPs also have high permeability (by endocytosis) and high retention capability into malignant cells and tissues. Once the NPs identify and bind to their target, pulsed laser light is delivered by fiber optics and endoscope at the resonant wavelength of the NPs in the "water window" or between 700 to 1200 nm, where the surrounding healthy tissue absorbs light minimally and thus the damage of the tissue is avoided. Spectra of light scattered back or absorbed present shifts that allow for the diagnosis of the cancerous cells.

As to the therapeutic function, after the NPs irradiation, their excited atoms relax by releasing the absorbed energy as heat. The resulting increased temperature may either trigger the release of drugs that had been loaded on or may initiate the thermal lysis of vital organelles that leads to their death.

The equally important interaction between NPs and the surrounding biological tissue is solved by a protein layer that tends to adsorb around the NPs. This "protein corona" that masks the NP affects positively their toxicity, cellular uptake and pharmacokinetics. The ideal residence time of the NPs within the biological system can

be adjusted by allowing for the absorption of nonspecific protein to the NPs, which enables their elimination from the system..

In the above example, the detecting NP would need to be resonantly excited to maximally absorb or scatter light at NIR wavelengths (within the "water" window) and be illuminated individually, if possible.

1.3. Research objectives

This thesis aims at developing models to characterize optical properties of plasmonic anisotropic nanostructures and verify them through spectroscopic methods. Two cases of anisotropic structures are considered, namely, a nanorod-polymer composite film and nanostars.

First subtopic: Development and optical characterization of a gold nanorod – polymer composite film in which the rods are uniaxially aligned to the highest possible degree. The special feature of the composite film is that it may induce NLA in the rods due to their alignment and high enough concentration and has potential applications for optical limiting. This topic was pursued in the following three stages:

- Improvement of the film matrix composition to allow for high stretch ratios
- Optical characterization, spectroscopic and numerical of the composite film
- Development of a novel non-destructive method to quantify the alignment of the embedded rods

Second subtopic: Optical characterization of a gold nanostar by using numerical simulations of a model geometrically parameterized. Finding out the most effective

control factors of tunability of its absorbance peak in the NIR region of the spectrum is of special interest.

1.4. Overview of the remaining chapters

The remaining chapters of the thesis will describe in detail the methods used in my research and the results obtained.

Chapter 2. **Theoretical background**

As a preliminary introduction to the interaction between light and metal nanoparticles, a few important definitions and physical phenomena specific to the problems dealt with in this work will be presented. After a short presentation of the electronic structure of metals, the dielectric function and ways to express it analytically will be defined such as to match experimental data, starting from the first theory on electron dynamics conceived by Drude up to taking into account the size and shape of the NPs. Based on the background presented so far, a well informed selection of the NPs material is possible so criteria for selecting gold will be presented. Polarization of light and dichroism, which were used heavily throughout this work, will be described. Lastly, the numerical simulations of absorbance carried out to parallel or complete the spectroscopic observations will be briefly described for situations where experiments were not possible.

Chapter 3. **Improved Alignment of Gold Nanorods Embedded in Polymer Films**

This chapter is based on the manuscript with the same name, submitted to the International Journal of Theoretical and Applied Nanotechnology, accepted for publication and currently in press, which also was presented at the International

Conference on Nanotechnology: Fundamentals and Applications, Toronto, August 12-14 2013.

After reviewing the methods for aligning nanorods used today, factors that govern the alignment process are presented and a change of composition of the matrix material is proposed to allow for a maximal increase of stretch ratio of the composite film. The preparation of the film is then discussed and the results obtained by measuring the absorbance spectra of film in polarized light are assessed. A dichroic ratio is also defined as a measure of rod alignment and its linear tendency with respect to the stretch ratio is presented.

Chapter 4. **Optical characterization of the stretched AuNR-PVA composite film**

This chapter is based on the article "Dichroic optical properties of uniaxially oriented gold nanorods in polymer films" published as an "Online First" article by "Plasmonics", 2013, 10.1007/s11468-013-9623-x.

In this chapter the importance in maintaining a low enough temperature during the preparation and stretching of the composite film is described and a threshold is determined in order not to trigger the atomic rearrangement of the rods which would lead to the alteration of their optical properties. Next, a statistically significant sample is estimated and used in assessing the degree of alignment of the rods and the dichroism of the film. The numerical simulations that were carried out are also presented, including the mesh convergence study and the size and shape dependent dielectric function of gold. Finally, the stretching device that was developed especially for this experiment will be described and its manufacturing drawing and the photograph of a film strip clamped and stretched in the device will be shown.

Chapter 5. **Non-Destructive Quantification of Nanorod Alignment**

This chapter is based on the manuscript entitled "Non-Destructive Quantification of Alignment of Nanorods Embedded in Uniaxially Stretched Polymer Films" submitted to the peer-reviewed Journal of Applied Physics on November 21, 2013, currently under review.

In this chapter a novel method for quantifying the alignment of the rods achieved by uniaxially stretching the composite film, is proposed without using electronic microscopy that requires destructive examination but by combining a probabilistic model, an assumed Gaussian distribution of the aspect ratio of the rods and numerical simulation of absorbance spectra of a discrete group of geometrically representative rods. Assuming electromagnetically non-interacting rods, the longitudinal absorbance peak of their ensemble is considered to consist of the superposition of their individual spectra that are obtained by numerical simulation using the size and shape adapted dielectric function of the metal and the finite difference time domain method. The precision of the solution depends on the number of discretization intervals, the accuracy of the numerical simulations and the precise knowledge of the polydispersity of the rods. For the sake of concreteness, nanorods were used to describe the quantification steps but the method is equally valid for any dichroic particles.

Chapter 6. **Optical properties of gold nanostar-PDMS composite**

This chapter is based on the article entitled "Fabrication of a Gold Nanostar - Embedded Porous Poly(dimethylsiloxane) Platform for Sensing Applications", published in "Sensors & Transducers", 149, 2, 20, (2013) and co-authored by me. My contribution

in this article was the simulation of the absorbance spectra of a AuNS embedded in PDMS by solving the electrodynamics equations of a parameterized 3D-model and using the FDTD method. The results of my parametric study showed that superimposing spectra of stars with branches of different lengths and tip aperture angles could generate overall spectra in good agreement with the spectra measured spectroscopically. They also demonstrated the enhanced tunability of NSs compared to NRs, means of tuning the excitation of AuNSs in the most effective manner as well as how to design NSs characterized by a desired spectral location and absorbance intensity of its fundamental excitation mode if NSs of certain well defined geometries could be controllably synthesized.

Chapter 7. **Conclusions and Contributions** in which the main findings and contributions made in this work are emphasized, as well future research topics are suggested.

2. Theoretical background

Chapter outline

2.1. Electronic structure of metals
2.2. The dielectric function
    2.2.1. The Drude-Lorentz classical model
    2.2.2. Comparison with experimental data
2.3. Surface plasmon resonance (SPR)
2.4. The size and shape adaption of dielectric function
2.5. Material selection
    2.5.1. Chemical neutrality
    2.5.2. Chemical binding despite general nonreactivity
    2.5.3. Excitation of SPR in the VIS-NIR region
    2.5.4. Ongoing research on cell toxicity of AuNRs
2.6. Polarization of light
    2.6.1. Polarizer
    2.6.2. Dichroism
2.7. Numerical simulations of optical properties
    2.7.1. Governing equations and computation scheme
    2.7.2. The computation grid and boundary conditions

2.1. Electronic structure of metals

Properties of matter in any type of interaction with its surrounding are defined by the behavior of matter in response to the agent of interaction and depend on its internal organization, such as arrangements and interactions at the atomic and subatomic level. As a particular case of properties, optical properties of metals are defined by the response of the metals to electromagnetic (EM) radiation in the visible range and depend on the electronic structure of the metals.

Metals in their bulk state are solids in which atoms are arranged in a three-dimensionally periodic network, also called a crystal lattice. The nuclei of the atoms, which are much heavier than the electrons are imagined almost immobile, positioned in the nodes of this lattice. Around the nuclei orbit the electrons organized in shells, subshells and orbitals, which can be rationalized by invoking the uncertainty principle. Farthest away from the nuclei, on the outermost atomic shell lie the valence electrons that are thus only weakly bound to the nuclei of their atoms. In these positions, they are also the main mediators in interaction with the outside of the metal block, other materials or the incident light and are therefore the main determinants of the metallic properties.

However, the periodic arrangement of the atoms in their crystal lattice also induces a periodic potential energy of the electrons, which makes that the electrons are organized into bands of energy, possibly separated by forbidden bands, or band gaps, depending on the respective energy level and on the material in question. In the same time, due to the high density of atoms and their electrons in solids, electrons occupy energy levels that are separated by only very small differences, compared to the thermal energy at room temperature. Thus, in metals, the band of valence electrons is either incompletely filled (such as in the case of gold and silver) or overlaps with other empty energy bands.

An electromagnetic (EM) radiation incident on a metallic NP subjects all the electrons inside the metal to EM forces. However, only electrons having the largest kinetic energy or velocity, at the Fermi level, also called the Fermi surface in the velocity space, may feel a net effect, since for all others, any increase in their velocity will be cancelled by another one in the opposite direction. Thus, the electrons of valence bands

that are partially filled and which have a high number density near the Fermi energy level can easily break away from their atoms and transit to excited states of higher energy and momentum by absorbing even small amounts of energy from low frequency photons. Since the attractive forces towards the nuclei of their atoms of origin are even more diminished at this level, the newly arrived electrons are almost completely free to drift and contribute to the electric and thermal conductivity which are specific properties that define a metal. For this reason they are also called "conduction" electrons, populating the "conduction" band.

However, electric and thermal conductivity cannot be achieved by isolated atoms, irrespective of the element they represent. In order to exhibit metallic properties, a cluster of atoms of an element that is considered "metal" in its bulk state, must have a large enough size such that the density of states in the vicinity of the Fermi level form bands of energies. Therefore, the name "metallic nanoparticle" already implies cluster sizes larger than the critical size at which the conduction band develops.

Assuming NPs of at least a few nanometer size, their interaction with light, i.e. EM radiation in the visible range (i.e. 390-770 nm wavelength), can be described by using classical electrodynamics, with no need of quantum mechanics. (Maier 2007, Bohren & Huffman, 1983). Only for particle sizes comparable to or smaller than de Broglie wavelength of the material $\lambda_{deB} \sim h/\sqrt{m_e k_B T}$, do boundary surfaces of the particle confine the conduction electrons and quantum mechanics needs to be applied to calculate the equations of motion and the quantized energies of the electrons.

In the classical interpretation, light is modeled as an EM wave instead of a beam of photons and matter is considered as composed of electric dipoles. This is because the

negative electrons and positive ions, which normally balance each other out are separated apart from each other by the external EM field. Metallic atoms thus become small electric dipoles, tending to orient themselves along the lines of external EM field, which constitutes the polarization of matter. The dynamics of electrons in a metal is then modeled as a collection of atomic scale simple harmonic oscillators (SHOs), as in the Drude-Lorentz model set into forced oscillation by the EM forces induced by the incident electric field. The equations of SHOs do not exactly reflect the physical phenomena but they lead to results identical to those obtained by quantum mechanics, except for their interpretation (Bohren & Huffman 1983). The classical results allow for a good qualitative understanding of the optical phenomena.

2.2 The dielectric function

In the classical interpretation of optical properties of metals, in which the electrons are described as SHOs driven by forces induced by an external EM field, as shown above, the following simplifying assumptions are made:

a) The ***local electric field*** $\mathbf{E}_{\mathbf{local}}$ actually seen by an electron in a metal consists of the incident external electric field $\mathbf{E}_{\mathbf{ext}}$ superimposed on the secondary field $\mathbf{E}_{\mathbf{sec}}$ scattered back by the neighboring atoms within the metal. Since the resulting microscopic field $\mathbf{e}(\mathbf{r})$ comprises unnecessary details of variation in an amount impossible to handle, the field is smoothened by averaging over the volume of a crystal cell, as shown below, to define the **macroscopic field E** which is used instead (Kittel, 2005)

$$\mathbf{E}(\mathbf{r}) = \frac{1}{V_C}\int \mathbf{e}(\mathbf{r})dV$$

As well, since the secondary radiation is much less than the external field, the local electric field is approximated as: $\mathbf{E}_{\mathbf{local}} \approx \mathbf{E}(\mathbf{r}) = \mathbf{E}_{\mathbf{ext}} + \mathbf{E}_{\mathbf{sec}} \approx \mathbf{E}_{\mathbf{ext}}$

b) The material is assumed to have the following properties:

- **Isotropy,** i.e. the polarization **P** is parallel with the electric field **E,** hence

  P = $\varepsilon_0\chi\mathbf{E}$**,** where χ is the dielectric susceptibility and ε_0 is the permittivity of vacuum

- **Linearity**, i.e. it obeys linear constitutive laws: **D** = $\varepsilon_0\varepsilon\mathbf{E}$ and **B** = $\mu_0\mu\mathbf{H}$, where "**D**" is the dielectric displacement; "**H**" and "**B**" are the magnetic field and magnetic induction, respectively; "ε" and "μ" are the relative permittivity and permeability of the material, respectively. All are assumed time-harmonic functions of angular frequency "ω".

- **Homogeneity**: despite the discrete distribution of its microscopic charges: positive ions and negative electrons, their number density is assumed large enough such that the metal can be idealized as a homogenous continuum of charges with instantaneous response to the electric field.

2.2.1 **The Drude-Lorentz classical model**

The conductance electrons are assumed to be a collection of isotropic, independent and identical second order SHOs driven by a time-harmonic excitation of frequency ω. By neglecting the scattered radiation from the neighboring atoms, this many-body problem becomes a system of differential equations of the following form (Maier, 2007):

$$m\ddot{\boldsymbol{x}} + b\dot{\boldsymbol{x}} + k_{\mathrm{SHO}}\boldsymbol{x} = -\mathrm{e}\mathbf{E}_{\mathbf{0}}\exp(-i\omega t) \tag{2.1}$$

where: **x** is the displacement vector of electrons from their equilibrium positions, "e" and "m" are the electric charge and effective mass of an electron, respectively; "b" is the damping coefficient due to electron collisions and k_{SHO} is the stiffness of a SHO. Dividing by mass, (2.1) becomes:

$$\ddot{\boldsymbol{x}} + \gamma\dot{\boldsymbol{x}} + \omega_0^2\boldsymbol{x} = -(\mathrm{e/m})\mathbf{E_0}\exp(-i\omega t) \tag{2.2}$$

where $\omega_0 = (k_{SHO}/m)^{1/2}$ is the natural frequency, $\gamma = b/m = 1/\tau$, is the collision frequency of the electrons and τ the relaxation time of the order $\tau \sim 10^{-14}$ s (Maier, 2007).

To simulate the free conduction electrons the spring constant of the oscillators or their natural frequency is set to zero: $\omega_0 = 0$ and the solution can be written as:

$$\boldsymbol{x} = \frac{(\mathrm{e/m})\mathbf{E}}{\omega^2 - \omega_0^2 + \mathrm{j}\gamma\omega} = \frac{(\mathrm{e/m})\mathbf{E}}{\omega^2 + \mathrm{j}\gamma\omega} \tag{2.3}$$

The electrostatic imbalance due to the displacement of the electrons from their neutral positions induces a dipole moment in each atom. Assuming a maximum EM-coupling between all electrons such that they oscillate collectively and coherently, i.e. in phase, the polarization vector P, or the average dipole moment per unit volume, is:

$$\boldsymbol{P} = -N\boldsymbol{e}\boldsymbol{x} = -\frac{Ne^2/m}{\omega^2 + \mathrm{j}\gamma\omega}\boldsymbol{E} \equiv \varepsilon_0\chi\boldsymbol{E} \tag{2.4}$$

where N is the number density of free electrons and the second identity constitutes the constitutive relationship: $\mathbf{P} = \varepsilon_0\chi\mathbf{E}$. The "plasma frequency" is defined as:

$$\omega_{\boldsymbol{P}}^2 = Ne^2/\mathrm{m}\varepsilon_0 \tag{2.5}$$

and is a constant of the metal. From (2.4) we identify the dielectric susceptibility as:

$$\chi = -\frac{\omega_P^2}{\omega^2 + j\gamma\omega} \tag{2.6}$$

and the dielectric function of the metal

$$\varepsilon(\omega) = 1 + \chi = 1 - \frac{\omega_P^2}{\omega^2 + j\gamma\omega} \equiv \varepsilon_1 + j\varepsilon_2 \tag{2.7}$$

with the following real and the imaginary part (Maier, 2007):

$$\varepsilon_1 \equiv \mathrm{Re}(\varepsilon) = 1 - \frac{\omega_P^2}{\omega^2 + \gamma^2} \tag{2.7a}$$

$$\varepsilon_2 \equiv \mathrm{Im}(\varepsilon) = \frac{\gamma\omega_P^2}{\omega\left(\omega^2 + \gamma^2\right)} \tag{2.7b}$$

2.2.2 Comparison with experimental data

Large discrepancies are noticed between the above analytical expressions and the experimental data for gold in the bulk state (Johnson & Christy, 1972) as seen in FIG. 2.1:

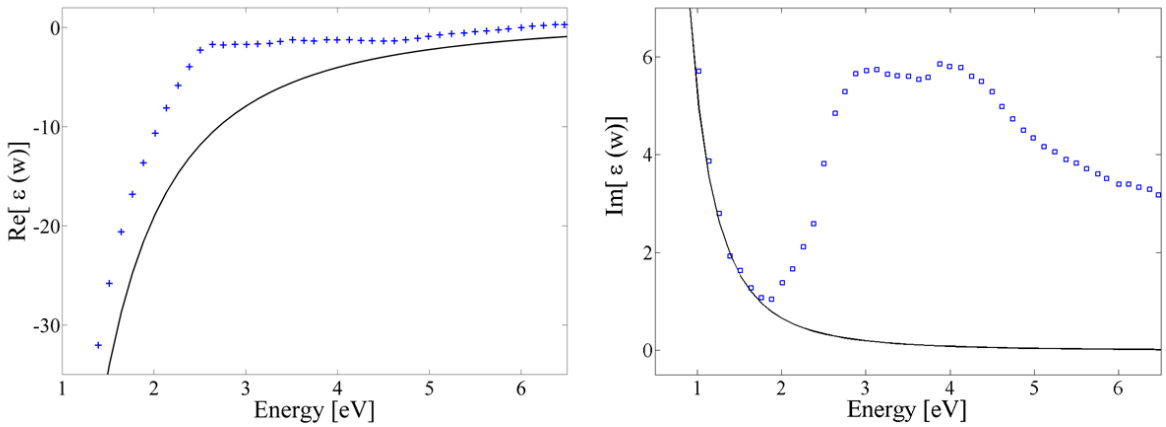

FIG. 2.1 Comparison between the dielectric function calculated using equations (2.7 a & b) of the Drude-Lorentz model (continuous lines) and experimental data [Johnson & Christy, 1972] (marked by "plus" and "square" signs) for bulk gold.

The difference is due to the influence of electrons from other bands than the conduction band. For gold, the band of electrons "d" is filled and it affects the Fermi level from where the electrons are promoted into the conduction band. In addition to the intraband transitions that occur at low energies, for energies higher than 1eV, interband

transitions between quantized states start to occur. To remedy the calculation model, the interband transitions are modeled as bound electrons using the full equation (2.1) of the SHO, which results in the addition of a number of terms leading to an expression of the dielectric function of the following form [Maier, 2007]:

$$\varepsilon(\omega) = 1 + \sum_{n} \frac{A_n}{\omega_n^2 - \omega^2 - j\gamma_n \omega} \tag{2.8}$$

The same expression is obtained by applying quantum mechanics, although some terms may have different meanings and interpretations [Bohren, 1983].

In the analyses that carried out in this work, the wavelength range of interest was between 400-900 nm, which corresponds to 1.4 – 3.0 eV in the energy terms. It is seen from FIG.2.1 that the Drude-Lorentz relations (2.7) do not fit well to the actual dielectric function of bulk gold for this region of frequencies. For this reason, the FDTD simulations were carried out by using the dielectric function based on the experimental data of (Johnson & Christy, 1972).

2.3 Surface plasmon resonance (SPR)

To find out the physical meaning of plasma frequency ω_p defined in (2.5) we let $\omega \rightarrow \omega_p$ in (2.7) for small damping limit: $\gamma \sim 0$, which leads to $\varepsilon(\omega_p) = 0$ and **K** || **E** from (2.8), meaning that the oscillation waves of the conduction electrons are longitudinal. The equations of motion of the electrons can be set up by imagining the following experiment. An initial uniform external electric field normal to an infinite conducting slab of finite thickness as in FIG.2.2 displaces the conduction electrons and creates a

surface charge distribution σ and an internal field E_{int}. The external field is turned off at t=0. The electrons return to their initial position to reestablish balance but they overshoot, which initiates an oscillatory motion [Greffet, 2012]

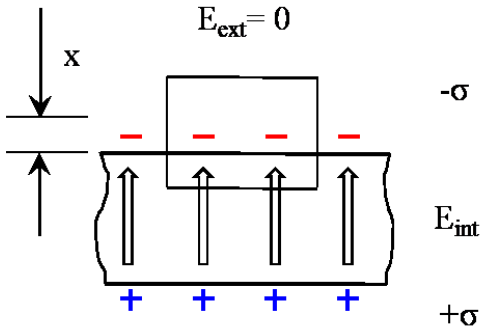

FIG. 2.2 Bulk plasmon in a metal slab

The surface charge excited by the initial electric field can be determined by using Gauss theorem for a Gaussian rectangular box, as shown in FIG. 2.1. Thus:

$$\sigma = Nex \tag{2.9}$$

The equation of the collective and coherent oscillation of the free electrons is (Maier, 2007):

$$m\ddot{x} \qquad\qquad \ddot{x} \qquad\qquad \frac{Ne^2}{m\varepsilon_0} \tag{2.10}$$

from which the plasma frequency defined in (2.5) is recognized as the natural frequency of oscillation of the conduction electrons.

In light-matter interaction, the energy transferred from the radiating field to matter is not continuous but discrete, each photon absorbed in matter causing a quantum excitation with a certain quantized energy and momentum. Thus, the quantized excitation of electric charge, as discussed above is called “plasmon” and a quantum of another type of excitation (charge, electron-hole pair or lattice) coupled with the EM field is called

polariton (Bohren & Huffman, 1983). Regarding the coupling between charge and the EM field, depending of its specific, the following definitions exist [Maier, 2007]:

- **plasmon or volume or bulk plasmon** is a quantized collective and coherent excitation of electric charge, as schematically suggested in FIG. 2.2;
- **surface plasmon polariton** (SPP) is an EM excitation propagating at the interface between a dielectric and a conductor, evanescently confined in the perpendicular direction, as schematically suggested in FIG. 2.3.(a);
- **localized surface plasmon** is a non-propagating excitation of the conduction electrons of metallic nanostructures coupled to the EM field, as schematically suggested in FIG. 2.3.(b).

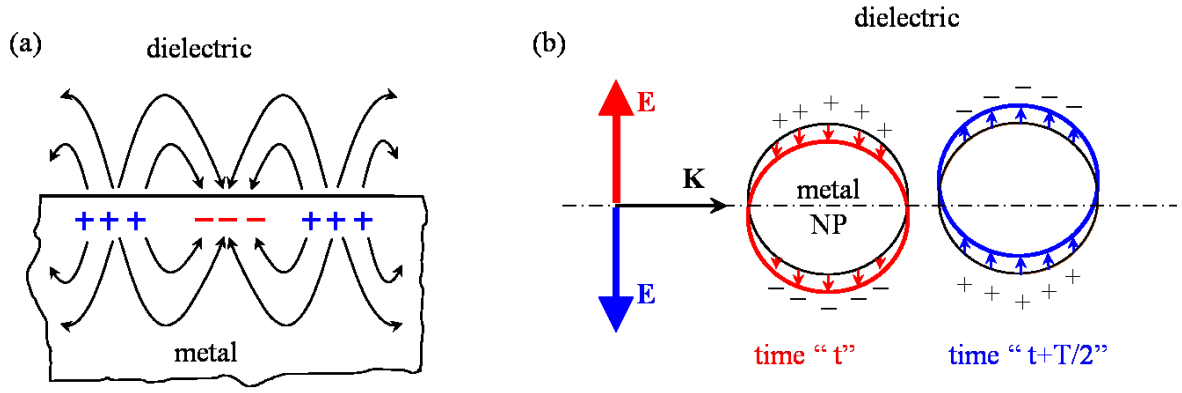

FIG. 2.3 (a) propagating surface plasmon polariton - adapted from [Willets & Van Duyne, 2007) (b) localized surface plasmon polariton - adapted from (Hutter & Fendler, 2004; Myroshnychenko et al., 2008)

2.4 The size and shape adaption of dielectric function

At the wavelengths of interest (400-900 nm) and at room temperature the mean free path (MFP) of the free conduction electrons of bulk gold is $12 \leq \text{MFP} \leq 42$ nm (Ashcroft, 1976; Zhukov, Chulkov & Echenique 2006), which is larger than the smallest dimension of the nanorods (diameter d=10 nm) that will be used in the AuNRs-polymer composite film. Therefore, the dielectric function of the rods is dependent on the size and shape of the particles (Genzel, Martin & Kreibig, 1975; Noguez, 2007). This dependence is treated classically by considering a reduced effective MFP denoted by "L_{eff}" of the free conduction electrons of the following form (Coronado & Schatz, 2003; Liu & Guyot-Sionnest, 2004):

$$L_{\text{eff}}(\eta, \mathrm{d}) = \frac{4\mathrm{V}}{\mathrm{S}} = \frac{2\eta}{1+2\eta}\mathrm{d} \tag{2.11}$$

This takes into account the energy loss at the particle surface S and within its volume V (where $\eta = L/d$ is the aspect ratio of the particle). A corresponding effective collision frequency of the free electrons due to the reduced MFP and scattering from the particle surface (Genzel, 1975), is introduced as:

$$\gamma_{eff} = \gamma(L_{\text{eff}}) = \gamma_0 + \frac{Av_F}{L_{eff}} \tag{2.12}$$

where $\gamma_0 = 1.075\ 10^{14}\ s^{-1}$ [Johnson and Christy, 1972] is the collision frequency of the free electrons in the bulk material, $v_F = 1.39\ 10^6$ m/s [Kittel, 2005] is the Fermi velocity of electrons and A is the electron-surface scattering parameter, a dimensionless constant. The contribution of the free electrons to the dielectric function is obtained by inserting the effective collision frequency γ_{eff} into the classical (Drude) dielectric function of (2.7):

$$\varepsilon_F(\omega) = \varepsilon_D(\omega, L_{eff}) = 1 - \frac{\omega_P^2}{\omega^2 + j\gamma_{eff}\omega} \tag{2.13}$$

However, the contribution of the bound electrons, considered not to be affected by the size and shape of the particle, can be expressed in terms of the free electrons unaffected by size and shape, which is just the Drude expression for the free electrons, as follows:

$$\varepsilon_B(\omega) = \varepsilon_{bulk}(\omega) - \varepsilon_D(\omega) \tag{2.14}$$

where $\varepsilon_D(\omega) = 1 - \frac{\omega_P^2}{\omega^2 + j\gamma_0\omega}$ is the Drude dielectric function of (2.7).

Assuming the contributions of the free and bound electrons are additive, leads to the following dielectric function (Noguez, 2007):

$$\begin{aligned}\varepsilon(\omega, L_{eff}) &= \varepsilon_F(\omega) + \varepsilon_B(\omega) \\ &= \varepsilon_D(\omega, L_{eff}) + \varepsilon_{bulk}(\omega) - \varepsilon_D(\omega) \\ &= \varepsilon_{bulk}(\omega) + \frac{\omega_P^2}{\omega^2 + j\gamma_0\omega} - \frac{\omega_P^2}{\omega^2 + j\left(\gamma_0 + \mathrm{A}\frac{Av_F}{L_{eff}}\right)\omega}\end{aligned} \tag{2.15}$$

Finally, the non-dimensional electron surface scattering parameter A = 0.33 was adopted from experimental determination of the plasmon bandwidth of a single gold nanorod. (Sönnichsen, Franzl, Wilk, von Plessen, & Feldmann, 2002; Berciaud, Cognet, Tamarat, & Lounis, 2005; Novo et al., 2006).

2.5 **Material selection**

Gold, with the chemical symbol of "Au" from the Latin "aurum", has been selected for both nanorods and nanostars for the following reasons:

2.5.1 Chemical neutrality

Under normal conditions, gold does not enter into chemical reactions with other elements. For example, gold can be oxidized only in conditions of high pressure of several 1000 atm (Pei et. al., 2009) and temperature due to its chemical stability. Therefore, Au is one of the few metals that can be prepared at the nanometer scale under ambient atmospheric conditions, without reacting with the oxygen. Other metals oxidize, which results in an oxide layer at the surface of the features. The problem with the oxide layer is that it grows up to a few micrometers thickness until the oxide layer itself becomes self passivating, i.e. the superficial layer is thick enough to arrest the oxidation process). At this thickness, an oxide would obviously cover and spoil any geometric details at nm-scale of the nanoparticle.

For NRs of diameter d=10 nm and length L=38 nm as those used in the composite film, if gold would oxidize in aqueous solution at room temperature, the reaction would propagate throughout their volume and transform them into rods of gold oxide (Au_2O). Since Au_2O has the real dielectric function $\varepsilon_1 = 10$ and the imaginary part $\varepsilon_2 = 0$ at the LSPR wavelength λ=850 nm or E=1.45 eV (Pei et. al., 2009), the corresponding refractive index and extinction coefficient would be $n_{Au2O} = 3.2$ and $k_{Au2O} = 0$, respectively, which have very different values from the actual coefficients of gold: n_{Au}= 0.28 and $k_{Au} = 5.2$. Thus, the optical properties of the rods would change dramatically.

Another advantage of its chemical inertness is its limited interaction with biological tissues, insuring its safe use in biological applications. However, research on its possible toxicity in human health care is still ongoing.

2.5.2 **Chemical binding despite general nonreactivity**

During the synthesis of AuNRs in aqueous solution [Perez-Juste, 2005] the surfactant cetyl trimethylammonium bromide (CTAB) or $(C_{16}H_{33})N(CH_3)_3Br$ was also used together with silver nitrate ($AgNO_3$) to promote the axial growth. It is known that CTAB molecules bind to the {1,1,0} and {1,0,0} side faces of the nanorods, while the binding to the {1,1,1} faces or the rod ends is much weaker, which allows for higher aspect ratio rods. The notation {h,k,l} denotes a family of equivalent crystallographic planes, where h,k and l are Miller indices. As a result, the AuNRs remain coated by a bilayer of CTAB from their synthesis. In order to prevent the aggregation of the AuNRs during their later mixing in the polymer solution, AuNRs were kept coated by surfactant.

Thus, despite being chemically non-reactive, gold has the useful ability to bind to CTAB possibly via a gold bromide surfactant complex [Sabatini, 2007, p.147].

Binding to other chemical compounds is also necessary for its biofunctionalization in biosensing [Anker, 2008] or imaging applications and most importantly in disease treatment, where they are used as drug carriers or destroyers of cancer cells. Chemical linkers such as thiol groups are used for protein conjugation to the surface of AuNPs.

2.5.3 **Excitation of SPR in the VIS-NIR region**

Most metals in the bulk phase can be resonantly excited by light in the ultraviolet (UV) region of wavelengths, except for gold and silver that are excitable in the visible (VIS) to NIR domain. It is thus possible to observe the excitation of AuNPs with the unaided eye, which has been recognized almost 2000 years ago and used as colorants in

stained glass windows, pottery or as dye. This is an important advantage since it allows for applications such as biosensing using inexpensive measurement equipment.

2.5.4 Ongoing research on cell toxicity of AuNRs

Any extraneous matter introduced in a biological tissue has effects that depend on the size and concentration of the respective particles and so do even AuNRs. However, as long as direct contact with biological cells is prevented by coating the gold NPs, such as in the case of AuNRs used as drug carriers, there is no toxicity risk. In their other therapeutic or imaging roles, however, the potential toxicity of AuNRs in direct contact with biological cells is carefully studied, depending on their size and concentration. The potential therapeutic or other biomedical applications of AuNRs is huge and there is an intense research that is carried out ***in vitro*** and ***in vivo*** to find out the limitations that must be imposed on using AuNPs in order to be able to make use of it, [Alkilany, (2012)].

2.6 Polarization of light

The description of light has so far been concerned only with its direction of propagation, given by the propagation vector **k** where $k=2\pi/\lambda$. We have thus assumed that the plane defined by the electric field and its propagation vector, also called the plane of vibration, remains fixed during the propagation, while the electric and magnetic field vary in magnitude. In such a case light is called linearly or plane polarized in the respective plane of vibration. Two examples of plane polarized light are shown in FIG.2.4.

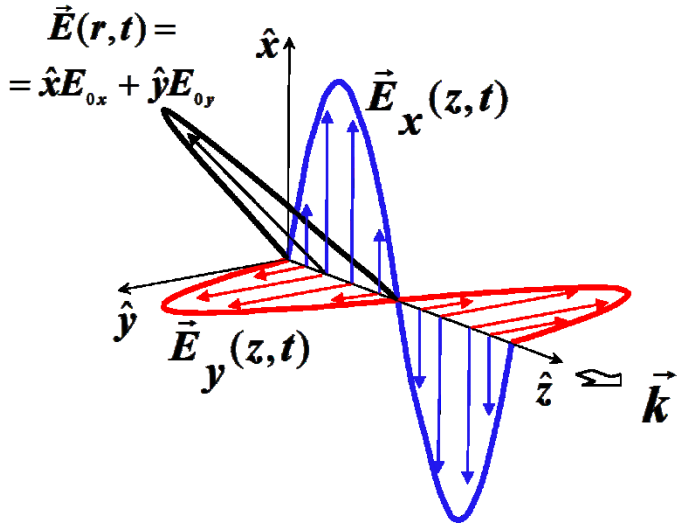

FIG.2.4 Plane polarized lightwaves in the [xOz] and [yOz] planes and in an arbitrary plane in the first quadrant of the reference system – adapted from (Hecht, 2002)

In the most general case, the electric field of a lightwave can be described by the expression: $\boldsymbol{E}(z,t) = \boldsymbol{E}_0 \cos(\boldsymbol{k} \bullet \boldsymbol{r} - \omega t)$ where $\boldsymbol{r}$ is the position vector. If we choose a reference system {x,y,z} with the Oz axis along the direction of propagation of a lightwave, and select the xOz plane as the plane of vibration of a plane polarized lightwave, then the electric field can be expressed as: $\vec{E}_x(z,t) = \hat{x}E_{0x} \cos(kz - \omega t)$.

However, the plane of vibration may rotate around the propagation direction making an angle θ(t) possibly varying in time. This angle is called polarization angle and in general, the exact orientation of the electric field is called the state of polarization.

If the state of polarization of a lightwave is not specified, it is assumed that the wave is unpolarized or randomly polarized, by which it is meant that the respective wave is formed by rapidly varying polarization states. Natural light is unpolarized, for example, by which it may be understood that it originates from many superimposed atomic size emitters, randomly polarized.

2.6.1 Polarizer

A polarizer is an optical device that accepts at its input a lightwave of an arbitrary state of polarization and produces at its output a wave of the desired polarization. If the output state of polarization is linear, then the polarizer is also called linear polarizer.

In the measurements of light absorption by the composite film developed in this research, many recordings of absorbance spectra were carried out in linearly polarized light by using a linear polarizer attached to the light source of the spectrophotometer. The purpose was to find out how the absorption of the nanostructure depended on its position relative to the orientation of the incident electric field.

2.6.2 Dichroism

Each optical device absorbs light in a specific way. That means that light energy is transformed in a specific way, depending on the internal structure or chemical composition of the device and also depending on the orientation of the incoming light.

In the case of the composite film, the electrons of the embedded metallic nanorods are set into oscillation by the incident electric field. Their accelerated charges constitute microscopic currents of highest intensity along the long axes of the rods, which endows the device with a preferential ability to absorb light. The time varying micro currents generate magnetic fields whose directions are related to the axes of the rods of origin. In their turn, the microscopic magnetic fields are time varying as well and they generate other secondary electric fields, which interact with the primary incident electric field. The constructive interaction defines the so called “transmission axis” (TA), which is a direction along which the electric field passes unabated while along the direction

perpendicular to TA, the electric field is cancelled, due to the destructive interaction with the secondary electric field.

Dichroism is the ability of an optical device to absorb selectively one of the two orthogonally plane polarized components of the incident light.

The absorbance of the AuNR-polymer composite film whose development is presented in Chapter 3 will be tested with polarized light and will be demonstrated that it has good dichroic properties.

2.7 **Numerical simulations of optical properties**

Throughout this work, numerical simulations of the optical properties of nanostructures were carried out in addition to spectroscopic measurements, aiming at the following goals:

a) To start by gaining confidence in the way a well established and one of the most complete and successful numerical method in the field of nanostructures was used.
b) To verify the validity of the data on the material used, such as the dielectric function of gold, by comparison with known results.
c) To fill in the experimental gaps, that is, to expand my research into domains where experiments were not possible to carry out. Such was the case of calculating optical properties of an array of perfectly aligned, non-interacting and geometrically identical nanorods.
d) Based on the confidence gained, to demonstrate potential optical properties of new structures that are not yet possible to synthesize, to help orient the development and

design of future new nanostructures. As an example, the potential nanostar structure defined parametrically by a number of branches of variable thickness, length and angle aperture was examined, to show that a nanostar as a whole had an excitation frequency that is tunable in the region of interest by conveniently adjusting four geometric parameters.

2.7.1 Governing equations and the computation scheme

Optical properties of metallic NPs can be treated by applying classical electrodynamics, interpreting light as an EM wave and matter as a collection of electric dipoles, as it was shown in section 2.1. Thus the laws governing the interaction of light and matter are expressed by Maxwell equations in their macroscopic form (2.16), completed by the constitutive equations (2.17) for linear, isotropic, non-magnetic and homogenous materials. The microscopic heterogeneity is insured to be negligible compared to the wavelength of the incident radiation, by choosing a sufficiently small lattice spacing [Maier, 2007; Bohren, 1983]:

Maxwell equations

$$\nabla \bullet \boldsymbol{D} = \rho_{ext} \qquad (2.16a)$$

$$\nabla \bullet \boldsymbol{B} = 0 \qquad (2.16b)$$

$$\nabla \times \boldsymbol{E} = -\mu_0 \mu \, \partial \boldsymbol{H} / \partial \boldsymbol{t} \qquad (2.16c)$$

$$\nabla \times \boldsymbol{H} = \boldsymbol{J}_{ext} - \partial \boldsymbol{D} / \partial \boldsymbol{t} \qquad (2.16d)$$

Constitutive laws

$$\boldsymbol{D} = \varepsilon_0 \varepsilon \, \boldsymbol{E} \qquad (2.17a)$$

$$\boldsymbol{B} = \mu_0 \mu \, \boldsymbol{H} \qquad (2.17b)$$

$$\boldsymbol{J} = \sigma \boldsymbol{E} \qquad (2.17c)$$

The commercial software RSOFT, based on a Finite Difference Time Domain (FDTD) numerical method was used to solve the partial differential equations (PDE) (2.16) & (2.17). The FDTD method is second order accurate and its accuracy depends on the coarseness of the grid employed for the discretization of the equations. The method consists of the following steps:

- discretizing the time and spatial domain of the problem;
- approximating differentials by central finite differences in time and space;
- solving the resulting algebraic system subject to boundary conditions.

The numerical calculation scheme is based on estimating the first order derivative of a function "f(x)" by the central difference formula, which is second order accurate with the following approximation expression:

$$\left.\frac{\partial f}{\partial x}\right|_{(x=x_o)} \approx \frac{f(x_0 + \Delta x) - f(x_0 - \Delta x)}{2\Delta x} \tag{2.18}$$

Yee's mesh and notations are used (Yee, 1966), in which a grid point in the solution region is denoted by: (i, j, k) ≡ (iΔx, jΔy, kΔz) and a function of space and time is denoted by: $F^n(\mathbf{r},t) = F(i\delta, j\delta, k\delta, n\Delta t)$, where $\delta = \Delta x = \Delta y = \Delta z$ and Δt are the spatial and time increments, with i, j, k and n integers. The resulting equation system contains the following second order accurate finite difference approximation of the derivatives:

$$\left.\frac{\partial^n f}{\partial x}\right|_{(i,j,k)} \approx \frac{f^n(i+1/2, j, k) - f^n(i-1/2, j, k)}{\delta} \tag{2.19a}$$

$$\left.\frac{\partial^n f}{\partial t}\right|_{(i,j,k)} \approx \frac{f^{n+1/2}(i, j, k) - f^{n-1/2}(i, j, k)}{\Delta t} \tag{2.19b}$$

Thus, for example, the discretized form of (2.16c) has the expression shown below, in (2.20):

$$\frac{\partial H_x}{\partial t} = -\frac{1}{\mu_0 \mu}\left[\frac{\partial E_z}{\partial y} - \frac{\partial E_y}{\partial z}\right] \tag{2.20a}$$

$$\frac{H_x^{n+1/2}(i,j,k) - H_x^{n-1/2}(i,j,k)}{\Delta t} = \\ = \frac{1}{\mu_0 \mu}\left[\frac{E_y^n(i,j,k) - E_y^n(i,j-1,k-1)}{\Delta z} - \frac{E_z^n(i,j,k) - E_z^n(i,j-1,k)}{\Delta y}\right] \tag{2.20b}$$

2.7.2 The computation grid and boundary conditions

For all numerical models in this work, a 3D non-uniform mesh was used, because it is more economic in computation time and memory. The minimum space step was chosen small enough to be able resolve the smallest geometrical feature of the nanostructure and also be much less than the incident wavelength. A mesh example is shown in FIG. 2.3, but this is actually much coarser than the mesh actually used, for better visual clarity. In addition, for the stability of the solution, the time step was related to the spatial step by the Courant criterion, which requires the following condition be satisfied (Taflove & Hagness, 2005):

$$c\Delta t \le 1/\left[1/\Delta x^2 + 1/\Delta y^2 + 1/\Delta z^2\right]^{1/2} \tag{2.21}$$

However, after the preliminary choice of the mesh size, the spatial step was adjusted by carrying out convergence analyses, to insure that the response of the nanostructure to the incident lightwave did not depend on the size of the mesh. This was done by varying the mesh size a number of times, checking the results at each step. The procedure was repeated until the sought response ceased to change. Such convergence analysis was carried out for each of the analyses presented in this work.

Absorbing boundary conditions (ABC) were also used to prevent the incident or transmitted lightwaves reflect back from the boundaries of the computational domain and thus simulate an unbound space around the numerical model. Their further interference with the incident waves would have altered the results, which had to be avoided. In this regard the perfectly matched layer (PML) technique (Berenger, 1994) was used, which is implemented in the RSoft software.

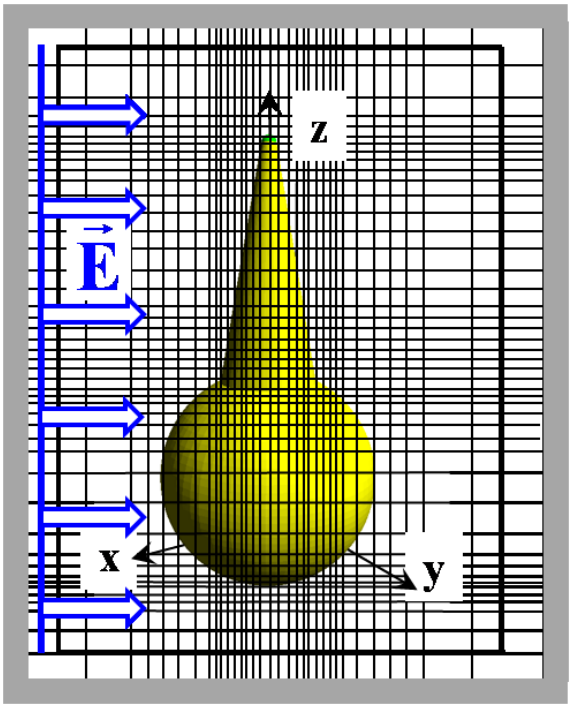

FIG. 2.4 Schematic showing the principle of non-uniform grid used to compute the properties of a one-branch nanostar 3D-model. The grid actually used was much finer, but it has been coarsened for clarity. The nanostructure is excited by a wavelight that is emitted from the launch pad, drawn in blue color. The monitor is shown as the black line rectangle and the PML as the outer gray strip.

3. **Aligned gold nanorods: Improving the matrix of the composite film**

Based on "Improved Alignment of Gold Nanorods Embedded in Polymer Films",

Int. J. of Theoretical & Applied Nanotechnology, in press, December 2013

Chapter outline

3.1. Introduction
3.2. Review of aligning methods
3.3. Improving the plastic deformability
3.4. Experimental – film preparation
3.5. Assessing the stretching of the composite film

3.1. Introduction

Since the excitation of the LSPR of NRs is highly tunable in the "tissue diagnostic" or "water" region (700-1200 nm of the optical spectrum) by adjusting as many as five geometric factors: aspect ratio, end cap geometry, volume of the rod, convexity of waist and convexity of the ends, there are many applications that make use of the excitation of the LSPR of aligned NRs. For instance, besides the first application example in optical limiting that was presented in the introduction chapter, other applications include selective patterning of aligned metallic rods embedded in thin polymer films by selective laser melting of the rods [Wilson, 2002].

However, in an application based on NRs, if the component rods are randomly oriented or misaligned, their optical properties are averaged out and the nanostructures function less effectively. Therefore, these applications can work at their highest efficiency only if all component AuNRs can be maximally excited, simultaneously. This may take place only if the applications use either a single rod or an ensemble of fully aligned ones.

Out of the two alternatives, using a single rod is not preferred, because although the optical detection, characterization and utilization of a single NR was demonstrated some time ago [Klar, 1998], applications based on single NRs would still require more expensive equipment and would be difficult to be miniaturized and implemented in practical devices. The second alternative, applications based on aligned rods is more practical and several methods of rod aligning have been investigated, each one having its own degree of difficulty.

3.2 Review of aligning methods

Among a few notable methods, using electric field to induce alignment moments in AuNRs suspended in liquid solutions was shown to require very high field strengths in order to make sure that the disturbing Brownian motion is overcome. Electric field strengths as high as 15 kV were found insufficient to fully align the suspended NRs [Padilha et al., 2009], which confirmed the experimentally unattainable high electric field strengths reported previously [van der Zande, 1999].

In a different approach, electric fields generated between micrometer spaced electrodes did achieve high enough field strengths to induce alignment moments that overcame the Brownian motion in a colloidal AuNR solution. The colloidal system was then allowed to dry slowly, in the presence of this strong field. However, besides generating alignment moments, the electric field also induced dielectrophoretic forces in the rods, which caused their accumulation around the electrodes and hence a nonuniform spatial distribution. Moreover, despite sufficiently high alignment moments, the resulted

degree of alignment was “considerably smaller” than the ones reported for AuNRs suspended in solution [Ahmed, 2009].

The directional growth of AuNRs, starting from seeds implanted on different substrates [Mieszawska, 2006] was studied as well, but this method could not provide a transparent substrate, which is necessary to types of experiment such as the one in this paper.

Rod alignment by uniaxial film stretching is another method. It consists in embedding the AuNRs in a film of thermoplastic polymer that is subsequently heated up to its softening temperature. By simultaneously subjecting the film to tensile stress, a sufficiently large elongation can be obtained. In this process, the nanorods in contact with the polymer chains get entrained and reach a final orientational position parallel with the direction of stretching. It results that the degree of alignment of the rods is directly proportional to the stretch ratios of the film and therefore, the highest possible stretch ratios were attempted in this work. This was achieved by slightly modifying the composition of the composite matrix in order to improve its plastic deformability. A stretching device was also designed in order to reduce the risk of film fracture. Finally, the alignment of the AuNRs was assessed qualitatively by scanning electron microscopy (SEM) and quantified by calculating an average orientation angle and an orientational order parameter.

3.3. Improving the plastic deformability

The matrix of this type of composite film is usually chosen to consist of polyvinyl alcohol (PVA) because this polymer can be drawn into thin and transparent films. This is due its thermoplastic properties, which makes that it softens when heated up to its glass

transition temperature Tg (85°C) and flows under tensile stress. If PVA is cooled back to room temperature, it regains its hardness in a reversible cycle. This is possible because its molecules consist of many thousands of carbon atoms bound together by single and strong covalent bonds, which form long linear chains with rotational, bending and twisting flexibility in three dimensions (Callister et al., 2010). Therefore, a well-stirred PVA aqueous solution with well dispersed AuNRs may reach a highly entangled state of its chains. If the mixture is allowed to dry, it will solidify in this state, forming a film. By heating up the film while simultaneously applying a slowly increasing stretching force, the secondary bonding forces between chains will be broken, allowing them to disentangle. Eventually, the polymer chains will be straightened out with their axes oriented along the stretching direction, and the rods aligned parallel to the stretch direction, as well.

Thus, matrix polymers of longer molecular chains allow for higher film stretch ratios because the relative displacement of the chains is possible along longer distances. However, the higher molecular weights of such polymers also have higher glass transition temperature. But heating up to this temperature is limited by the risk of thermal reshaping of the rods with altered optical properties as a consequence. (Perez-Juste et al., 2005; Liu Y. et al., 2009). In order to depress the softening temperature, a small amount of glycerol as plasticizer was mixed in the polymer solution. The selection of glycerol was based on a study (Finch C., 1973) that found that it was one the plasticizers most compatible with PVA.

Subsequently, the transparency of the glycerol-PVA films was tested in the visible-NIR range and it was found to have been well maintained. This verification was

necessary in order to insure that the optical excitation of the embedded AuNRs would not be obstructed.

Finally, films with glycerol of 2% and 4% mass percent concentration of PVA were tested and all could be stretched up to a ratio of seven. However, because one undesired side effect of the plasticizer is that the solidified film is less rigid, the optimal concentration of glycerol was chosen such as to insure that the resulting film could maintain a flat enough surface over a long period of time, after stretching.

Previous reports have indicated that a stretch ratio of four to six would be sufficient for a perfect alignment (van der Zande et al., 1999). In order to insure the best possible alignment of AuNRs embedded in the composite film, we aimed in this work for a stretch ratio of seven.

3.4. Experimental – film preparation

Completely hydrolyzed PVA 146,000-186,000 MW, glycerol G9012 (≥ 99.50%) and gold nanorods 716812 (diam. × L 10 nm × 38 nm +/- 10%) were all purchased from Sigma-Aldrich and used as received. A volume of 11 ml of AuNR solution of concentration 35μg/ml was used for forming of a composite film.

A mass of 2.04 g PVA granules was gradually mixed in 20 ml distilled and deionized water and slowly heated up to about 95°C under stirring, until a clear and transparent 10% PVA solution was obtained. After the solution cooled down to about 35°C, 32μl glycerol (2% of the PVA mass), was dropped into the PVA solution under stirring for an additional 30 minutes. The solution was subsequently degassed. Finally, 3.0 g of the above PVA-glycerol water solution was poured into a 50 ml beaker and 11 ml of the 35 μg/ml AuNRs colloidal solution was added, well stirred and sonicated for

about 30 minutes. The AuNR-PVA solution was subsequently cast into a 60 x 60 mm2 flat mold and allowed to solidify for 48 hrs at room temperature. The solidified film had an average thickness of 50 μm and was afterwards kept in an oven at 40°C temperature for 24 hrs to make sure it was completely dry. After having peeled it off, the film was cut into 20 by 30 mm rectangular strips. The strips were then clamped into the stretching device and gradually stretched under heating at about 65°C.

Absorbance spectra were obtained using a Perkin Lambda 650 spectrophotometer, in the visible - NIR region. Micrographs were taken with the JEOL JSM840 scanning electron microscope.

3.5. Assessing the alignment of the AuNRs

A measure of the resulting alignment of the rods is how well the LSPR mode can be excited in as many rods possible; ideally, in all the rods simultaneously, while the TSPR cannot be excited in any of them. Therefore, as a first check, we have the intensity of absorbance spectra of the film in light polarized parallel and perpendicular to the alignment direction s-s', as seen in FIG. 3.1 (a). A plane polarized lightwave with the electric field parallel ($E_{\|}$) with the stretch direction s'-s incident on the composite film, is strongly absorbed at the longitudinal wavelength and a minimal radiation energy is allowed to pass through the film. Consequently, the absorbance spectrum has a strong intensity peak that is proportional to the percent of aligned rods out of the total number, at the wavelength of excitation of the LSPR, which is about 850 nm. On the other side, for the incident electric field oriented perpendicular ($E_{\perp}$) to s'- s, the energy of the lightwave is transmitted unabated through the film because the rods are excited transversally, which requires a small amount of energy to be absorbed from the incident

field. Therefore, the composite film has optical properties similar to a dichroic polarizer with the transmission axis perpendicular to the stretch direction.

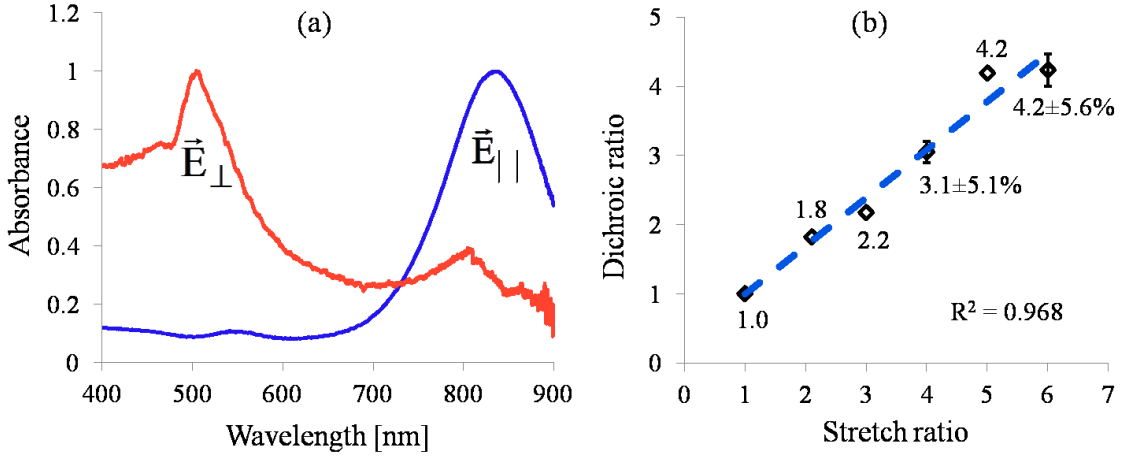

FIG. 3.1 (a) Normalized absorbance spectra of uniaxially stretched AuNR-PVA film illuminated by plane polarized light with the electric field parallel (E||) and perpendicular $(E_{\perp})$ to the s' – s direction. (b) Linear trend of the dichroic ratio dependence on the stretch ratio.

The above statement holds for the ideal case of perfectly aligned AuNRs embedded in a composite film. In reality however, a small absorbance peak can still be noticed located at wavelength of the transverse SPR, in panel (a), for light polarized parallel with the stretch direction. Similarly, a small absorbance peak is seen to persist at the longitudinal SPR wavelength, for light polarized perpendicular to the stretch direction. This demonstrates the existence of a large enough number of AuNRs that could not be aligned during the stretching process. These peaks would not exist in a perfectly aligned ensemble of rods.

Another way of quantifying the alignment of the rods is the dichroic ratio, defined as the ratio of the absorbance intensities for plane polarized light with the electric field parallel and perpendicular to s'- s. As seen above, the value of the dichroic ratio is also

proportional to the ratio of the number fraction of the rods parallel or perpendicular to the alignment direction. The dependence of the dichroic ratio on the stretch ratio is shown in panel (b) of FIG. 3.1. The trend line fitted to the experimental data suggests that the dichroic ratio may depend linearly on the stretch ratio.

4. Optical Characterization of the AuNR-PVA Composite Film

based on "Dichroic Optical Properties Of Uniaxially Oriented Gold Nanorods Embedded In Polymer Films" published online by ***Plasmonics,*** DOI 10.1007/s11468-013-9623-x *Oct. 6, 2013,*

Chapter outline

4.1. Introduction

4.2. Temperature threshold

4.3. Characterization

- 4.3.1. Statistically significant sample and average orientation angle
- 4.3.2. Optical characterization: dichroism
- 4.3.3. Optical characterization: deviations from dichroism

4.4. Numerical simulations:

- 4.4.1. Mesh convergence
- 4.4.2. Size & shape adapted dielectric function

4.5. Device for stretching polymer films

4.1. Introduction

In the previous chapter, the importance of the chemical composition of the film matrix was highlighted for attaining high stretch ratios of the composite film and the need to maintain a satisfactory quality of the film surface after drying. Both the stretch ratio and the surface quality of the film indirectly determine the optical properties of the film, which are essential for the optimal functioning of the application. However, since optical properties of the AuNRs depend both on their arrangement relative to each other and on the intrinsic properties of each individual AuNR, preserving them in unaltered condition during the casting process is equally important. More specific, aspects such as the heating temperature reached during the film stretching process may cause reshaping of the rods

and alteration of their optical properties. For this reason, this chapter will analyze the maximum allowable heating temperature and then the resulting alignment of the rods will be quantified statistically. The dichroism of the film, which is an optical property that strongly depends on the alignment of the rods, will be finally look at.

4.2. **Temperature threshold**

Heating the composite film up to the polymer glass transition temperature (i.e. the temperature where the polymer film in solid state softens and starts flowing) prior to and during the drawing process, may lead to structural instability of the embedded rods with consequent reshaping and altered optical properties, as proposed based on molecular dynamics simulations [Wang, 2005] and later demonstrated experimentally [Liu, 2009]. The results obtained suggested that atomic reorganization may be caused by unstable surface facets, which have high free energy and tend to reorient into more stable ones followed by the reorganization of the bulk to fit the new surface structure. In addition, ligands such as ions bonded to the rod surface as well as the surrounding PVA-matrix, play an equally important role in surface protection. It was hypothesized that reshaping may be prevented as long as ligands remain bonded to the crystal surface, but the decreased viscosity of a heated up surrounding medium may allow for diffusion of the ligands away from the crystal surface [Liu, 2009, Murphy, 2005].

To find out if ligand ions of surfactant (CTAB) attached to AuNRs in the PVA environment of the film matrix would allow for the thermal reshaping of the AuNRs, annealing experiments with unstretched films were carried out followed by spectroscopic measurements. It was found that a AuNR-PVA composite film annealed at a temperature

of 150°C for 15 minutes had a blue shift of 3 nm of the LSPR peak, which was a sign of incipient reshaping of the rods. The corresponding spectrum is shown in FIG.4.1.

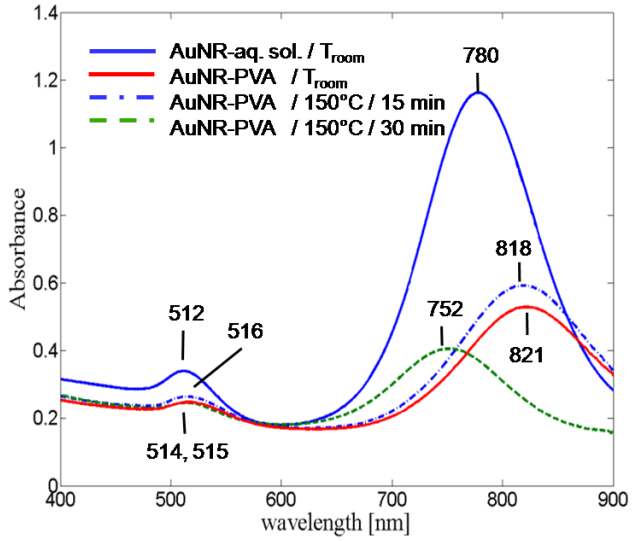

FIG. 4.1 Absorbance spectra of AuNRs in aqueous solution and embedded in unstretched PVA film under different annealing conditions

In this figure, it is also seen that annealing the film at 150°C for 30 minutes caused a blue shift of 70 nm, which implied a more severe reshaping and alteration of optical properties, as expected. This suggested that annealing at 150°C for 15 minutes was the thermal threshold between stability and atomic rearrangement of the rods.

Although this threshold had not been crossed, an examination of the micrograph of FIG. 4.2 (a) revealed the presence of spherical NPs as well. They could have been generated as byproducts of AuNR synthesis, in which case they could have been crystallized as spheres of any diameter. Or, they could have been generated by the accidental removal of the protective layer of CTAB that was coating the rods, which eventually allowed for the rearrangement of the rods into spheres.

Because the volume of a sphere resulting from a rod-to-sphere transformation, would be equal to the initial volume of the rod, the diameter of the sphere would be: $d_{sph} = 2\sqrt[3]{3d^2L/4} = 28.4nm$. But this is approximately the size of the sphere shown in the inset (i) of FIG. 4.2. This close match of dimensions supports the hypothesis of rod reshaping into spheres, although the temperature threshold had not been crossed.

4.3. Characterization

4.3.1. Statistically significant sample and average orientation angle

In order to assess the alignment or calculate any other statistic of the population of rods, the size of a statistically significant sample (SSS) will be first estimated.

Casting composite films depends on a large number of microscopic sources of variability, such as: a) polymer dissolution, which consists of disentanglement of polymer chains and solvent diffusion; b) local temperature and viscosity of the solution; c) dimensions and shape of each individual AuNR; d) thickness of surfactant coating and e) uniformity of the rod dispersion. Since none of these factors are controllable at the macroscopic scale of the gauging instruments, the following assumptions are made: (i) the orientation of the rods, before and after stretching is random; (ii) a stretched AuNR-PVA composite film contains a single layer of rods and forms a zero-thickness sheet that is defined by its middle plane; (iii) the geometric distortions of the SEM images caused by the microscope and the equipment setup are negligible.

Consequently, all AuNRs visible in a micrograph such as the one shown in Fig. 2 (a), whose apparent lengths are approximately equal to the nominal one of 38 nm are

considered to be lying in the middle plane of the film and their apparent orientation angles are accepted as having true values.

Moreover, each orientation angle φ, defined in the inset (ii) of Fig. 2 (b), is considered to be the realization of an independent and continuous random variable (RV) Φ. Assuming that every RV has the same probability distribution, each set $\{\Phi k\}$, $1 \leq k \leq n$, of RVs, defines a random sample (RS) of size "n", where n is the total number of relevant rods, collected from one or several micrographs.

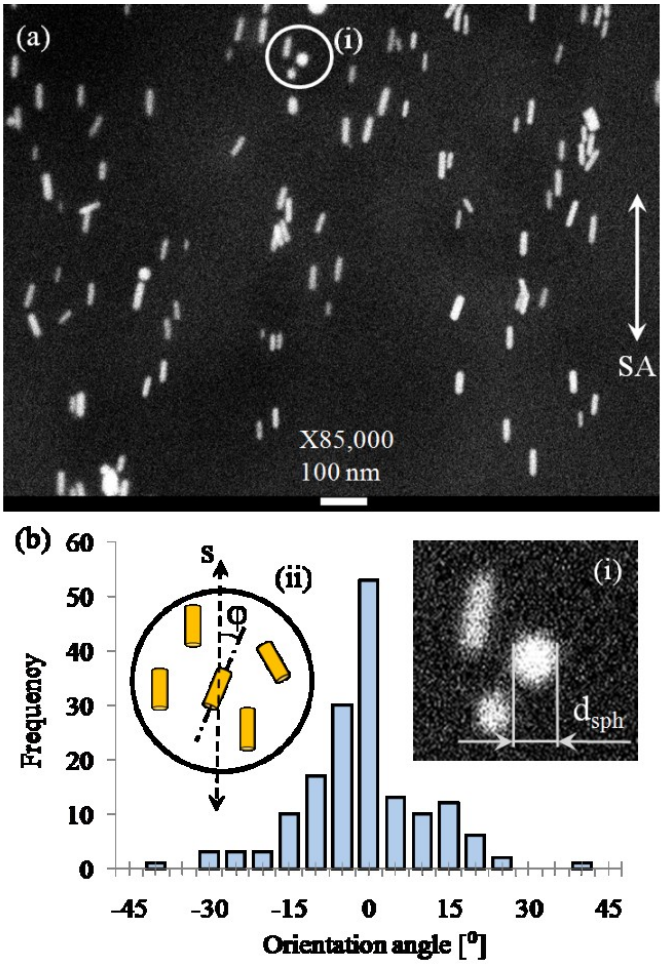

FIG. 4.2 (a) SEM micrograph of a AuNR-PVA film stretched along the stretch axis (SA), depicted by the double-headed arrow. (b) Histogram of orientation angles Insets: (i) Spherical NP likely to have been formed by thermal reshaping of a AuNR or as a synthesis byproduct (ii) Definition of the orientational angle φ

In addition, since about 10^{12} rods have been used for forming a composite film, it is meaningful to consider that the mean of the samples follows a Gaussian distribution, according to the central limit theorem. However, since the SEM micrographs contain much fewer rods, the Gaussian distribution assumption is extended to all RVs $\{\Phi_k\}$ for every sample.

As well, since neither the mean μ nor the variance σ^2 of the population is known, the t-distribution, instead of the Gaussian one is further assumed. Thus, the standardized variable: $T = (\bar{\Phi} - \mu)/(S/\sqrt{n})$ has a t-distribution with "n-1" degrees of freedom, where S^2 is the variance of the sample. Furthermore, an interval that contains the true mean orientation angle of the rod population with a required confidence "1-α" satisfies the condition: such that the precision of the confidence interval (CI) was $2t_{\alpha/2,\upsilon-1}$ The error "e" made in using to estimate μ is finally required to be equal to half the precision of the CI, and thus, the estimated size of the statistically significant sample is [Devore, 2012]:

$$n = \left(t_{\alpha/2,\nu} S/e\right)^2 \qquad (4.1)$$

Data for the calculation of 164 orientation angles φ was collected from two micrographs, out of which one is presented in FIG.4.2 (a). The mean of the selected sample had a value of $\bar{\Phi} = 3.5°$ and the standard deviation was S = 11.05°.

Requiring that the sample mean represents the true mean of the population of rods with a 96% confidence, a confidence factor of α = 0.04 results. As well, for ν = n-1 = 163 degrees of freedom, the percentage points of the t-distribution is $t_{\alpha/2,\nu} = 2.106$. Thus, using formula (4.1) for an admissible error of e = 2°, the size of a statistically significant sample was calculated to be $n_{sample} = 136$. It was therefore concluded that the above

sample of 164 rods was large enough such that the sample mean of $\overline{\Phi} = 3.5°$ was a good enough estimator of the true mean of the orientation angles. The estimated standard error made by using this sample is [Devore, 2012]:

$$\hat{\sigma}_{\bar{\Phi}} = \frac{S}{\sqrt{n}} = \frac{11.05^{\circ}}{\sqrt{164}} = 0.86^{\circ} \qquad (4.2)$$

Another way to quantify the alignment of the rods is the two-dimensional orientational order parameter [Ahmed, 2009; Hu, 2006], defined as $S = 2 < \cos^2 \varphi > -1$. Based on the statistically significant sample of rods determined above, the value of this parameter was found to be S = 0.92, which is 8% off the value corresponding to the perfect alignment (S = 1).

4.3.2. Optical characterization: dichroism

Unstretched AuNRs-PVA composite films have isotropic optical properties, since both the longitudinal and transverse SPR modes can be excited irrespective of the polarization state of the incident light, as the spectrum at the top of FIG. 4.3 indicates. This is due to the random orientation of the rods, which averages out their individual anisotropies. The schematic of the spectrophotometer-polarizer setup of FIG.4.3, inset (i), shows that unpolarized light from the spectrophotometer is passed through a linear polarizer of transmission axis fixed at a given angle θ. (The polarization angle θ between the electric field $\vec{E}$ and the stretch axis (SA) of the film is defined in the inset (i) of FIG.4.4).

Stretched films, on the other side, are optically anisotropic since the LSPR and TSPR modes can only be excited by light polarized parallel and perpendicular to the

stretch axis of the film, respectively. This is shown in the spectra at the middle and bottom of FIG.4.3.

Actually, since not all the rods can be fully aligned, both resonant modes can be excited to some extent by the same polarization direction. For example, the spectrum produced by light polarized parallel to the alignment direction $\theta = 0°$ presents a well developed LSPR peak in Fig. 3, but also a non-negligible transverse one.

The best optical performance is provided by an ideally fully aligned AuNR-PVA composite film, assumed to contain identical and non-interacting rods. Spectra of such a film can be appreciated by analyzing the FDTD-simulated spectra of a single AuNR, whose 3D model is shown coated by a layer of surfactant in the inset (i) of Fig.4.

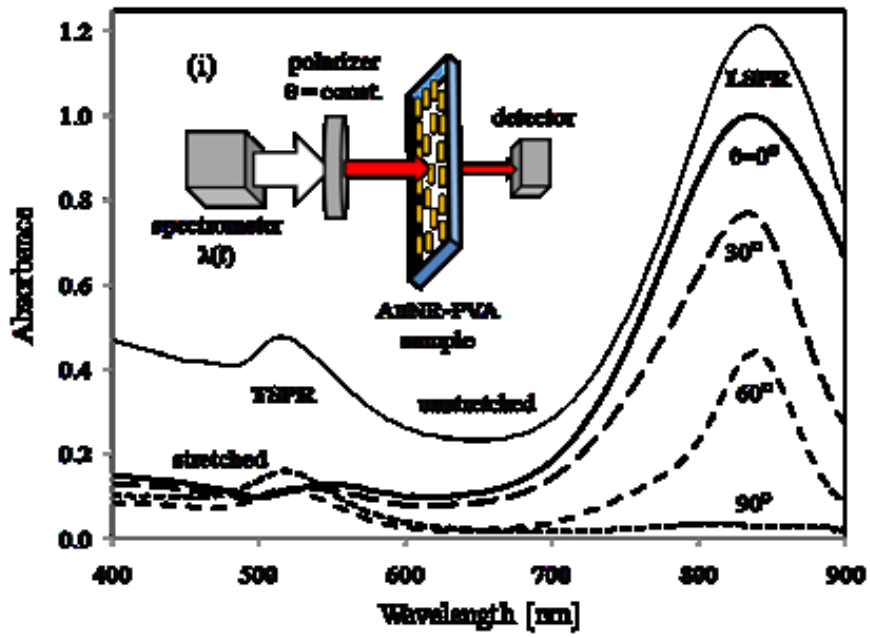

FIG.4.3 Absorbance spectra. Uppermost: spectrum of unstreched film, shifted vertically for better visibility; middle and bottom: spectra of stretched film for different polarization angles θ (defined in FIG.4.4). **Inset (i):** schematic of the experimental set-up.

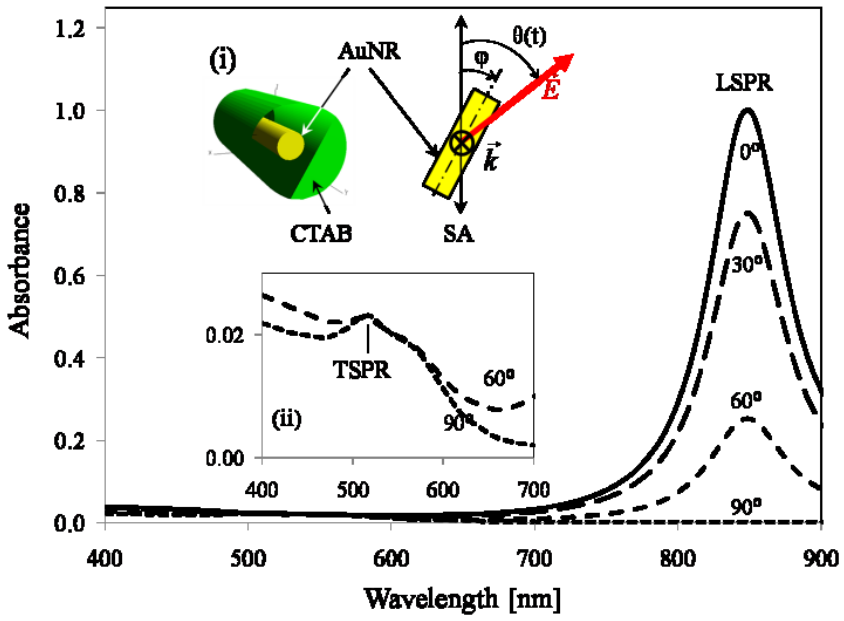

FIG.4.4 FDTD-simulated absorbance spectra of a single AuNR. **Inset (i)** FDTD 3D-model, coated with surfactant. (ii) scaled-up TSPR absorbance peak.

The agreement between the simulated and measured T- and LSPR peak wavelengths is very good. However, it is seen that the linewidth of the experimentally observed LSPR band is much broader than the linewidth of the simulated LSPR band. This discrepancy can be attributed to the size distribution of the rods. Namely, a size variability of the rods of ±10% around the nominal diameter "d" and length "L", allows for the aspect ratio η = L/d to range from a minimum η_{min}=3.11 to a maximum of η_{max}=4.64. Since the LSPR peak position is known to depend linearly on the aspect ratio within the electrostatics limit, it will have its own range of values, which will broaden the experimental LSPR band with respect to the simulated one. More exactly, the relationship between the aspect ratio of a NR and the peak position of its LSPR was derived theoretically [Link, 1999, Yan, 2003, Link, 2005] and also proved experimentally [Wilson, 2002; Brioude, 2005] to be:

$$\lambda_{LSPR} = (a\eta + b)\varepsilon_m + c \qquad (4.3)$$

where ε_m is the dielectric constant of the surrounding medium and a, b and c are constant coefficients, determined experimentally as listed in the table below:

Table 4.1 Coefficients defining the dependence relationship (4.3) of the peak wavelength of a AuNR on its aspect ratio

Author [year(s)]	a	b	c
S. Link & al. [1999, 2005]	53.71	-42.29	495.14
B. Yan & al. [2003]	52.95	-41.68	466.38

Therefore, rods of aspect ratios that differ by a maximum of $\Delta\eta_{max} = 4.64 - 3.11 = 1.53$ have the peak positions of their LSPR separated by a maximum of $\Delta\lambda_{max} = a_{avg}\varepsilon_m\Delta\eta_{max} = 166.4\,\text{nm}$ where a_{avg} is the average of the a-values from Table 1 and the dielectric constant of the medium is $\varepsilon_m = n_{CTAB}^2 = 2.04$. Taking into account that a spectrum is a superposition of elementary spectra of all atoms simultaneously excited by the light beam, the elementary spectra farthest apart tend to broaden the ensemble spectrum, provided that their number fraction is large enough. Measuring the full width at half maximum (FWHM) of the LSPR band, we found that the composite film had a FWHM of 144 nm which is only 13% smaller than the largest separation between elementary spectra found above. Therefore, the size distribution of the rods can explain the broadening of the experimental plasmon band.

It is also seen that, incident light polarized parallel with the stretch axis SA of the rods ($\theta = 0°$) is significantly more strongly absorbed than light polarized perpendicularly. First when the incident electric field is normal to the long axis of the rod ($\theta = 90°$), does

the transverse mode prevail, but it is still weak in absolute terms, while the longitudinal mode is not excited, as seen in the inset (ii) of FIG.4.4.

It results that plane polarized light is selectively absorbed with a 180°- periodicity of the polarization angle, which justifies the name “dichroic”.

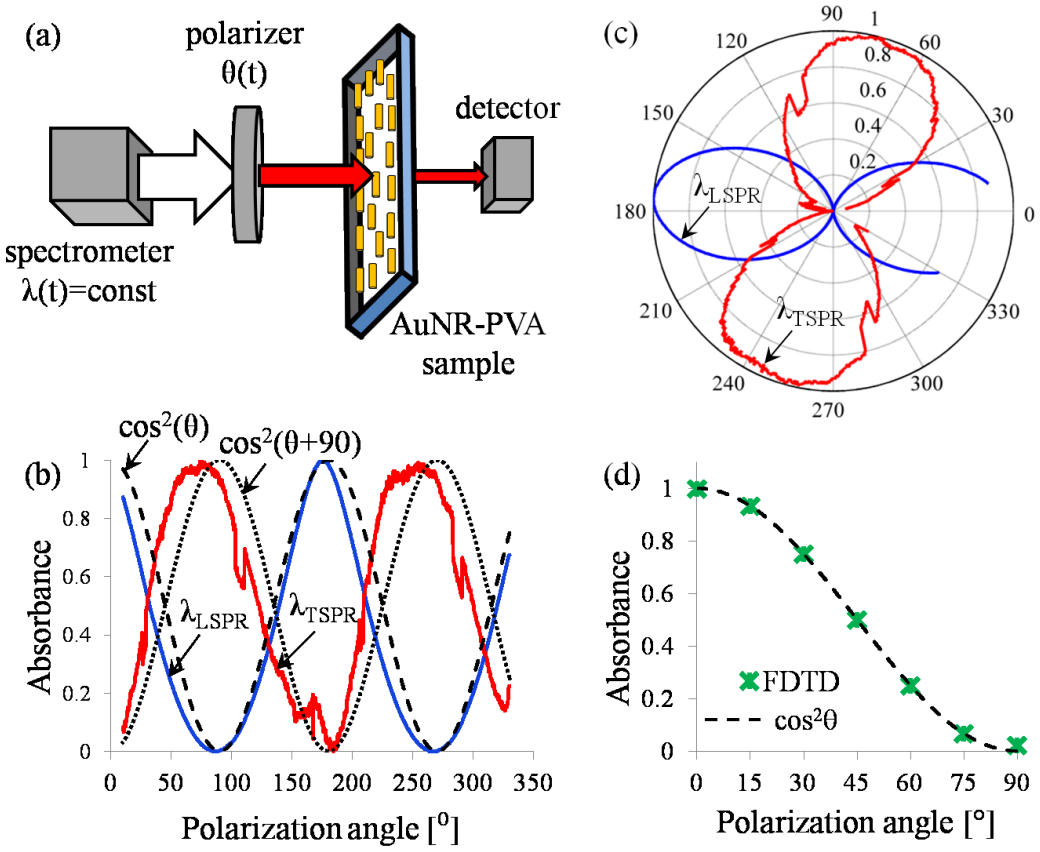

FIG.4.5 (a) Experimental set-up. (b) Measured absorbance spectra at L- and TSPR wavelengths matched with the theoretical cosine-squared law, in cartesian coordinates and in (c) polar coordinates (d) Matching of simulated absorbance spectrum at LSPR peak wavelength with the theoretical cosine-squared law.

This is illustrated in FIG.4.5, as follows: panel (a) shows that absorbance spectra were measured by scanning the polarization angle θ while keeping the wavelength constant. Panel (b): the two scannings performed at the T- and LSPR wavelength have 180°-periodic resulting absorbance spectra, dephased by 90°.

The 180°- periodicity of the stretched film spectra can be rationalized more rigorously as follows:

We first define a reference rectangular coordinate system {x, y, z} such that the x- and y-axes are parallel to the transmission axis (TA) and to the stretch axis (SA) of the AuNRs-PVA composite film, respectively. We also consider an incident electromagnetic radiation with the electric field component of magnitude E_0 propagating along the z-axis and polarized in a plane that makes an arbitrary angle θ with respect to the x-axis, as shown in FIG.4. 6.

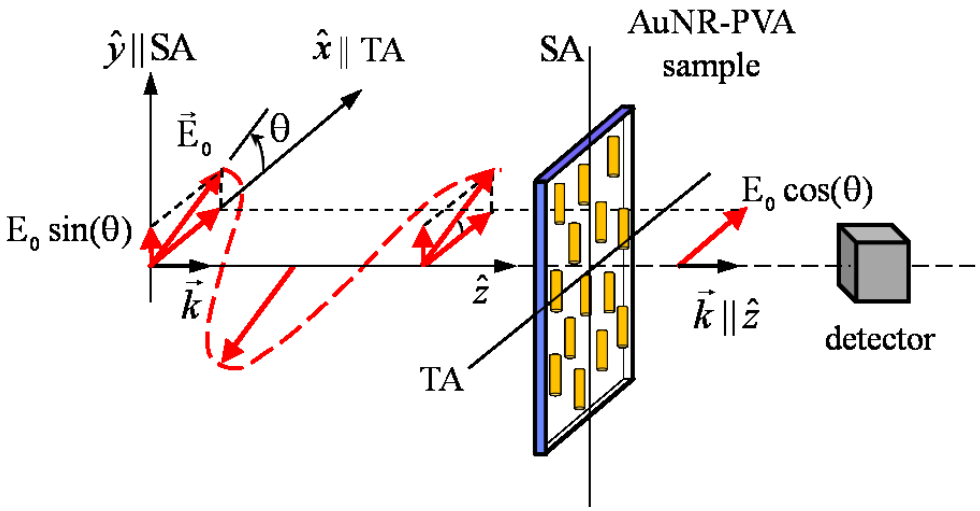

FIG.4.6 Schematic of a plane polarized light wave incident on the composite film at an angle θ with respect to the transmission axis (TA) of the film. TA is perpendicular to the stretch axis SA.

Assuming the rods embedded in the polymer film are perfectly aligned, they will fully absorb the y-component of the electric field and only the component parallel to TA or $E_0 \cos(\theta)$ will be transmitted, eventually reaching the detector of the spectrophotometer. Since we recorded our absorbance spectra in the visible range of radiation, the frequency of the incident field is of the order of 10^{15} Hz or very high and the detector will record

only the average energy per unit area and time, or the intensity (a.k.a irradiance) of the incident field [Pollack, 2002]:

$$I = \frac{c\varepsilon_0}{2} E^2 \propto \cos^2(\theta) \qquad (4.4)$$

which proves the cosine-squared law.

Therefore, the optical properties of a stretched AuNR-PVA composite film approach the properties of an ideal dichroic polarizer.

4.3.3. Optical characterization: Deviations from dichroism

The spectrophotometer that we used to record the absorption spectra had not been designed to measure absorption by individual atoms. More exactly, its light beam of macroscopic cross section could only be used to measure a superposition of atomic transitions taking place in a huge number of NPs, whose atoms are all simultaneously excited by the light spot. Therefore, an absorbance spectrum represents an average of those atomic transitions. A portion of these transitions clearly originated from rods, spheres and coupled particles, but their contribution to the overall spectrum is only proportional to their number fraction, due to averaging. Thus, the contribution of each shape to the ensemble spectrum can be estimated based on the SSS, as follows:

The SSS estimated above consisted of 165 observations which were collected from two SEM micrographs. The one shown in FIG.4.2 (a) contains 94 NPs, among which we can observe three possible spheres. In the second micrograph (not shown here) we could only observe one out of 75 NPs. Thus, our SSS contained four possible spheres out of a total of 169 NPs, i.e. a percentage of only 2.4%. As to the coupled AuNRs, we

observed a total of 13 cases out of 169 NPs, which is still not a large number (7.6% of the total).

Because the two samples make up a sample larger than the SSS, we can generalize this result to the entire population of NPs. We conclude therefore that the spherical AuNPs together with the coupled AuNRs contribute a small percentage to the overall ensemble, which may explain the deviations of their optical properties from the cosine-squared law.

As seen in FIG.4.5 (b), the polarization scan recorded at constant TSPR peak wavelength presents much larger fluctuations than the one recorded at constant LSPR peak wavelength. A first cause of this difference is the transformation of the two spectra by translation and scaling according to: $A'(\theta) = \left(A(\theta) - A_{min}\right) / \left(A_{max} - A_{min}\right)$ where A and A' stand for the original and the transformed absorbance, respectively. This was carried out such that both spectra share a common range of [0, 1] and in order to highlight their periodicity. However, the min-to-max variation in the LSPR case is larger by a factor of 0.436/0.016 or 27 than in the TSPR case. Therefore, the absorbance fluctuations measured at TSPR wavelength were normalized by a much smaller number, which has significantly magnified their amplitudes.

However, even the original absorbance fluctuations recorded at TSPR wavelength are larger than the ones recorded at LSPR wavelength and one possible explanation may be ascribed to deviations of the smaller transverse cross section of the AuNRs from its nominal shape, caused by the possible atom rearrangements mentioned above. More exactly, shape changes along the smallest cross sections lead to larger wavelength shifts of plasmon bands, as established recently [Sandu, 2012].

4.4. Numerical simulations

The best optical performance of the composite film can be obtained from an ideal ensemble of AuNRs that are identical in chemical purity and dimensions and which are perfectly aligned and uniformly dispersed at sufficiently large distance from each other such as not to interact electromagnetically. In order to use this ideal system as a reference of performance for the composite film, the absorbance spectrum of an ideal ensemble of rods was emulated by modeling a single AuNR and simulating its absorbance spectrum, as described below.

4.4.1. Mesh convergence

Any numerical model of a physical phenomenon involves the discretization of the computational domain with a maximum size of the discretization grid, which depends on the specific details of the phenomenon and the smallest dimensions of the geometrical model. The grid however needs to be refined in several iterations until the results obtained no longer depend of the size of the grid.

Therefore, in simulating the absorbance spectrum of a single AuNR, an orthogonal coordinate system {x, y, z} and a rectangular grid of size that depended on the region of interest, were first attached to the computational domain as follows. For the far-field region with respect to the AuNR, a grid of constant size of 5 nm was used, which was small enough compared to the minimum wavelength of 400 nm of the incident EM radiation. For the near-field region, close to the metal-dielectric interface, the

convergence of the simulations was studied starting from a size of 1nm for the mesh of the metal edge, decreasing down to 0.3 nm, equal in x, y and z directions. The results obtained are presented in the diagram of FIG. 4.7, where the size of the edge grid was used as the coordinate on the horizontal axis.

As convergence criteria the change of the LSPR peak wavelength and peak intensity relative to their average over all iterations were monitored. Variations between ±1% were obtained for an initial grid size of 1 nm for the relative change of the peak wavelength, shown as the dashed blue line in FIG. 4.7, which decreased down to values between ±0.4% for a grid size of 0.4 nm, which was considered accurate enough.

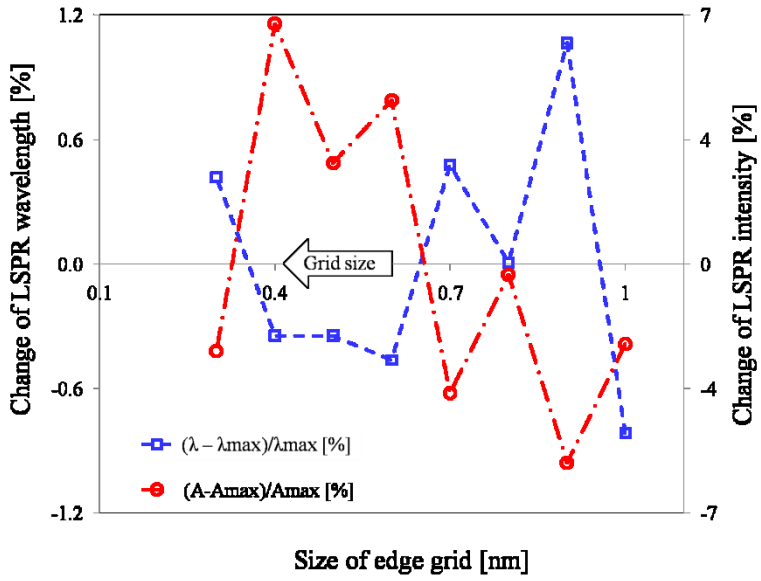

FIG.4.7 Mesh convergence**:** change of LSPR wavelength and intensity relative to the maximum of all iterations plotted with respect to the size of the edge grid.

4.4.2. Size & shape adapted dielectric function

Since the mean free path (MFP) of the free conduction electrons of bulk gold is within the range $10 \leq MFP \leq 42$ nm [Ashcroft, 1976; Zhukov, 2006] for the wavelengths of interest (400-900 nm) and at room temperature and therefore larger than the smallest dimension of the rods (diameter d=10 nm), the dielectric function of gold is dependent on the size and shape of the particles [Genzel, 1975; Noguez, 2007]. This dependence is treated classically by considering a reduced effective MFP (Leff) of the free conduction electrons, as follows [Coronado, 2003; Liu, 2004]:

$$Leff(\eta, d) = \frac{2\eta}{1+2\eta} d \qquad (4.5)$$

where η = L/d is the aspect ratio of a rod. The damping constant affected by the reduced MFP and scattering from the particle surface [Genzel, 1975], is written as:

$$\gamma_{eff} = \gamma(L_{eff}) = \gamma_0 + Av_F / L_{eff} \qquad (4.6)$$

where γ_0 = 1.075 1014 s^{-1} [Johnson & Christy, 1972] is the damping constant of the bulk material, v_F = 1.39 106 m/s [Kittel, 2005] is the Fermi velocity of electrons and A=0.33 is the electron-surface scattering parameter, a dimensionless constant [Sönnichsen, 2002; Berciaud, 2005; Novo, 2006]. The following dielectric function is obtained [Noguez, 2007]:

$$\varepsilon(\omega, L_{eff}) = \varepsilon_{bulk}(\omega) + \frac{\omega_P^2}{\omega^2 + i\gamma_0\omega} - \frac{\omega_P^2}{\omega^2 + i\gamma_{eff}\omega} \qquad (4.7)$$

in which is the plasma frequency of the electron gas [Maier, 2007]. The deviation of the refractive index and extinction coefficient from the bulk values due to size and shape effects, is shown in FIG.4.7, panel (a) and (b), respectively.

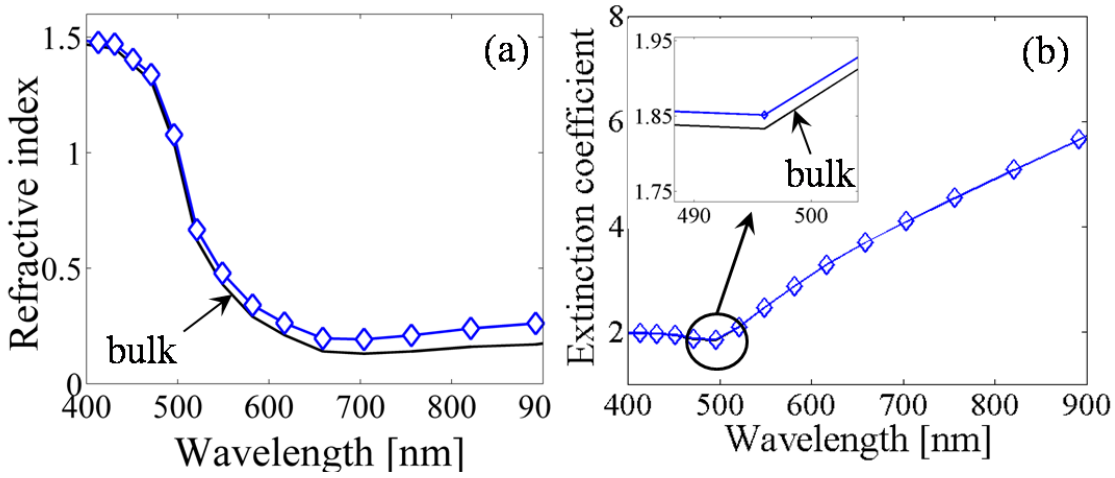

FIG.4.8 Effect of size and shape of the NPs on the refractive and extinction coefficients of gold: bulk (black line, no marker), size-adapted (blue line, diamond marker). (a) refractive index (b) extinction coefficient.

Both PVA and CTAB were modeled as non-dispersive media, with the following refractive indices: n_{PVA}=1.51 for PVA [Kumar, 2004] and n_{CTAB}=1.43 for the CTAB coating of the AuNRs [Yu, 2007].

4.5. Device for stretching polymer films

A device for uniaxially stretching polymer films was designed as shown in Fig.8.

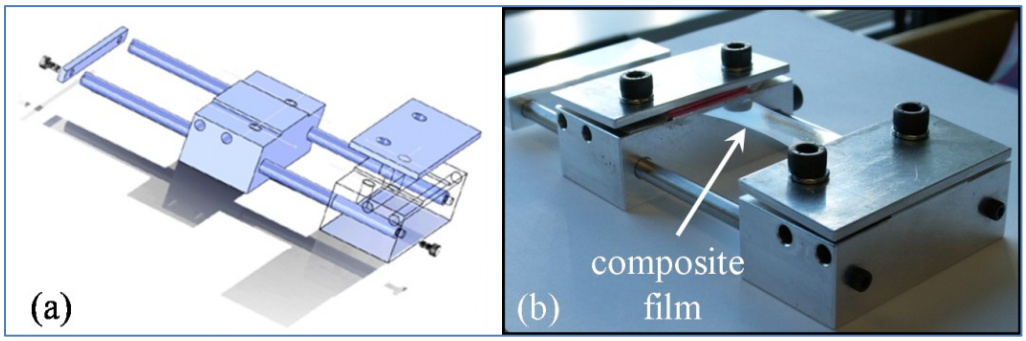

FIG.4.9 (a) Exploded drawing of the device for stretching polymer films (b) Photograph of a stretched AuNR-PVA composite film still clamped in the device and allowed to dry at room temperature for 24 hours.

The device was manufactured of aluminum, paying attention not to generate stress concentration factors, such as sharp notches or scratches, in order to reduce the fracture risks of the composite film. The device was designed to be operated manually, which should enable a better control of the stretching process. This could be achieved by increasing or just maintaining the tensile stress in the film, to allow for the disentanglement of the polymer chains, till the desired stretch ratio is reached.

5. Non-Destructive Quantification of Nanorod Alignment

Based on "Non-Destructive Quantification of Alignment of Nanorods Embedded In Uniaxially Stretched Polymer Films" submitted to: Journal of Applied Physics, November 22, 2013, currently under review

Chapter outline

5.1. Introduction

5.2. The non-destructive quantification method

- 5.2.1. Qualitative understanding of the peak broadening
- 5.2.2. Simplifying assumptions
- 5.2.3. A unified probabilistic approach
- 5.2.4. Problem formulation and its solution
- 5.2.5. Implementation of the method for the discretized problem
  - a. Parameters defining the Gaussian distribution
  - b. Discretization of the domain
  - c. Solving for the average orientational angle $\bar{\Phi}$
    - i. Using the dielectric function of the bulk material
    - ii. Using the dielectric function adapted for size and shape
  - d. Alternative faster graphical method of solving for B

5.3. Summary and conclusions

5.1. Introduction

Since the uniaxial alignment of an ensemble of NRs would accomplish the double goal of bringing the anisotropic optical properties to the macroscopic scale of practical applications while strongly enhancing the intensity of the local field, it is equally important to have an accurate knowledge of the degree of alignment achieved. So far, however, the alignment achieved was quantified more or less satisfactorily, depending on the alignment method. For example, the alignment of rods in liquid solutions could be

more accurately assessed by transmission electron microscopy (TEM), but the alignment of rods embedded in stretched polymer films could only be partially and approximately estimated by statistical calculations based on microscopic images.

In this regard, although all the available microscopic techniques such as scanning electron microscopy (SEM), TEM and cryo ultramicrotomy provide important morphologic information, they have several disadvantages, such as the shallow probing depth of the electron gun compared to the thickness of a composite film - in the case of using SEM, for instance. For this reason, the SEM micrographs suffer in quality, either because of insufficient resolution or because of the electrostatic charging of the polymer matrix in trying to increase the penetration of the electron beam, despite having sputtered layers of either gold or carbon. Even if the investigated sample does not become electrostatically charged and a perfect image is obtained, methods based on microscopy can only probe a very limited depth and surface area at a time and are therefore time consuming. Finally and most importantly, cutting out samples from the composite film renders that film unusable for the intended optical application. The microscopic methods are therefore destructive and in addition, expensive, difficult to carry out and hence, most often, incomplete. For these reasons, a non-destructive method capable of probing the entire volume of the sample and requiring easily available, inexpensive equipment is desirable. Such a method is proposed in this chapter.

To explain its derivation and verify its results, this method will be applied to the stretched composite film prepared and characterized so far, henceforth called the "reference film". The important features of relevance for this method development are: AuNRs of nominal diameter d_{nom} = 10 nm and length L_{nom} = 38 nm with 10%

dimensional variability, embedded in a matrix of polyvinyl alcohol (PVA). The alignment of its embedded rods has been quantified by statistical calculations based on SEM micrographs in the previous chapter. FIG.5.1(a) shows one of the SEM micrographs as well as the definition of the orientation angle φ of a typical rod with respect to the stretch axis (SA) of the film in the inset (i). The resulting average orientational angle of the AuNRs was $\bar{\Phi} = 3.5°$ within a range of $-30° \le \delta\varphi \le 30°$ as seen in the histogram of panel (b). These results will be used as reference for our proposed method.

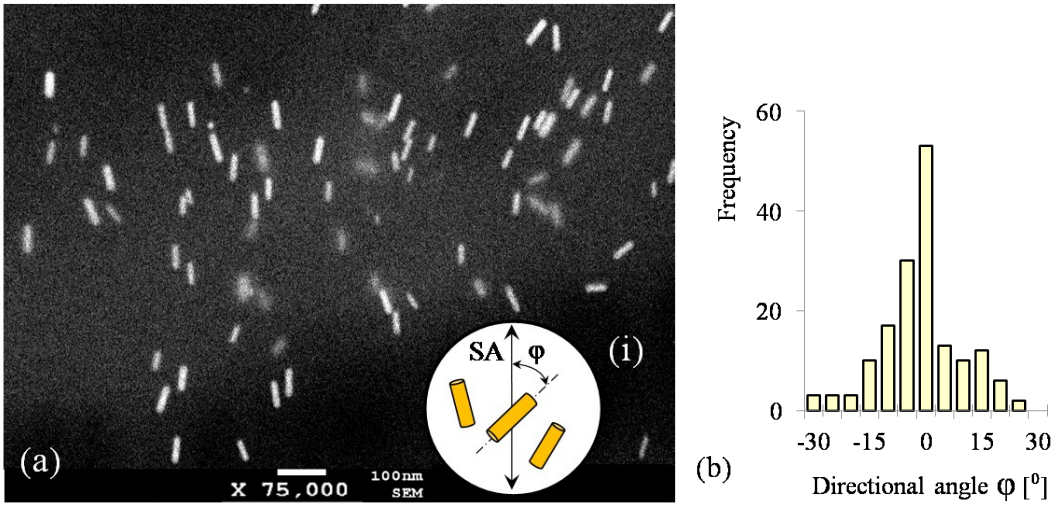

FIG. 5.1 (a) Micrograph component of the statistical significant sample (SSS). Inset (i) Schematic of typical AuNRs and definition of the orientation angle φ with respect to the stretch axis SA of the film. (b) Histogram of the orientation angles of the AuNRs measured based on micrographs of the SSS.

5.2. The non-destructive quantification method

5.2.1. Qualitative understanding of the peak broadening

Assuming the rods are free from impurities and embedded in a homogenous polymer matrix, any dissimilarity between their absorption spectra must be caused by the intrinsic properties of the rods, such as dimensions and orientations, irrespective of the surrounding medium. These properties will therefore be focused upon.

The description of the method starts by looking at the absorption spectra of the reference composite film illuminated by plane polarized light with the polarization direction angle θ with respect to the SA of the film, as shown in FIG. 5.2(a) and inset (i). Since the method focuses on the LSPR peak in light polarized parallel with SA (angle θ=0°), the LSPR peak was separated out from the panel (a) and superimposed it in panel (b) on two computer simulated spectra of the reference single AuNR. The two simulations have been run for two dielectric functions: 1) of the bulk gold and 2) the size and shape adapted dielectric function of gold, using the electron-surface scattering parameter $\alpha = 0.33$ as detailed in appendix A.

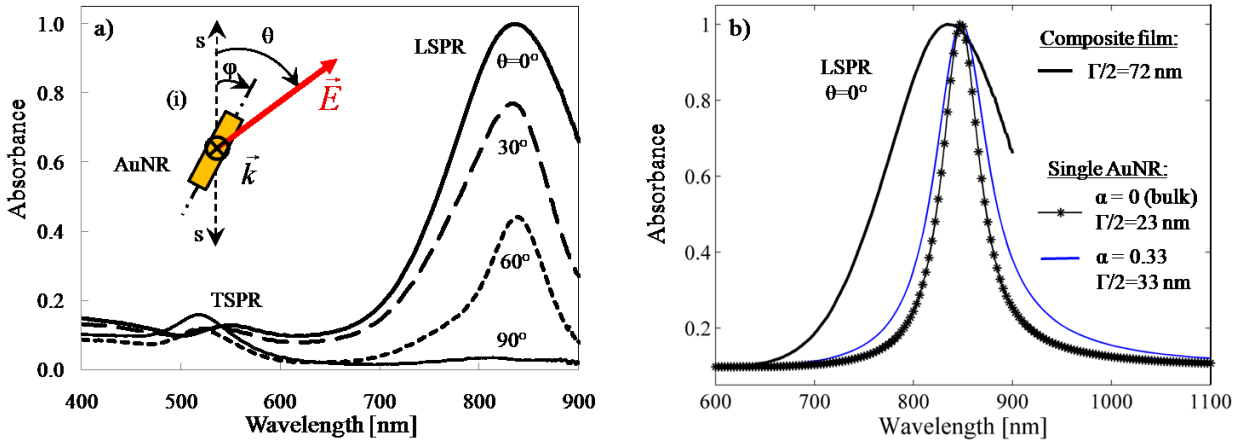

FIG. 5.2 (a) Polarized absorbance spectra of the reference stretched AuNR-PVA composite film. The angles θ and φ indicate the direction of polarization of the incident light beam and the orientation of a typical rod with respect to the SA of the film, respectively. (b) The measured LSPR spectrum for parallel polarization θ=0° superimposed on simulated spectra for two dielectric functions: of the bulk gold (asterisk marked black line) and size & shape adapted (blue thin line)

By measuring the widths of the absorbance peaks in panel (b) a full width at half maximum (FWHM) of $\Gamma_{composite}$ = 144 nm was found for the reference composite film,

which is much larger than the FWHM of the simulated spectra of the single rod: Γ_0 = 46 nm and $\Gamma_{0.33}$ = 66 nm for the bulk and the size & shape adapted dielectric functions, respectively. This width differential is due to the polydispersity and misalignment of the AuNRs, which can be justified qualitatively as follows.

Due to their polydispersity, the rods have different aspect ratios and hence different LSPR peak wavelengths. This is because the LSPR peak wavelength of a NR is directly proportional to the aspect ratio, in the electrostatic limit, as has been shown theoretically (Link et al. 1999; Link et al. 2005; Yan et al. 2003) and experimentally (Link et al. 1999; Link et al. 2005; Yan et al. 2003; Wilson et al., 2002; Brioude et al. 2005). Therefore, the distinct spectral positions of the peak wavelength of the AuNRs will broaden the LSPR peak of the ensemble of rods.

To determine the effect of the nonuniform orientation of the rods, a beam of linearly polarized light is considered falling at different incident angles on each rod, depending on its orientation. Because the rods have dichroic optical properties, as shown in Appendix B, the absorbance intensity of each rod depends on the relative angle between the incident polarized beam and the axis of the rod. Their relative orientation translates into more or less flattened LSPR peaks, which is equivalent to a more or less diminished contribution of those rods to the absorption of the ensemble.

With this insight, the quantification method was developed by adding up the individual absorptive contributions of all the rods modulated by their polydispersity dependent aspect ratios, orientations, and their number fraction to obtain the spectrum of the ensemble. An equation is further derived which related this spectrum of the ensemble

to the measured one of the reference film. The solution of this equation gave finally the average orientation angle, as it will be shown in the remainder of this chapter.

5.2.2. Simplifying assumptions

a) The absorbance spectra of the composite film were measured using a film of pure PVA as reference sample in the reference channel of the spectrophotometer. PVA of the same molecular weight was used in both the reference and the matrix of the composite film. In addition, the reference sample had been stretched by the same ratio as the composite film, to induce the same degree of anisotropy in both. Despite their initially equal thicknesses, the two films deformed with slightly different thicknesses during stretching. However, it is assumed here that the absorptive contribution of the PVA matrix had been accurately subtracted from the absorbance of the composite film and thus the measured absorbance represented the mere absorbance of the rods.

b) In addition, it is assumed that no static or dynamic charge transfer takes place between AuNRs and their embedding matrix or regions of interface with the matrix, which may affect the lifetime and the width of the LSPR peak (Kreibig, Gartz, Hilger & Neuendorf, 1999; Kreibig, 2008). The PVA matrix is therefore disregarded in the calculations. The only influence of the PVA matrix manifests itself through its refractive index that is used in the numerical simulations of the rod spectra. Consequently, the composite film is considered as consisting of a mere ensemble of free rods whose atoms relax only by emission of photons.

c) The rods are also assumed to be arranged in a single layer, as a two-dimensional array confined to the middle plane of the film. The spacing between rods is also

considered to be large enough such that they absorb light independently of each other. This approximation is reasonable since the average filling factor of the rods of 36 AuNRs/μm^3 is very small. Despite that, several plasmonically coupled rods may still exist, as seen in the micrograph of Fig. 5.1, but their number fraction calculated based on the SSS is negligibly small.

d) A typical rod is described by its random orientation angle φ measured between the long axis of the rod and the SA of the film, as depicted in the inset of Fig. 5.1. Its aspect ratio is defined as the ratio $\eta = L/d$ between length and diameter, respectively, which is assumed to take values within the range of variability $[\eta_{min}, \eta_{max}]$ allowed by the rod polydispersity. However, since L and d are independently distributed about their nominal values, two independent modeling variables would be needed to cover all possible dimensions. Therefore, in order to reduce the number of variables, the aspect ratio η was chosen as the only independent variable and the diameter d of a rod was linked to it.

e) It is additionally assumed that η varies randomly and continuously. The randomness assumption is justified because the dimensions of the rods result from a microscopic synthesis process that cannot be controlled by conditions imposed from its external macroscopic environment. As well, the continuity assumption is justified by the large size of the population of rods, of the order of $N_{tot} \sim 10^{12}$, with a similarly large number of dimensional categories that are separated by infinitesimally small spacing.

f) Since in deriving relationships for the ensemble the total absorption probability had to be averaged with respect to the orientation angle and the aspect ratio of a

typical rod, complementary assumptions of large enough cross section of the spotlight and uniform enough rod distribution had also been made, such that the rods lying within the lit area of the film reached the same extreme orientation angles $\bar{\Phi} \pm \delta\varphi$ as defined in FIG.5.3 and the same extreme aspect ratios η_{min} and η_{max} as limits of integration, irrespective of the position of the spotlight on the film surface.

5.2.3. A unified probabilistic approach

As postulated by quantum theory and schematically depicted in FIG. 5.4, light - matter interaction can be treated by considering that an irradiated atom jumps to one of its quantized states of higher energy W_2 by absorption of a photon, followed by relaxation of the atom to a state of lower energy W_1 while spontaneously emitting a photon. In both transitions, the photon has an angular frequency ω that satisfies the energy balance of the atomic states, i.e. $\hbar\omega = W_2 - W_1$.

The spontaneous emission of photons can be recorded by a detector and is considered a probabilistic event, which prompts a similar probabilistic interpretation of the more complex case of recording an absorption spectrum of a composite film, if the process can be properly broken down into more elementary events. Such an interpretation is proposed below.

The absorption spectrum of one AuNR of arbitrary aspect ratio η illuminated by a lightwave of arbitrary wavelength λ, polarized in the direction of the long axis of the rod and therefore $\theta = \varphi$, is considered first. As a result of the excitation and subsequent relaxation of the gold atoms, the almost simultaneously emitted photons are recorded superimposed on each other by the detector of the spectrophotometer, as schematically

depicted in FIG. 5.4. If the wavelength of light is allowed to vary within the range of interest, the signal can be recorded as an absorbance spectrum by the detector, which is denoted by $A^{\parallel}_{1NR}(\eta,\lambda)$. Actually, the absorbance depends on both diameter d and aspect ratio η of the rod because they both define the three-dimensional confinement of the conductions electrons and also because the dielectric function of gold depends on the size and shape of the particle. But, as mentioned in section B(c), d and η had been linked together in pairs to reduce the dimensionality of the problem.

For each wavelength of the incident radiation, the intensity of absorbance of this spectrum is proportional to the total probability of spontaneous emissions of photons by the atoms that make up the rod. Conversely, the total probability of the radiative transitions that occur in the atoms of a rod illuminated by a lightwave plane polarized parallel to the long axis of the rod, which is denoted by $P_1(\lambda, \varphi = \theta)$, is proportional to the absorbance recorded at the respective wavelength λ. Therefore:

$$P_1(\eta,\lambda,\varphi=\theta) \propto A^{\parallel}_{1NR}(\eta,\lambda) \qquad (1)$$

If the polarization of the incident lightwave is not parallel to the long axis of the rod but makes an arbitrary angle $\theta \neq \varphi$, the excited atoms of the AuNR relax by emitting photons with a probability that follows the cosine-squared law (Appendix B). The emission probability in this case can be tentatively written in the following way:

$$P_2(\lambda,\varphi\neq\theta) = C\cos^2(\varphi-\theta) \qquad (2a)$$

where C is a factor of proportionality, constant with respect to φ and θ, but possibly dependent on other variables. Since P_2 has to be a continuous function of θ, it will also have to satisfy the previous case in the limit as $\theta \rightarrow \varphi$, that is:

$$A^{\,\mathrm{II}}_{1NR}(\eta,\lambda) = \lim_{\theta\to\varphi} P_2(\lambda,\varphi\neq\theta)$$
$$= C\lim_{\theta\to\varphi}\cos^2(\theta-\varphi) = C \qquad (2b)$$

Substituting C of (2b) into (2a) gives the probability of photon emission in the more general case of arbitrary θ and φ angles as:

$$P_2(\eta,\lambda,\varphi,\theta) = \cos^2(\varphi-\theta)A^{\,\mathrm{II}}_{1NR}(\eta,\lambda) \qquad (3)$$

In order to interpret probabilistically the dimensional non-uniformity of the rods, the rods are classified into dimensional categories specified by the aspect ratio η. The probability of finding N(η) rods of aspect ratio η out of the total number N_{tot} of rods that make up the ensemble is denoted by $P_3(\eta)$. By analogy with the method of Truong, (1976), η is also considered as the realization of a random variable of distribution described by a continuous probability distribution function (PDF). For simplicity, this PDF was chosen to be Gaussian, that is:

$$P_3(\eta) = \frac{N(\eta)}{N_{tot}} = G(\eta) = \frac{1}{\sqrt{2\pi}\sigma}\exp\left[-\left(\frac{\eta-\bar{\eta}}{\sqrt{2}\sigma}\right)^2\right] \qquad (4)$$

where "$\bar{\eta}$"and "σ" are the mean and the standard deviation of the population of AuNRs.

The above particular cases can be finally compounded as sub-events of the most general case of a AuNR of arbitrary geometry η, arbitrary orientation angle φ and illuminated by light plane polarized at an arbitrary angle θ. In this general case, the resulting radiative transitions of the gold atoms take place with a total probability denoted by P_{tot} (η, λ, φ, θ) that is equal to the joint probability of its sub-events, or their product, since the three sub-events are independent. Therefore, the absorbance spectrum obtained by recording the radiative transitions of a rod in this most general case is:

$$A_{1NR}(\eta,\lambda,\varphi,\theta) \propto P_{tot}(\eta,\lambda,\varphi,\theta)$$
$$= P_2(\lambda,\varphi,\theta)P_3(\eta)$$
$$= G(\eta)\cos^2(\theta-\varphi)A^{\,\mathrm{II}}_{1NR}(\eta,\lambda) \qquad (5)$$

5.2.4. Problem formulation and its solution

Since the light beam of the spectrophotometer has a macroscopic cross section at its point of incidence on the composite film, a very large number of atoms are excited simultaneously. In their subsequent spontaneous relaxation, these atoms emit a correspondingly large number of photons that will reach the detector simultaneously and the signal recorded will therefore consist of the superposition of signals of all photons.

In order to express the superposition of photons originating from rods of different orientations, the expression (5) is averaged with respect to φ over an interval centered at the average alignment angle $\bar{\Phi}$ of the rods, defined in FIG. 5.3, which is the unknown of the problem.

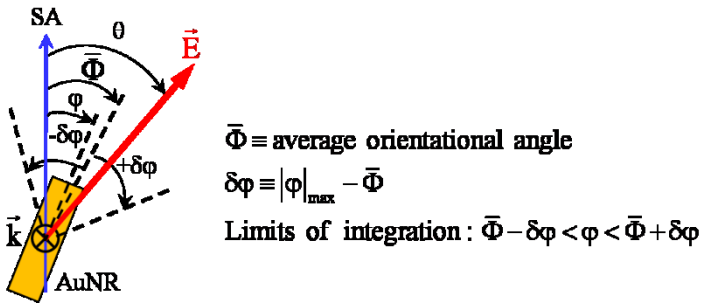

FIG. 5.3 Definition of interval centered at the average alignment angle of the rods used in the averaging of the total probability with respect to the orientational angle. SA is the stretch direction of the film

The following absorbance is obtained:

$$
\begin{aligned}
&A_{1NR}(\eta,\lambda;\theta-\bar{\Phi},\delta\varphi) \quad = \\
&= \quad \frac{1}{2\delta\varphi}\int_{\bar{\Phi}-\delta\varphi}^{\bar{\Phi}+\delta\varphi} A_{1NR}(\eta,\lambda,\varphi,\theta)d\varphi \\
&= \quad \frac{1}{2\delta\varphi}G(\eta)A^{\,\mathrm{II}}_{1NR}(\eta,\lambda)\int_{\bar{\Phi}-\delta\varphi}^{\bar{\Phi}+\delta\varphi}\cos^2(\theta-\varphi)d\varphi \\
&= \quad \frac{1}{2}\left[1+\frac{\sin(2\delta\varphi)}{2\delta\varphi}\cos\left(2(\theta-\bar{\Phi})\right)\right]G(\eta)A^{\,\mathrm{II}}_{1NR}(\eta,\lambda) \\
&= B(\theta-\bar{\Phi},\delta\varphi)G(\eta)A^{\,\mathrm{II}}_{1NR}(\eta,\lambda) \qquad (6a)
\end{aligned}
$$

where

$$
B(\theta-\bar{\Phi},\delta\varphi)\equiv\frac{1}{2}\left[1+\frac{\sin(2\delta\varphi)}{2\delta\varphi}\cos\left(2(\theta-\bar{\Phi})\right)\right] \qquad (6b)
$$

is a function of θ, while $\bar{\Phi}$ and $\delta\varphi$ are constant parameters that define the mean and the maximum deviation from the mean of the averaging interval, respectively.

By averaging the absorbance of the initially randomly oriented array, another absorbance has been formally obtained, namely that of another array, consisting of rods uniformly oriented at the average angle $\bar{\Phi}$, with preserved dimensions and locations and of equivalent overall absorbance spectrum.

Making the assumption of independent absorbers of section B.(c), the irradiance transmitted by the ensemble can be expressed as the sum of the irradiances transmitted by each component rod of all possible dimensional categories η, as expressed in (7a) below. The irradiance of a rod can also be written in terms of its absorbance, as in (7b), from which, by using (5), (7c) is obtained. On the other side, the irradiance of the ensemble can also be expressed in terms of its absorbance, as in (7d).

$$I_{ensemble}(\lambda,\theta-\bar{\Phi},\delta\varphi)=$$

$$=\int_{\eta_{\min}}^{\eta_{\max}} I_{1NR}(\lambda,\eta;\theta-\bar{\Phi},\delta\varphi)d\eta \qquad (7a)$$

$$=I_0\int_{\eta_{\min}}^{\eta_{\max}} 10^{-A_{1NR}(\eta,\lambda;\theta-\bar{\Phi},\delta\varphi)}d\eta \qquad (7b)$$

$$=I_0\int_{\eta_{\min}}^{\eta_{\max}} 10^{-G(\eta)B(\theta-\bar{\Phi};\delta\varphi)A^{\perp\!\!\!\perp}_{1NR}(\eta,\lambda)}d\eta \qquad (7c)$$

$$=I_0 10^{-A_{ensemble}(\lambda,\theta-\bar{\Phi},\delta\varphi)} \qquad (7d)$$

From (7c) and (7d) the absorbance of the ensemble is then obtained, expressed as a process of integration of the absorptive contributions of the constituent rods as follows:

$$A_{ensemble}(\lambda,\theta-\bar{\Phi},\delta\varphi)=-\log_{10}\int_{\eta_{\min}}^{\eta_{\max}} 10^{-G(\eta)B(\theta-\bar{\Phi};\delta\varphi)A^{\perp\!\!\!\perp}_{1NR}(\lambda,\eta)}d\eta \qquad (8a)$$

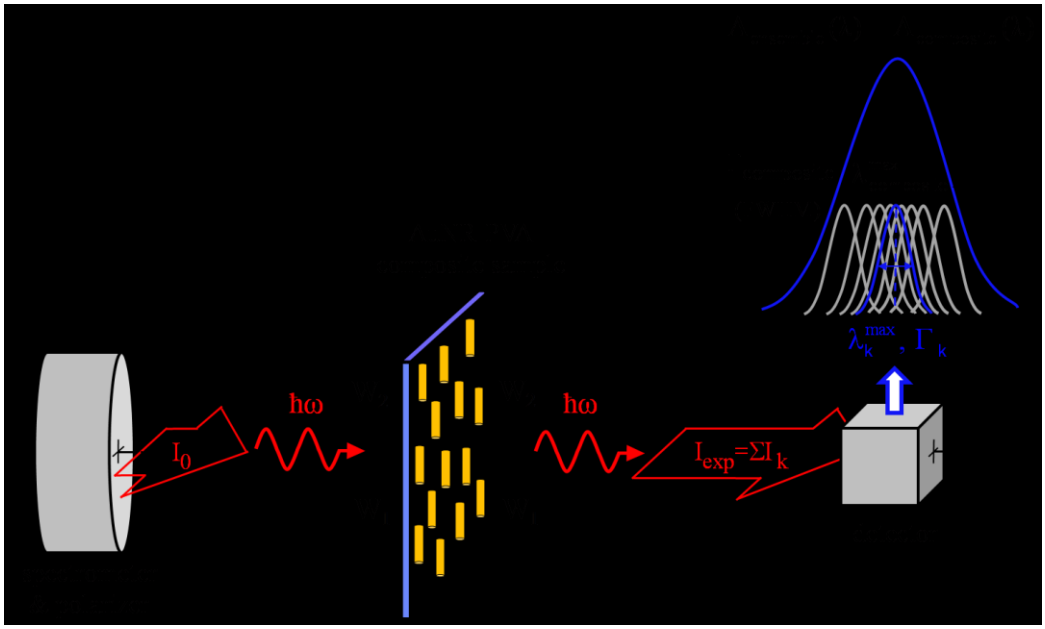

FIG. 5.4 Schematic of atomic transitions taking place within each illuminated AuNR: absorption of photons resulting in the excitation of the atoms by followed by their relaxation by spontaneous emission of photons. The emitted photons are captured superimposed on each other by the

detector, which is recorded as an absorption spectrum. The index k is associated with each illuminated nanorod, all assumed to lie far apart from each other such that not to interact electromagnetically.

Since by using a reference sample the absorptive contribution of the PVA matrix had been effectively cancelled, as assumed in section B(a), it results that the absorbance of the ensemble of rods must be equal to the measured absorbance of the composite film, or $A_{composite} = A_{ensemble}$ for every wavelength λ and polarization direction θ, as schematically depicted in FIG. 5.4.

The main relationship of this method, equation (8b), is thus obtained that is:

$$A_{ensemble}(\theta,\lambda) \equiv -\log_{10} \int_{\eta_{\min}}^{\eta_{\max}} 10^{-G(\eta)B(\theta-\bar{\Phi};\delta\varphi)A^{\parallel}_{1NR}(\lambda,\eta)} d\eta = A_{composite}(\theta,\lambda),\ (\forall)\,\theta,\lambda \qquad (8b)$$

This identity relates the average orientational angle $\bar{\Phi}$ to the absorbance spectrum of the composite film measured for an arbitrary polarization direction θ and wavelength λ. In this equation, the function $B(\theta-\bar{\Phi};\delta\varphi)$ defined by (6b) will be regarded as an independent variable, in which role it is henceforth denoted simply by "B" with possible values in the range of the function $B(\theta-\bar{\Phi};\delta\varphi)$. Since the right hand side of (8b) is experimentally known, it is subsequently aimed for solving (8b) for B.

However, (8b) holds for all possible wavelengths λ and polarization angles θ of the interval of interest, which is equivalent to an infinite number of equations in B. It is therefore assumed that the ensemble and the measured spectra are identical if and only if the widths and peak intensities of their LSPR are simultaneously equal. This interpretation of (8b) is equivalent to the following two equations:

$$\Gamma_{ensemble}(B) = \Gamma_{composite} \qquad (9a)$$

$$\left[\max A - \min A\right]_{ensemble} = \left[\max A - \min A\right]_{composite} \qquad (9b)$$

Thus, B is the only unknown of the equations (9) that are solvable, in principle. One way of solving (9a) for B is by trial and error, for example, as follows.

For an allowed value of B, the LSPR of the simulated ensemble is plotted, scaled up or down until (9b) is satisfied, its FWHM is graphically measured and compared with the FWHM of the experimental LSPR. These steps repeated for different B-values until the FWHM of the simulated ensemble LSPR equals the FWHM of the experimental LSPR, which solves the equations (9) for B. Let this solution be denoted by B*.

The above solution procedure can also be formally expressed in terms of an inverse function that is applied to (9a), as follows:

$$B^* = \Gamma^{-1}_{ensemble}\left(\Gamma_{ensemble}(B)\right) = \Gamma^{-1}_{ensemble}\left(\Gamma_{composite}\right) \equiv \mathrm{f}(\Gamma_{\boldsymbol{composite}}) \qquad (10)$$

which highlights that the solution B* is some function "f" of the experimental data. Finally, substituting the definition (6b) into (10) the following trigonometric equation in $\bar{\Phi}$ is obtained:

$$\frac{1}{2}\left[1 + \frac{\sin(2\delta\varphi)}{2\delta\varphi}\cos\left(2(\theta - \bar{\Phi})\right)\right] = B^* = \mathrm{f}(\Gamma_{\boldsymbol{composite}}) \qquad (11)$$

in which the right hand side is an experimentally known value. Solving (11) for $\bar{\Phi}$ is trivial, the resulting solution will depend on δφ and θ as parameters and in principle the problem is solved.

5.2.5. Implementation of the method for the discretized problem

For the implementation of this method, the maximum deviation angle $\delta\varphi = 30°$ will be chosen as a realistic value, as suggested by the SEM-based histogram of FIG.5.1, while the incident polarization will be parallel to the SA of the film, or $\theta = 0°$. In that case, the range of the function $B(\theta - \bar{\Phi}; \delta\varphi)$ was obtained as:

$$0.0865 \le \mathrm{B}(\theta - \bar{\Phi}; \delta\varphi) \le 0.9135 \quad \text{for} \quad \delta\varphi = 30°, \theta = 0° \qquad (12a)$$

$$0 \le \mathrm{B}(\theta - \bar{\Phi}; \delta\varphi) \le 1.0 \quad \text{for} \quad \delta\varphi = 0°, \theta = 0° \qquad (12b)$$

a. *Parameters defining the Gaussian distribution*

Assuming a 10% dimensional dispersion about the nominal dimensions, the aspect ratio is chosen as the only independent variable that describes the geometry of a rod. The mean aspect ratio of the Gaussian distribution was imposed to be equal to the nominal value of $\bar{\eta} = \left(L/d\right)\big|_{nom} = 3.8$ with its extreme values calculated as: $\eta_{\min} = L_{\min}/\mathrm{d}_{\max} = (0.9 / 1.1)\eta = 3.11$ and $\eta_{\max} = 2\bar{\eta} - \eta_{\min} = 4.49$ such that $\bar{\eta} = (\eta_{\max} + \eta_{\min})/2$

The standard deviation "σ" was determined such that the width of the Gaussian distribution was large enough to ensure that the area under the PDF was close to 100%, which comprised most of the total event. Consequently, the distribution width was chosen as: $\eta_{\max} - \eta_{\min} = 6 \cdot \sigma$ for which the area under the Gaussian PDF was 99.73% of the total event [23]. By imposing this condition, the standard deviation was determined as σ = (4.49 – 3.11)/6 = 0.23.

b. Discretization of the domain

Since the dielectric function of gold at the size of our nanorods is both size and shape dependent, as described in Appendix A, two independent variables are required, such as the aspect ratio η and diameter d. However, allowing η and d to independently assume random values, would be prohibitively time consuming even for a discretized solution. Therefore, the domain of the problem is discretized by choosing a seven-point equidistant partition of the η- and d-domains and η and d are also linked together in pairs as shown below:

$$\{(\eta, d)_k, k = 1 \text{ to } 7\} = \{(3.11; 11.0),\ (3.34; 10.7),\ (3.57; 10.3),\ (3.8; 10.0),\ (4.03;\ 9.67),\ (4.26; 9.33),\ (4.49; 9.0)\}. \quad (13)$$

This linkage further reduced the number of required simulations of spectra and distinct dielectric functions from 49 to seven. The charts of the size and shape adapted dielectric functions are displayed in FIG. A.1 of appendix A.

c. Solving for the average orientational angle $\bar{\Phi}$

Obtaining the absorbance spectra $A^{\parallel}_{1NR}(\eta, \lambda)$ of a single AuNR in parallel polarized light is the first step of this method, as described above. Since the dielectric function of gold is size and shape dependent, the spectra had to be determined by numerical simulations for each of the seven dimensional categories η, it will be looked at both possible cases of dielectric function: (a) of the bulk gold, to serve as reference and (b) size and shape adapted. The range of the simulation wavelength spanned from 600 to 1200 nm, which was large enough to allow for the definition of baselines and graphical measurement of the FWHM of all LSPR bands.

i) Using the dielectric function of the bulk material

The typical calculation steps of the procedure are displayed in FIG. 5.4. In panel (a), the simulated absorbance spectra $A^{\perp\!\!\!\perp}_{1NR}(\lambda,\eta_k)$ of the dimensional categories η_k, $1 \le k \le 7$ of the rods is displayed, normalized and superimposed on the spectrum of the composite film shown as the continuous black curve, for comparison. Multiplying each spectrum by its corresponding Gaussian weight shown in panel (b), the contribution of the respective dimensional category of rods to the spectrum of the ensemble, is obtained as shown in panel (c).

To compute the spectrum of the ensemble, the integral of equation (7c) is approximated using its Riemann sum over the discretized domain as follows:

$$I_0 10^{-A_{ensemble}(\lambda)} = I_{ensemble}(\lambda) = I_0 \int_{\eta_{\min}}^{\eta_{\max}} 10^{-G(\eta)B(\theta-\bar{\Phi},\delta\varphi)A^{\perp\!\!\!\perp}_{1NR}(\eta,\lambda)} \cdot d\eta$$

$$\approx \frac{\eta_{\max}-\eta_{\min}}{6} I_0 \sum_{k=1}^{7} 10^{-G(\eta_k)B(\theta-\bar{\Phi},\delta\varphi)A^{\perp\!\!\!\perp}_{1NR}(\eta_k,\lambda)} \qquad (14a)$$

The absorbance spectrum of the ensemble is then expressed as:

$$A_{ensemble}(\lambda) \approx C_1 - \log_{10} \sum_{k=1}^{7} \left[10^{-G(\eta_k)A^{\perp\!\!\!\perp}_{1NR}(\lambda,\eta_k)} \right]^{B(\theta-\bar{\Phi};\delta\varphi)}$$

$$\approx -\log_{10} \sum_{k=1}^{7} \left[10^{-G(\eta_k)A^{\perp\!\!\!\perp}_{1NR}(\lambda,\eta_k)} \right]^{B(\theta-\bar{\Phi};\delta\varphi)} \qquad (14b)$$

where $C_1 = -\log_{10}\left[(\eta_{\max}-\eta_{\min})/6\right]$ is a constant. Since C_1 only translates the spectrum up and down along the absorbance axis while leaving its shape unchanged, C_1 will be disregarded in all subsequent calculations.

Using a loop of a few MATLAB code lines, the spectrum of the ensemble is then calculated according to the defining equation (14b) for B=1. The resulting spectrum is displayed as the blue dash-dotted curve overarching the weighted spectra of the single rods, in panel (c) as well. For a better comparison with the experimental spectrum, the spectrum of the ensemble was also scaled up and translated to match the baseline and the peak of the composite spectrum. It is noticed that the LSPR of the ensemble is narrower than the LSPR of the composite while the peak wavelength of the ensemble is very close to the LSPR peak of the nominal rod, but slightly displaced from peak of the composite LSPR.

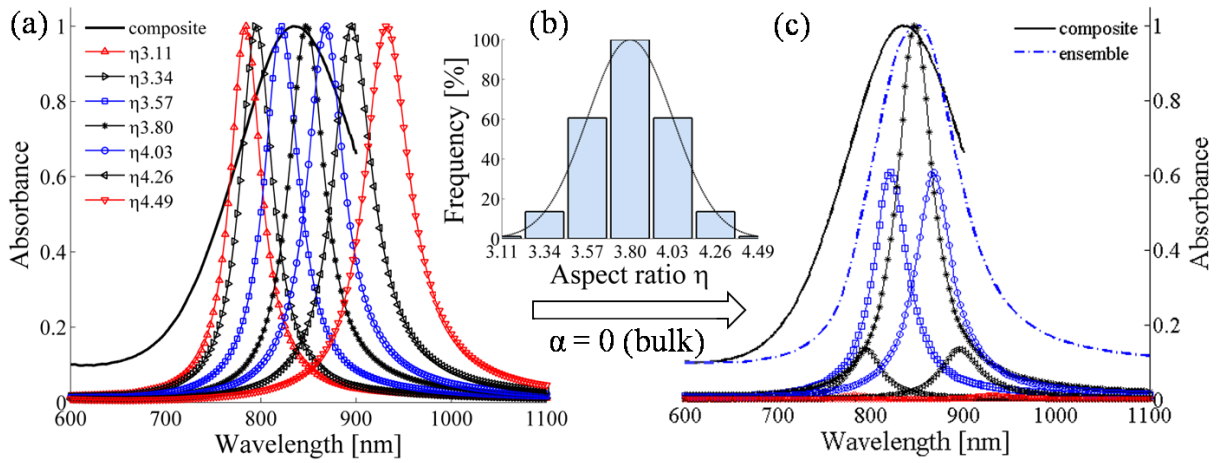

FIG. 5.5 Simulated absorbance spectrum of an ensemble of AuNRs for the bulk dielectric function and B=1. (a) Normalized spectra of the seven categories of rods, denoted by their aspect ratios "η". (b) The Gaussian weights assigned to each η-category. (c) The spectra of panel (a) weighted by Gaussian weights. The spectrum of the ensemble, the blue dash-dotted line, was obtained by summing up the weighted spectra according to the definition relationship (14b).

By treating the function $B(\theta - \bar{\Phi}, \delta\varphi)$ as an independent parameter, denoted by "B" and allowing it to take values in the maximum range (12), a family of ensemble spectra

defined by (14b) is generated and denoted by $y_0(B, \lambda)$, which is rewritten below for convenience:

$$y_0(\lambda, B) = -\log_{10}\left[\sum_{k=1}^{7}\left(10^{-G(\eta_k)A^{11}_{1NR}(\lambda,\eta_k)}\right)^{B}\right], \quad 0 \le B \le 1.0 \qquad (15)$$

To approximate the range of the FWHM of the y_0-spectra, the y_0-curves are plotted for the values B = 0.2*k, 0≤k≤5 that covers the maximal range [0, 1] of B. For the dielectric function of bulk gold, these spectra are shown in the panel (a) of FIG. 5.6 below. The goal is to find the value of B for which the lineshape of y_0 has the same FWHM as the composite film.

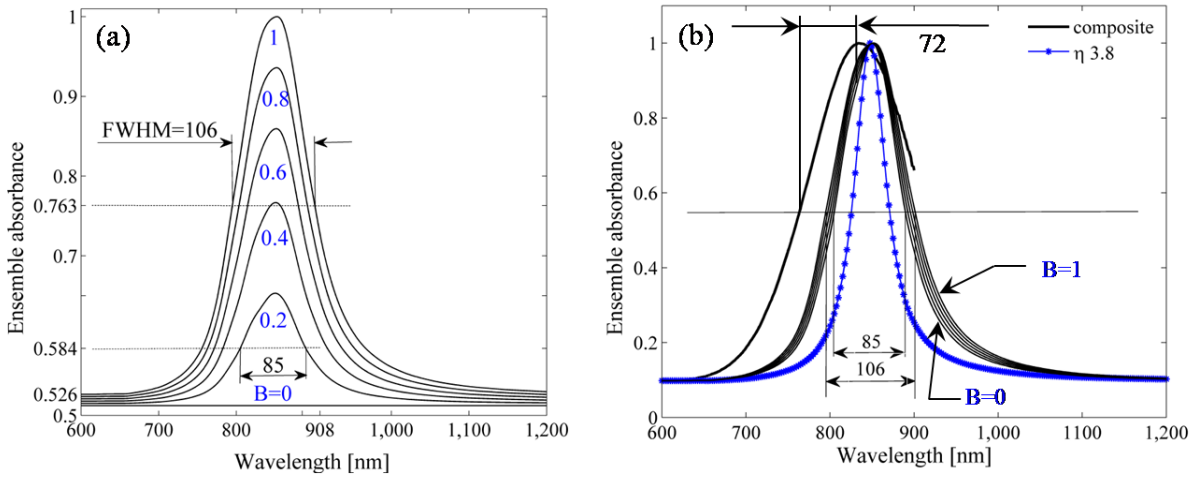

FIG. 5.6 Two equivalent representations of ensemble spectra $y_0(\lambda,B)$ defined by (15) for 0 ≤ B ≤ 1 and the bulk dielectric function of gold. (a) The peaks of the spectra are both allowed to vary with B. (b) The same y_0 spectra of (a) translated and scaled in the y-direction to match the baseline and the peak of the experimental spectrum.

First, however, the correctness of (15) can be qualitatively verified starting with the straight horisontal spectrum at the bottom of panel (a) of FIG. 5.5, which is obtained for B = 0. In the definition (6b) of the function B, it is seen that B = 0 only if both δφ = 0° and $\theta - \bar{\Phi} = 90°$. The physical meaning of these values is that: 1) all the rods are

perfectly aligned with the stretch direction, i.e. the maximum deviation from the mean angle $\bar{\Phi}$ is equal to $\delta\varphi = 0°$ and 2) the incident light is polarized perpendicular to the long axis of the rods, or $\theta - \bar{\Phi} = 90°$. But this is one of the limit cases in which only the TSPR mode of the rods was excited, while the LSPR mode was not excited and its lineshape was a horisontal spectral line, of constant intensity. This is exactly what the curve at the bottom of FIG. 5.6 (a) looks like, and terefore, the case B = 0 recovers the experiment, which is a first verification of formula (15) and of the calculation procedure.

It is also noticed that both the width and intensity of the spectra y_0 vary with B, which makes it harder to pinpoint the B-value for which the FWHM of the ensemble and the composite spectra match each other. To facilitate the comparison, each curve $y_0(\lambda, B)$ is transformed by translation and scaling in the y-direction to bring them to the same baseline and peak as the composite spectrum. Since these transformations do not modify the FWHM of the spectra, the transformed spectra of panel (b) are equivalent to the original ones of panel (a).

However, by measuring the FWHM of the y_0-lineshapes, a maximal value of 106 nm is found for B = 1 and the value of FWHM = 144 nm of the composite film cannot be matched by any ensemble spectrum y_0 for any B-value. It is thus concluded that the equations (9) do not admit any solution.

It is realized that the narrower width of the ensemble spectrum was due to simulations of spectra based on the bulk dielectric function of gold. Thus, it is expected that, using instead the size and shape adapted dielectric function, broader plasmon bands of the single rods will result, which will alleviate the width discrepancy between ensemble and experiment. This is because the size and shape corrections take into

account the shorter MFP experienced by the conduction electrons, which results in an increased number of collisions and a shorter lifetime of the excited states of the gold atoms. According to the uncertainty principle, the shorter lifetime will increase the energy uncertainty, which is equivalent to the broadening of the spectra. It is concluded that the dielectric function of gold has to be corrected for size and shape.

ii) Using the dielectric function adapted for size and shape

In order to apply the size and shape correction formulae of Appendix A, the electron-surface scattering parameter was adopted with a value of $\alpha = 0.33$ from the single nanorod experiments[11, 31, 32].

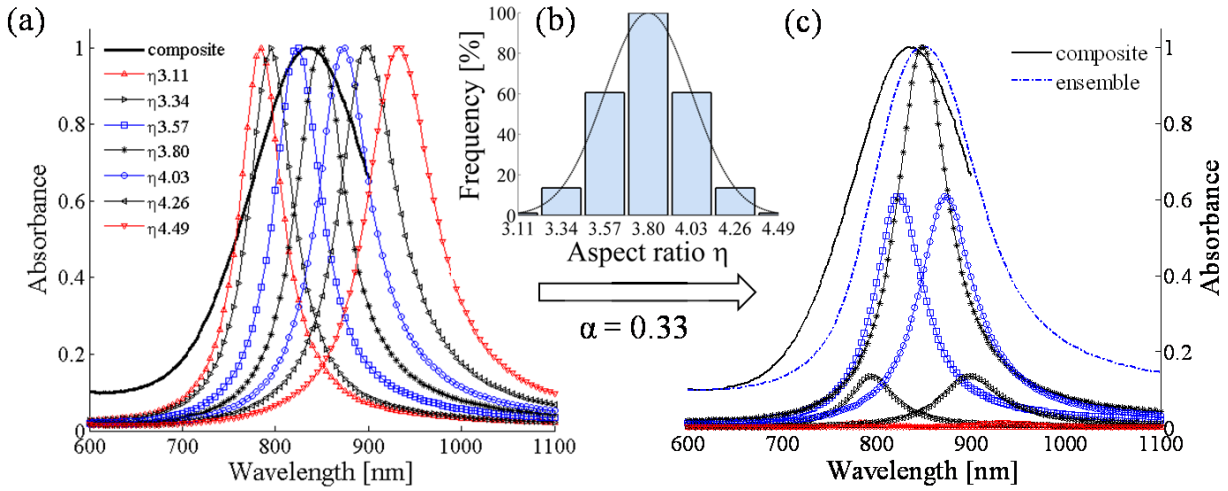

FIG. 5.7 (a) Normalized spectra of the seven categories of rods simulated for the size & shape adapted dielectric function using $\alpha = 0.33$ and B=1. (b) Gaussian weights assigned to each η-category. (c) Absorbance spectrum (dash-dotted line) of the rod ensemble.

As expected, the size and shape correction of the dielectric function has broadened the ensemble spectrum, which can be assessed in the panel (c) of FIG 5.6.

To find out exactly the new LSPR peak width, the procedure presented above is repeated, translating and scaling up the spectra in the y-direction to bring them to the

same baseline and LSPR peak as the LSP peak of the composite film. Carrying out this transformation revealed however that the ensemble spectra generated for $0 \leq B \leq 1$ have a maximum of FWHM ≤130 nm for B = 1, as seen in FIG. 5.8.

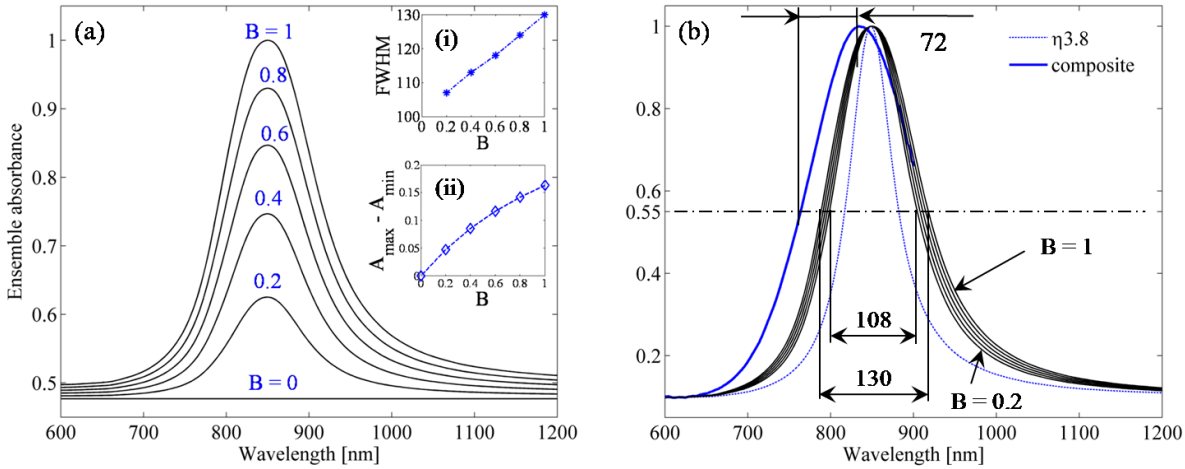

FIG. 5.8 Equivalent absorbance spectra of the rod ensemble for the corrected dielectric function of gold, using $\alpha = 0.33$ (a) The peak and the width of the spectrum are both allowed to vary with B. (b) The same spectra translated and scaled in the y-direction to match the LSPR baseline and peak of the composite film.

Although using the size and shape corrected dielectric function has broadened the ensemble spectrum, the LSPR peak is still narrower than the LSPR peak of the composite film and, as a result, the equations (9) still cannot be solved for B.

One of the reasons may be other dampening processes, such as the dampening at the chemical interface that would shorten the lifetime of the excitation states and thus broaden the spectra. However, their effect is likely very small, as per simplifying assumption B (b).

However, another more probable and important cause may be affecting the result. Namely, the 10% polydispersity of the nanorods was likely an underestimation. Qualitatively, this is plausible, because the more different the aspect ratios of the rods are, the larger the separation of their LSPR peak wavelengths, which broadens the peak of their ensemble LSPR. To get a sense of how large the rod polydispersity would need to be to allow for a solution of (9), the absorbance spectra of the individual rods are simulated for a few polydispersities of increased value, their ensemble spectra are calculated and their FWHM are graphically measured for the reference value of B = 1, with results listed in Table 5.1 below:

Table 5.1 Measured FWHM values for given polydispersities and values of the parameter B

Polydispersity [%]	13	14	15
Parameter B	FWHM [nm]		
1.0	143.5	150	157
0.91	141	147	153.5

The simulations confirmed the broadening trend of the ensemble LSPR peak beyond the FWHM=144 nm of the composite film, which proved that the equations (9) admit a solution B* for a polydispersity between 13% and 14%.

However, determining the exact value of the polydispersity that allows for solving (9) is a different problem. Had it not ben assumed that the rod polydispersity is 10%, TEM analyses of the rods in aqueous solution would have been carried out to exactly determine the polydispersity, which is a more efficient method. Now, it is not meaningful to continue by trial and error to find out the required polydispersity, which can certainly be done. On the contrary, it is meaningful to prove that the problem has a solution if the polydispersity of the rods is precisely known.

To prove it, the statistically determined solution mentioned in the introduction will be used. Thus, for the average orientation angle of $\bar{\Phi} = 3.5°$, the maximum angle deviation $\delta\varphi = 30°$ and θ = 0° a value of 0.91 of the function $B(\theta - \bar{\Phi}, \delta\varphi)$ is calculated according to (6b). Using the above simulations of the single rods spectra for 13%, 14% and 15% polydispersity, the ensemble spectra $y_0(\lambda, B)$ is calculated and plotted for B=0.91. Their measured FWHM is added in the second row of Table I and finally interpolated linearly between the columns of polydispersity 13% and 14%. It is found that an ensemble of 13.5% rod polydispersity has the width of its LSPR peak of exactly FWHM = 144 nm. With the hindsight of these results, the correct data of the problem that allow for a solution, can now be reformulated as follows.

Given a stretched composite film containing rods of 13.5% polydispersity it will be found that its LSPR peak has a FWHM equal to the peak width of the composite film $\Gamma_{composite}$ = 144 nm for exactly B*=0.91. Plugging this B*-value in the equation (11) and choosing a maximum angle deviation $\delta\varphi = 30°$ the solution $\bar{\Phi} = 3.5°$. is obtained. This completes the demonstration that the problem admits a solution in agreement with the statistical calculation based on SEM analyses, which verifies the proposed theoretical quantification method.

d. Alternative faster graphical method of solving for B

The above procedure involves several time consuming steps, but fortunately, once all calculations are completed, their results can be reused for future alignment quantifications of rods of the same material and nominal dimensions but of different polydispersities and FWHM of the composite film.

In order to reuse the above results, the FWHM of the LSPR bands are stored in columns for each polydispersity from 11% to 15% and value of B from 0.5 to 1.0, similar to the chart data of FIG.5.9. Trend lines are then fit to the FWHM of the same B-value. The fitting adequacy in terms of the determination coefficients R^2 listed in Table II show that second order polynomial fitting curves give consistently coefficients R^2 closer to 1 than the first order polynomials. Taking into account that a partition of only 7- point of the problem domain was used, the good adequacy of the fitting curves are considered to be a confirmation of the validity of the procedure.

To solve for B, the chart is used as follows: the measured FWHM = 144 nm and the known polydispersity of 13.5% intersect at a point through which another curve of constant B must pass. To find the B-value of this curve, it is interpolated linearly between the two neighboring B values and obtain a value of B*= 0.9098.

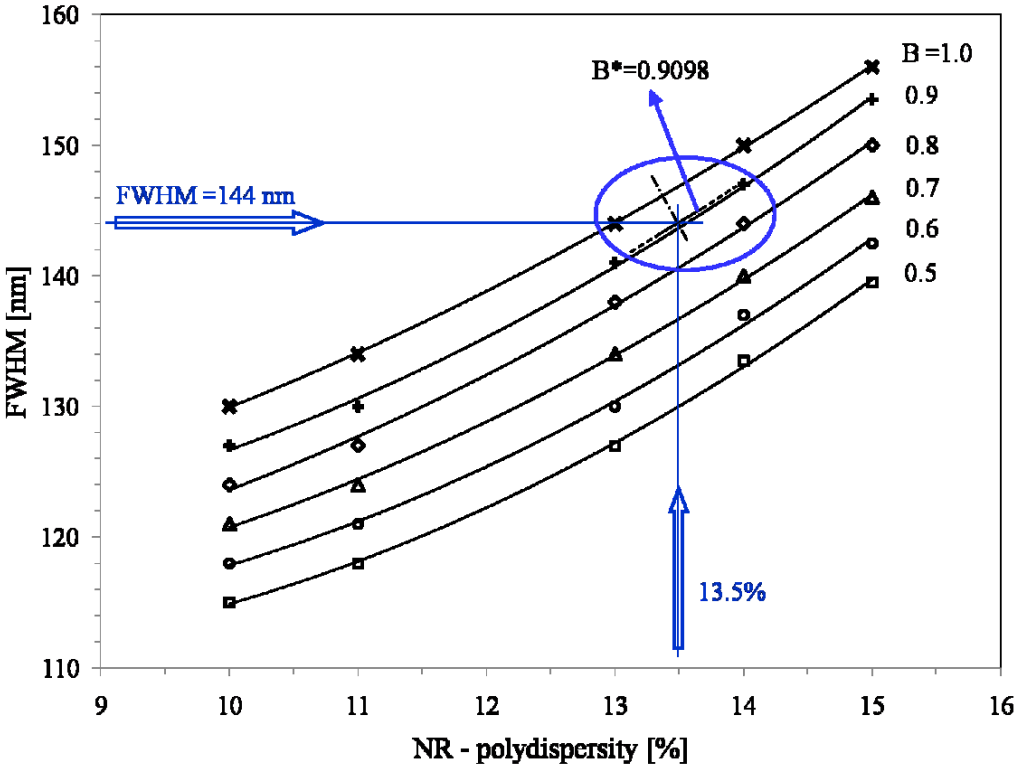

FIG. 5.9 Graphically solving for B using the FWHM of the film and the rod polydispersity

Table 5.2. Adequacy of second vs. first order fitting polynomials:

Parameter B	Coefficient of determination R^2	
	2-nd order	1-st order
0.5	0.9992	0.9867
0.6	0.9978	0.9866
0.7	0.9991	0.9911
0.8	0.9982	**0.9926**
0.9	0.9987	**0.9812**
1.0	0.9999	0.9956

Equation (11) is then solved for $\bar{\Phi}$ using $\delta\varphi = \pi/6$ and $\theta = 0$ and obtain:

$$\cos\left(2(\theta-\bar{\Phi})\right) = (2B^*-1)\frac{2\delta\varphi}{\sin(2\delta\varphi)} = 0.8196\frac{2\pi}{3\sqrt{3}} = 0.9911$$

which finally leads to an average angle of $\bar{\Phi} \approx 3.8°$. This result is 8.6% off the statistical result of $\bar{\Phi} = 3.5°$ that was shown in the introductive chapter, but the agreement is sufficiently good to confirm the principle of the non-destructive method. Obviously the agreement of the two results can be improved by increasing the accuracy of both methods of calculation.

5.3. Summary and conclusions

The current method of assessing the alignment of rods in stretched polymer films is based on statistical calculations and SEM micrographs, which requires cutting of samples from the film, which is destructive in nature. In addition, the dimensions and

positions of the rods necessary for the calculation of the orientation angles are subject to measurement errors. In contrast, the method presented above quantifies the alignment non-destructively, as summarized below:

Using a probabilistic approach and numerically simulated absorbance spectra of a selection of representative single rods, the LSPR spectrum of the ensemble is calculated. This calculation also involves the average orientation angle $\bar{\Phi}$ of the rods through a parameter denoted by "B" whose value is determined by imposing that the LSPR spectra of the ensemble and composite film have equal FWHM. Thus determined, the value of the B parameter is fed back into its defining equation, which now represents a trivial trigonometric equation in $\bar{\Phi}$. The solution of this equation is finally the sought average angle of the rods.

The relationship between $\bar{\Phi}$ and the parameter B mentioned above, is based on the following probabilistic approach. The intensity of the LSPR spectrum of a single AuNR was considered to be proportional to the probability of the compound event consisting of the following two independent sub-events: a) the occurrence that a typical rod has a given aspect ratio, assumed to be Gaussian distributed b) the spontaneous emission of photons by the gold atoms, which depends on the cosine-squared of the incidence angle between the polarized light and the rods.

Assuming electromagnetically non-interacting rods, the spectrum of their ensemble is then the superposition of the individual spectra, which is expressed by integrating with respect to the aspect ratio and the orientation angle of a rod – equation (8a).

As a first step in solving these equations, the dimensional categories of the rods are discretized and numerically simulated the LSPR spectra of the single rods in light polarized parallel to their long axis. The single rod spectra are then added together to obtain the longitudinal SPR of the ensemble by assuming values of the parameter B within the interval [0, 1], which is the maximal range of the function B – definition equation (6b).

The main steps taken to solve for the average orientation angle are summarized in the schematic of FIG. 5.10, below.

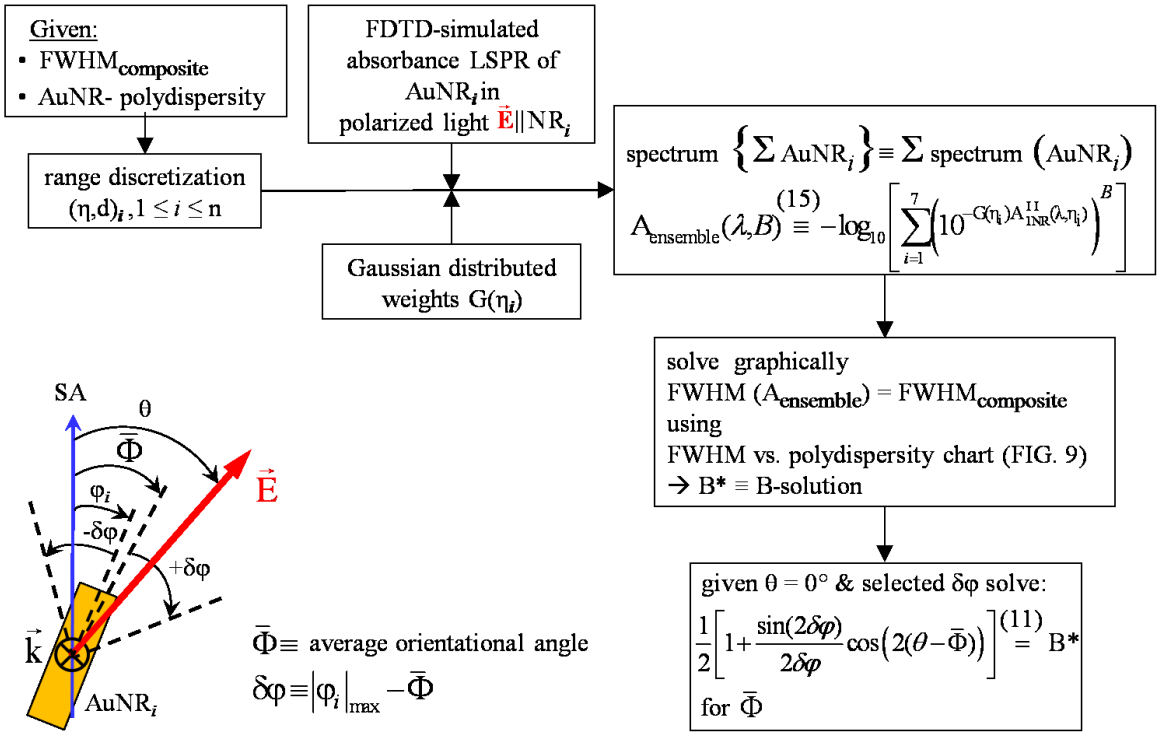

FIG. 5.10 Schematic of main steps in solving the discretized equations for the average orientation angle $\bar{\Phi}$ of the ensemble of AuNRs

Regarding solving for B by using the FWHM vs. polydispersity chart of FIG.5.9, the following sequence of steps is suggested: 1) simulation of the absorbance spectra of single rods 2) calculation of the spectrum of the ensemble for three polydispersities: the one given as input of the problem and two neighboring ones, one inferior and one superior; two would suffice but having three would allow for better accuracy. The values of parameter B can be taken from 0.5 up to 1.0, until a solution is obtained.

Knowing the exact polydispersity of the rods is essential since it affects: a) the range of the rod dimensions and the discretization into dimensional categories, b) the size and shape dependent dielectric function of the material and the absorbance spectra of the single rods, c) the solution B* and the average orientational angle.

Finally, the precision of the solution depends on the number of discrete dimensional categories of the rods and the accuracy of the numerical simulations.

6. Optical properties of gold nanostar-PDMS composite

Based on "Fabrication of a Gold Nanostar - Embedded Porous Poly(dimethylsiloxan) Platform for Sensing Applications", by N. Anand, S Venkatesh, P Putta, **S Stoenescu,** S. Badilescu, M. Packirisamy, V.-V.Truong published by Sensors & Transducers, 149, 2, 20, (2013) **My contribution:** FDTD simulations of absorbance of a gold nanostar

Chapter outline

6.1. Introduction.

6.2. Selection of the numerical method

6.3. The numerical solution and boundary conditions

6.4. Mesh convergence study

6.5. Results and discussion

- 6.5.1. The "sphere-only" model, labeled "S".
- 6.5.2. The sphere and one branch model "S1B"
- 6.5.3. Influence of branch length.
- 6.5.4. Influence of branch aperture
- 6.5.5. Influence of number (N) and orientation (angle φ) of the branches
- 6.5.6. The tunability of AuNSs optical response
- 6.5.7. Interaction of plasmons

6.1. Introduction.

A nanostar (NS) is an anisotropic NP that consists of a spheroidal core from which sharp-tipped branches extend out radially, as suggested by its name. Owing to its morphological complexity that can be appreciated from the sample shown in FIG.6.1, these NPs enjoy an improved tunability of their SPR peak wavelength and an enhanced sensing sensitivity. Specifically, the improved tunability of a NS resides in the possibility to excite SPR at a desired frequency by adjusting as many as four geometrical factors

characterizing a branch, as follows: length, aperture angle, number and orientation relative to other branches, as it will be shown below.

Together with the improved tunability, it is equally important to highlight that the localized SPR of NSs can be excited in the "water window" or the "tissue diagnostic window", which is the near-infrared (NIR) region between 700-1200 nm. This region is important because biological tissues absorb very little irradiation at these frequencies, such that accidental damage of the surrounding healthy tissue can be avoided while allowing for the useful illumination of NSs in its applications, for either in vivo imaging, destroying cancer cells or conveying of drugs for disease treatment in human health care [Huang, (2006), Alkilany (2012), Yuan, (2012), Zhang (2013)].

From the sensing standpoint, NSs have higher sensitivity than any of their component parts, considered individually [Hao, 2007]. This enhancement of sensitivity is due to the interaction between the electric fields induced in the constituent elements. Highly enhanced electric fields around the sharp tips of the branches provide the improved sensitivity of a NS to its dielectric surrounding, which can be used for biosensing applications. In this regard, ultrasensitive molecular detection at zepto-molar levels have been demonstrated [Lorenzo, 2009], where zepto-molar is 10^{-21} M and 1 M = 1 mole of matter per 1 liter of solution.

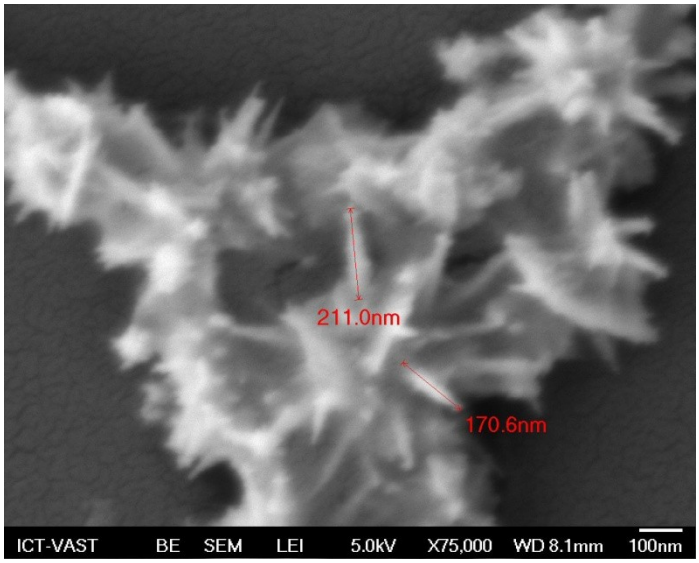

FIG. 6.1 Microscopic image of AuNS - PDMS composite. (Micrograph courtesy of Dr. Simona Badilescu, MIE Department, Concordia University)

The recently successful synthesis of NSs with adjustable geometry [Yuan, 2012] has opened up the possibility of synthesizing NSs that have desired optical properties, optimized to function at maximal efficiency in their applications. Based on these promising advances and on the advantageous properties of the AuNSs, a more in-depth study of their optical properties is of great theoretical interest and potential practical utility, which has motivated this work.

Therefore, assuming the synthesis feasibility of NS of arbitrary morphology and dimensions, the aim of this work was to analyze the functional role of the elements constituting a NS as well as the weight of their contribution in defining the overall optical properties of the structure. Besides the theoretical interest, the findings of this study may directly provide guidance in designing NSs with desired optical properties of optimum performance.

6.2. Selection of the numerical method

The simulation of optical properties of a NS was started by deconstructing the NP into solids of simpler shapes such as the sphere, truncated cones and spherical tips shown in FIG. 6.2 as suggested by previous works [Kumar 2008, Trigari 2011]. Using the geometric parameters listed in Table 1 to define the shape of these simpler solids, the absorbance spectra of their combinations were simulated by allowing these parameters to vary within their given ranges. Through this parameterized approach, the contribution of each component to the overall optical response could be investigated, which was assessed in terms of the spectral position and absorbance intensity of its main SPR peak. It was also aimed at finding out in what combination these components would better complement each other to produce by superposition an absorbance spectrum similar to the experimental one.

Since numerous NS models with accurate solutions were necessary in the shortest possible time, the size of the model relative to the magnitude of the incident light wavelength was a decisive factor that was taken into account. The maximum size of the NS was about 300 nm, comprised between the tips of two branches subtending 180° including the core. This size was of the same order of magnitude as the incident light wavelength, which raised the question of retardation of the EM wave propagation across the particle.

Retardation effects manifest themselves when the conduction electrons of a metallic NP do not oscillate in phase, due to non-negligible time differences that light takes to propagate from one part of the NP to another. These effects appear even when the largest dimension of a particle D_{max} is greater than about 20% of the electromagnetic

propagation wavelength λ_m in the surrounding medium [Myroshnychenko, 2008]. In this case, for PDMS as the medium with the dielectric function of $\varepsilon_m = 1.42$ a lightwave propagates with a wavelength of $\lambda_m = cT = nc_0T = \lambda_0 / \sqrt{\varepsilon_m} = 400 /1.19 = 335$ nm. Thus, the minimum diameter at which retardation appears is $D_{retard} \sim 20\%$ min $\lambda_m = 67$ nm. Taking as example even the mere spherical core with a diameter of D = 100 nm, a red shift and a broadening of the bandwidth of the SPR were expected, due to retardation. For this reason, using a fast but approximate numerical method based on the quasi-static assumption, such as DDA, could not have produced accurate results. Only a method based on solving the exact equations of electrodynamics had to be employed. As a result, the commercial software RSOFT was used, because it solves the full Maxwell's equations based on the finite difference time domain (FDTD) method.

The parameterized geometry of the elemental solids that make up a typical NS is defined as follows:

- sphere of diameter "D", which approximates the core
- branch approximated by a truncated right circular cone described by its
    - orientation angle "φ" with respect to the vertical axis Oz;
    - length "L" measured between its bases;
    - semi-aperture angle "α";
    - hemi-spherical tip of radius "r".

In a first stage of the simulation, all AuNSs models had coplanar branches, lying in the plane of the paper. Within this plane, the orientation of each branch was fully described by the angle "φ" with respect to the vertical axis Oz of the {x,y,z} reference system. Furthermore, the contribution of the constituent elements to the overall absorbance

spectrum of a AuNS model was analyzed based on their dimensions estimated from SEM micrographs of the AuNS samples.

However, in order to reduce the large number of the parameters and analyses required by the large polydispersity of the AuNSs, the diameter of the sphere simulating the NS core was held constant at a value of D = 100 nm. Therefore, a second stage of the analysis would be required to compensate for the missing variability of the optical response caused by holding the sphere diameter at a constant value. For the same reason, the radius of the semispherical tip of each branch was held constant at r = 3 nm. In this case, only the magnitude of the electric field enhancement is affected locally, in regions surrounding the tip of the branches, without affecting the spectral positions of the SPR modes. Table 6.1 and FIG. 6.2 summarize the definitions used and the values given to all the parameters used in describing a AuNS of average dimensions.

Table 6.1 Geometric parameters defining the morphology of a AuNS model

Parameter	Definition	Value(s)
D [nm]	Diameter of the core	100
N	Number of branches	1,2
L[nm]	Length of branch	100, 125, 150
r [nm]	Radius of hemispherical tip	3
α [°]	Half angle aperture of the branch tip	3, 10, 15
φ [°]	Branch orientation angle with respect to the Oz axis	0, 45, 180

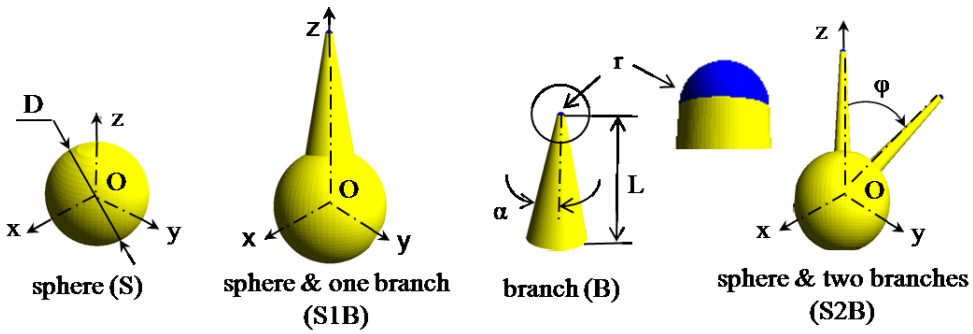

FIG. 6. 2 parameters used for the 3D model of an AuNS of average dimensions

6.3. The numerical solution and boundary conditions

The FDTD computational domain consisted of a parallelepipedic volume imagined to have been cut out of the embedding polymer matrix. Besides PDMS, the domain also contained the spherical core of the AuNS and the respective number of attached branches of the particular model under study. A lightwave of a certain polarization orientation was launched pointing towards the AuNS that was enclosed into a parallelepipedic "monitor" surface, which allowed for the monitoring of the power input and output through its surface. The difference between the input and output energy represented the energy absorbed by the AuNS as a function of EM radiation wavelength, or the absorbance spectrum. The computational domain was enclosed in a "perfectly matching layer" (PML) as absorbing boundary conditions, in order to prevent light waves and energy from being reflected back to the AuNS and interfere with the incident irradiation.

The regions of the domain occupied by PDMS and gold had optical properties defined by their corresponding dielectric functions. Due to the large size of the AuNS components compared to the mean free path (MFP) of the electrons, the dielectric function of the material was size independent and equal to the bulk dielectric function [Kreibig, 1995]. As such, the chromatic dispersion of bulk gold was described based on measured values [Johnson & Christy, 1972] of its real and imaginary parts (refractive index and coefficient of extinction, respectively). These values were provided as an external file to be read by the FDTD program to allow for interpolations at intermediary values.

For PDMS, an average refractive index value of 1.42 was considered, which takes into account the temperature and duration of its thermal treatment [Torres et. al., 2010].

6.4. Mesh convergence study

Since a non-uniform mesh was used to minimize the computational time and required memory, two regions of the computational domain D were relevant: the bulk region D_{bulk} or the region far away from the metal-to-polymer interface and the interface region $D_{interface}$ such that $D = D_{bulk} \cup D_{interface}$. Subsequently, the study was carried out in the following two steps:

1. by allowing the size of the bulk grid $\Delta_{\mathbf{B}}$ to vary, while keeping the size of the interface grid $\Delta_{\mathbf{IF}}$ in constant relationship with $\Delta_{\mathbf{B}}$, which allowed for the determination of $\Delta_{\mathbf{B}}$
2. by keeping $\Delta_{\mathbf{B}}$ constant at its value found at step 1 and allowing instead $\Delta_{\mathbf{I/F}}$ to vary.

Consequently, a uniform mesh of coarse size was generated for the bulk region and a very fine grid was generated to allow for an accurate solution of the field equations in the immediate vicinity of the metal-dielectric interfaces, where large gradients of the electromagnetic field existed. Especially the small geometrical details such as the sharp tips of the branches required an adequately fine grid. The transition between these two grids with contradictory requirements was made by using a graded grid.

In a first step, the convergence study for the bulk grid consisted of four iterations with grid sizes of Δ_B = 10, 7.5, 6 and 5 nm equal along the x, y and z coordinate axes, i.e. $\Delta_X = \Delta_Y = \Delta_Z = \Delta_B$. The edge grid had constant sizes and equal along the three axes,

i.e. $\delta_X = \delta_Y = \delta_Z = \Delta_B / 2$. The illumination of the NS had the electric field $\vec{E}$ polarized parallel to the Oz axis and the wave vector $\vec{k}$ was normal into the plane of the paper sheet. Since the spectral location of the SPR band of the spherical core was the most important result, it was chosen as the convergence criterion. Thus, when the change of the spectral location of the plasmon band was less than 1%, the solution was considered fully converged and the iteration process was stopped. The resulting spectra corresponding to these grids are shown in FIG. 6.3 (a).

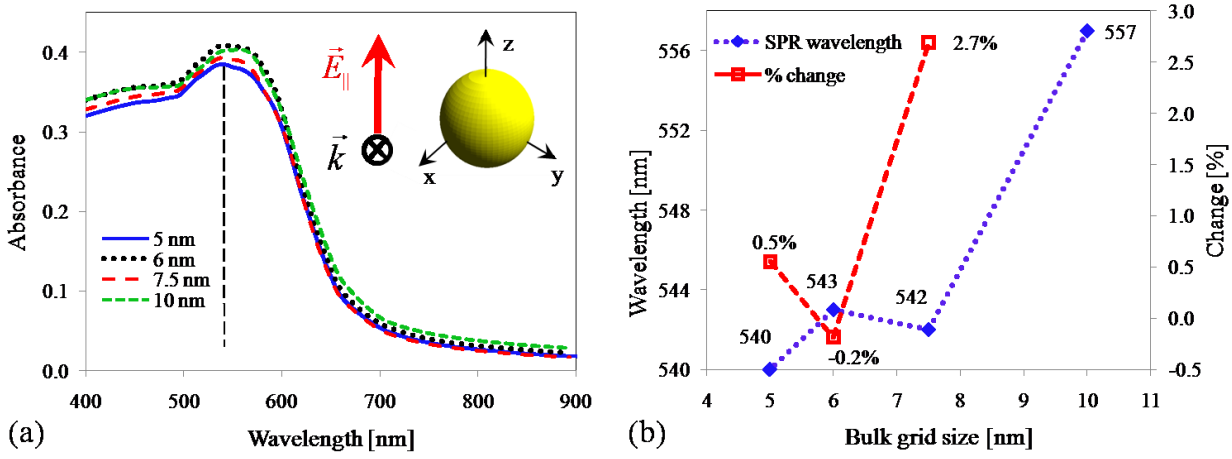

FIG. 6.3 Mesh convergence study for the bulk domain: (a) Absorbance spectra for grid sizes 10, 7.5, 6 and 5 nm. (b) Change of the SPR peak wavelength as a function of the grid size.

The convergence study for the metal-dielectric interface was carried out in a model that included one branch to allow for the smallest feature, i.e. the spherical cap of the branch, decide the size of the grid. As a consequence, the mesh required by the model was greatly enlarged. However, two sizes were tested for the edge grid: 1.25 and 1.0 nm while holding the bulk grid unchanged for two illumination cases: 1) electric field $\vec{E}_{\parallel}$ polarized parallel to the branch; 2) electric field $\vec{E}_{\perp}$ polarized normal to the branch.

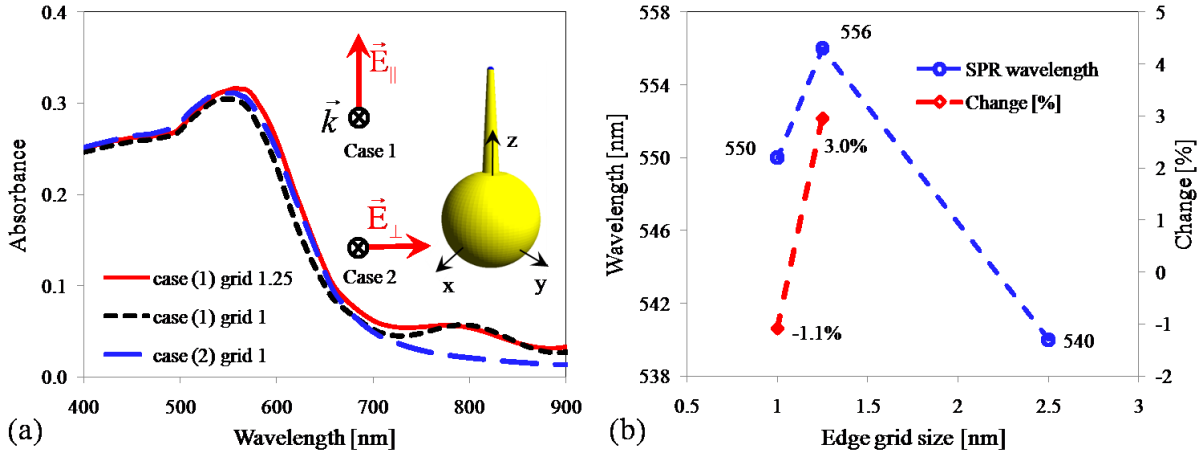

FIG. 6.4 Mesh convergence study for the metal-dielectric interface region. (a) Not normalized absorbance spectra for grid size of the edge 1.25 and 1.0 nm. (b) Change of the SPR peak wavelength as a function of the grid size.

As in the previous case, the criterion for convergence was the stabilization of the change of the plasmon band below 1%. However, reducing the edge grid from 1.25 to 1 nm greatly increased the model, such that any further increase would have led to a prohibitively large memory and computation time required. At this stage, the change of the SPR wavelength decreased to 1.1% only, as seen in FIG. 6.4 but the model was considered as converged, since it would not have been practical to further refine the mesh and increase the model.

To summarize, the model reached convergence for a uniform grid size of 5 nm for the bulk region and a size of 1 nm for the edge grid.

6.5. Results and discussion

6.5.1. The "sphere-only" model, labeled "S".

Due to its high order of symmetry, the model of the spherical core alone is isotropic and has a single dipolar SPR mode, irrespective of the polarization of the incident light wave. Therefore, the absorbance spectrum of the sphere is represented by the single black continuous curve in FIG. 6. 5, in response to both the s- and p-polarized lightwaves sketched in the inset (i). The FDTD-calculated plasmon band of the sphere is situated around 550 nm.

6.5.2. The "sphere and one branch" model, labeled "S1B"

6.5.2.1. Influence of branch length.

The attachment of a branch of half-aperture angle $\alpha = 3°$ to the sphere reduces its order of symmetry and renders it anisotropic. Therefore, its absorbance spectrum becomes dependent on the polarization of the incident light. When the polarization plane of the incident lightwave is parallel to the branch, as sketched in the inset (ii) of FIG. 6.5, a longitudinal SPR mode is excited in the branch. The peak wavelength of the plasmon is red-shifted with respect to the plasmon band of the sphere. Keeping the half-aperture angle of the branch at a constant value of $\alpha = 3°$ and varying only the length of the branch, the peak wavelength of the longitudinal SPR red-shifts with respect to the plasmon band of the sphere and strongly depends on the branch length. The absorbance curves for the branch lengths of 100, 125 and 150 nm have plasmon bands located at 794 nm, 870 nm and 960 nm, respectively, as shown in FIG. 6.5.

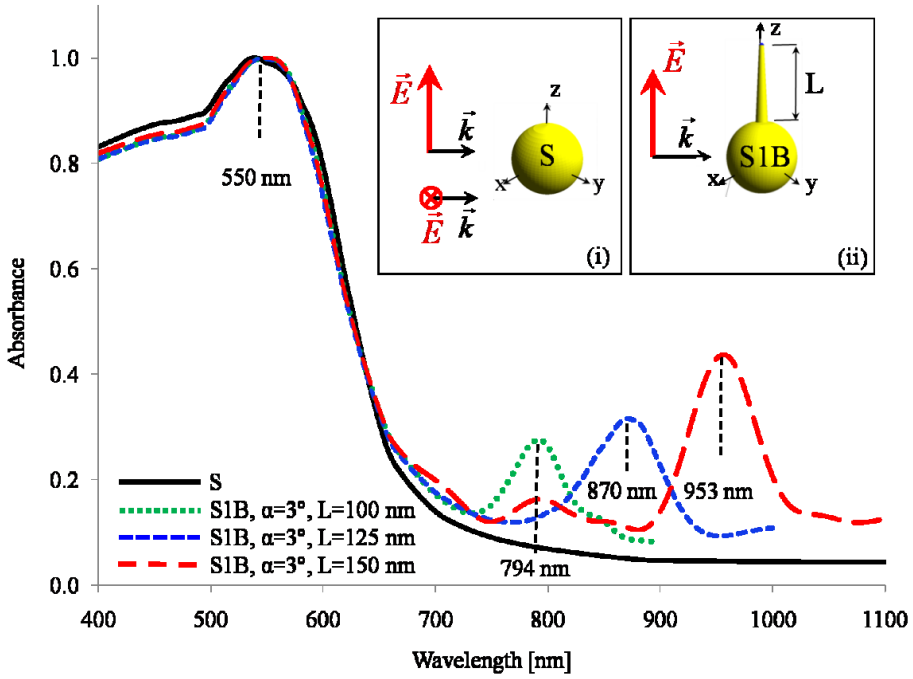

FIG. 6.5 Simulated absorbance spectra normalized with respect to the SPR wavelength of the spherical core.

The structure is illuminated by polarized light as shown in insets (i) and (ii). The spectra of the S1B models of branch lengths L=100, 125 and 150 nm are represented by the dotted/green, short-dashed/blue and long-dashed/red curves, respectively. All branches have the half-aperture angle of α = 3°. The spectrum of the spherical core is included as the continuous/black curve for reference.

6.5.2.2. Influence of branch aperture

Increasing the aperture of a branch drastically increases the intensity of the second plasmon, but only slightly red-shifts its peak wavelength, as shown in FIG. 6.6. For all simulations the nanostructure was illuminated by plane polarized light parallel to the axis of the branch.

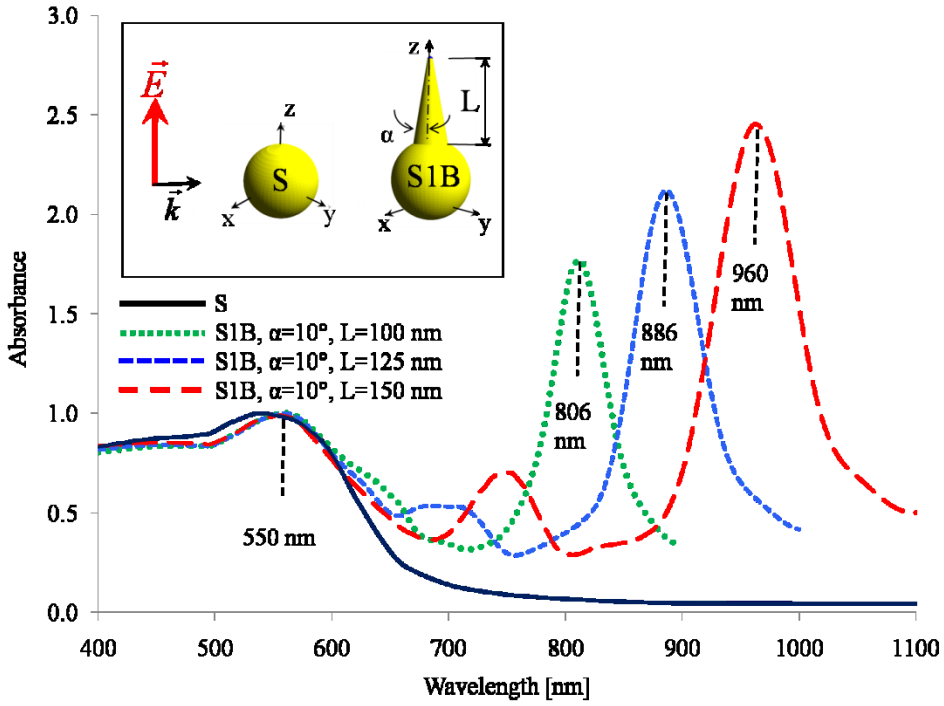

FIG. 6.6 Absorbance spectra of the S1B models, semi-aperture angle α=10° and branch lengths L = 100 dotted/green curve, L=125 short-dashed/blue curve and L=150 nm long-dashed/red curve, normalized with respect to the peak intensity of the S model. The spectrum of the spherical core is included as the curve S for reference.

The absorbance intensities of the secondary SPR modes are highly enhanced by increasing the semi-aperture angles, compared to the spectra of the S1B models with branches of semi-aperture angle α=3°, while their plasmon bands only red-shift slightly, as seen in FIG. 6.6.

Both spectral location and absorbance of the second SPR are highly dependent on the length and the aperture of the branches. This feature is useful for understanding the variable location and absorbance of the second SPR peak.

6.5.3. Influence of number (N) and orientation of the branches

Actual NSs have multiple branches of different lengths, apertures and orientations but including even three branches in a numerical model with adequately refined mesh

increases so much the size of the necessary memory and the length of computation time required for a fully converged solution that it is not possible to analyze the number of geometries and illumination cases in a reasonable period of time. Therefore, the effect of the number of branches on the optical response was assessed by increasing the number of branches up to a maximum number of two, while holding constant all other geometrical parameters: aperture, length and tip radius. A summary of the results obtained is the following and also shown in FIG. 6.7:

a) **N=0, model S (spherical core)** the continuous curve, shown for reference in FIG. 6.7
   - peak wavelength of the absorbance SPR at 550 nm;
   - the intensity of the absorbance SPR was used to normalize all the other spectra

b) **N = 1, model S1B** (core & one branch length L=100 nm of semi-aperture angle α=3°, parallel to the Oz-axis)
   - unchanged peak wavelength of the main SPR
   - appearance of the second SPR with the peak wavelength in the low NIR, at 787 nm.

c) **N = 2, model S2B,** angle between branches φ = 180° (the dashed curve)
   - 58% increase in absorbance intensity from 0.273 to 0.431.
   - spectral position of second SPR barely shifted 0.9% from 787 to 794 nm.

d) **N = 2, model S2B,** angle φ = 45° with respect to the Oz-axis

   illumination case – inset (i): the propagation vector "*k*" of the incident light wave is normal to the plane "π" (defined by the two branches) and the electric field $\vec{E}$ is polarized parallel to the Oz-axis).

- the second SPR, almost identically positioned,
- 11% increase in absorbance intensity, from 0.43 to 0.48. This enhancement of absorbance may be caused by the proximity of the two branches, which allowed the two individual plasmons on each branch to interact electromagnetically.

illumination case - inset (ii): the polarization plane of the illumination (defined by $\vec{E}$ & k) coincides with the plane π (the plane of the paper) and the electric vector $\vec{E}$ is parallel to Oz-axis, while keeping unchanged the geometry and arrangement of the branches

- the peak wavelengths of both the first and second SPR red-shift with 4.5% of the peak wavelength in the illumination case (i);
- the intensity of the first SPR peak remains unchanged and only the intensity of the second SPR peak grows by 18.5% relative to the second peak of S1B but less than the second peak of the S2B, illumination case (i).

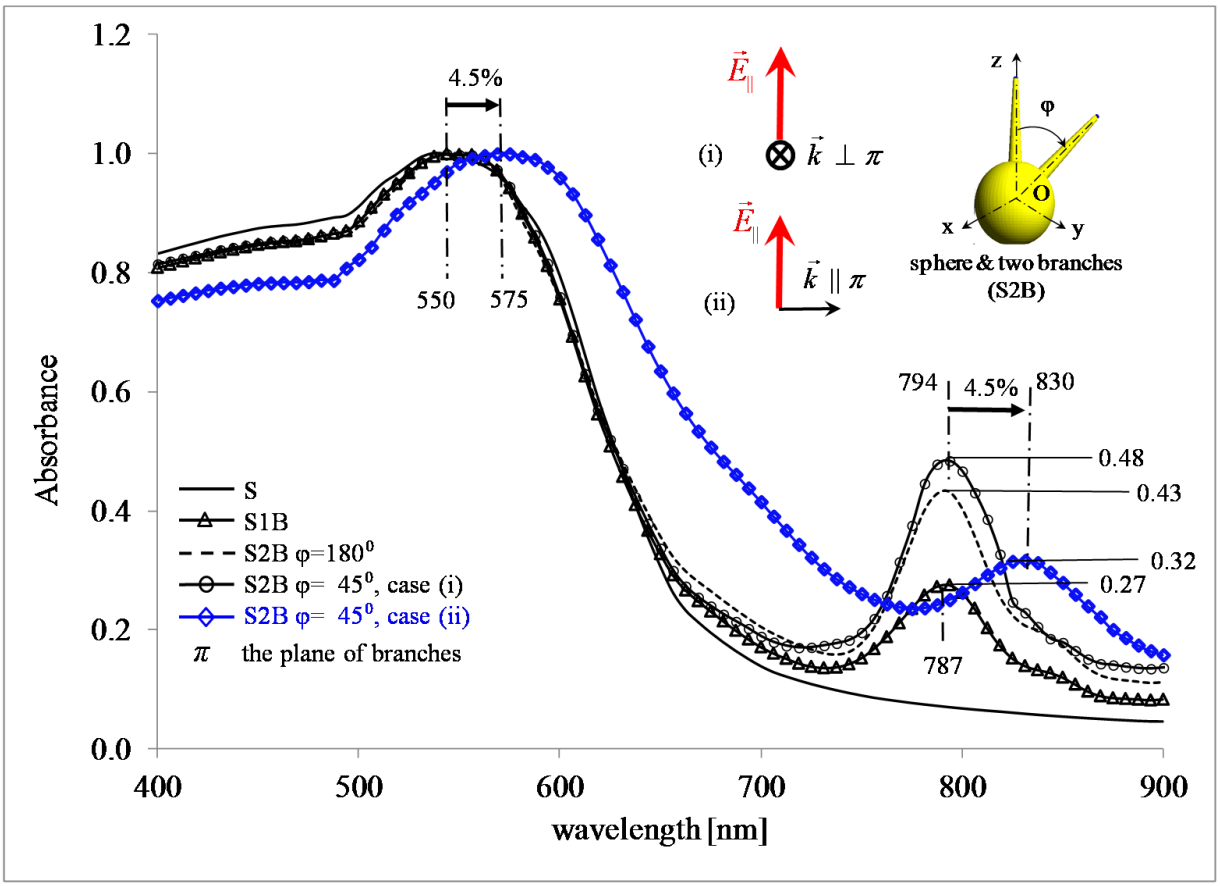

FIG. 6.7 Influence of the number of branches in two illumination cases, insets (i) and (ii).

The experimental absorbance spectrum of a large ensemble of AuNSs is given in FIG. 6.8 below for comparison. However, it must be specified that each individual AuNS of the ensemble is multi-branched, each branch possibly having its own unique length, aperture and tip radius. Therefore, the experimentally obtained spectrum is a superposition of spectra originated from AuNSs geometrically defined by parameters L, α, φ and r of all possible values.

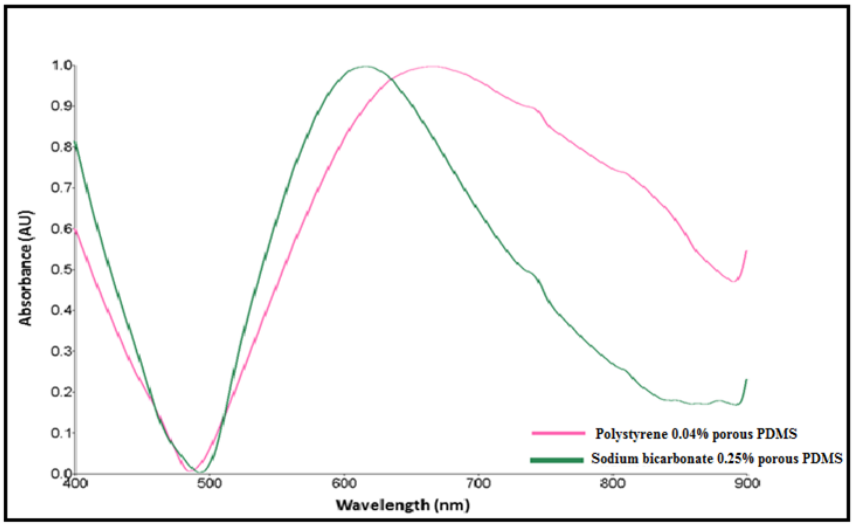

FIG. 6. 8 Two experimental spectra of AuNSs embedded in PDMS composite prepared with two porogens (Absorbance spectrum courtesy of Dr. Simona Badilescu, MIE Department Concordia University)

It is seen that spectra of branches of different geometries can complement each other to form by superposition an overall spectrum that is reasonably similar with the spectrum obtained experimentally. Indeed, by modifying the lengths of the branches, their plasmon bands can be blue shifted or red shifted, while by modifying the apertures, the intensity of their secondary SPR can be increased or decreased. Finally, by properly adjusting the geometry of the branches this shows how the AuNS structure can be optimized to achieve the spectral position and absorbance intensity required in a certain application. From this stand point, a NS is functionally superior to a NR, which is but one of the structural components of a NS.

6.5.4. The tunability of AuNSs optical response

As shown in FIG. 6.5 and 6.6, the spectral position of the second SPR mode (induced in the branch) strongly depends on both the length and aperture of a branch. Since the absorbance of the second SPR mode can be of much higher intensity than the

first SPR mode (of the core), the overall response of the AuNS is strongly dependent on the second SPR. In order to adjust the excitation wavelength of the overall optical response of the AuNSs within a desired region of the optical spectrum, the most effective means of fine-tuning may be desired. For this reason it is therefore necessary to know the rate of shift of the second SPR with respect to each factor that causes the shift.

This is especially important if the synthesis of AuNSs can be carried out in a controlled fashion, in which case the geometry of AuNSs have to be designed for optimal optical properties before synthesis.

Panels a) and b) of FIG. 6.9 below show the change in spectral position of the second SPR with respect to the first SPR, when the length and aperture of the branch are varied. It is noticed that the wavelength of the second SPR is strongly red-shifted almost linearly with the branch length, for half-aperture angles held constant at 3° and 10°, as seen in panel (a).

In the same time, a variable aperture angle of the branch below 10^0 red shifts the second SPR with 46%, or equally much as shown in the panel (b). For aperture angles between 10^0 and 15^0, the shift effect decreases with up to 10%.

Therefore, the SPR spectral location of the S1B model can be fine-tuned more effectively by adjusting the length of the branch than by adjusting its aperture. This conclusion can be generalized to a multi-branch AuNS, since its spectrum is the average of the spectra of its component branches joined to the core. Of course, a missing factor in this simpler analysis is the fact that the EM coupling of all the branches was not possible to take into account.

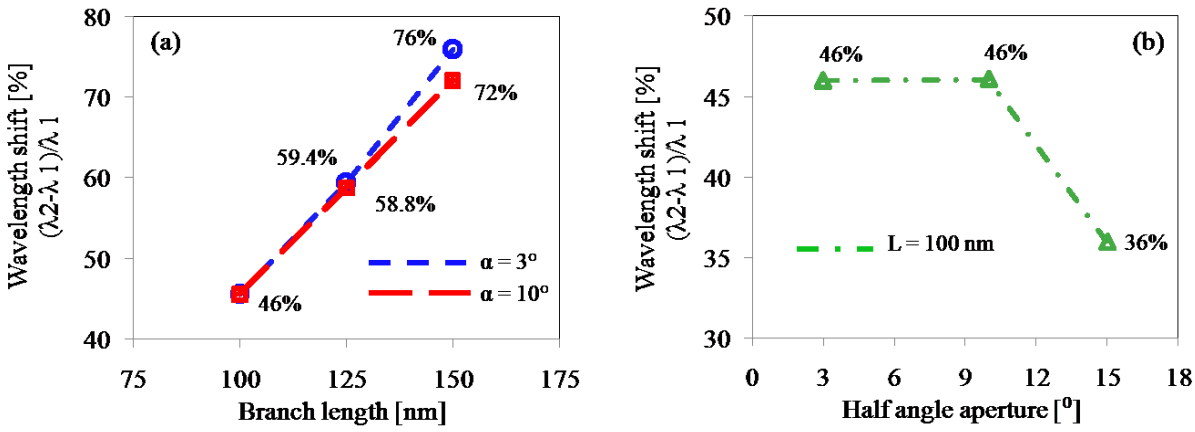

FIG. 6.9 Shift of peak wavelength of the second SPR mode (of the branch) with respect to the first SPR mode (of the sphere) for two cases: a) variable branch length at constant aperture (α = 3° and α = 10°) and b) variable branch aperture at constant length (L = 100 nm)

6.5.5. Interaction of plasmons

Comparing the first two SPR modes of the S1B model of FIG. 6.7 with the corresponding SPR modes of the separate core and branch models, a clear shift of the spectral positions is noticed, as shown in the panels (a) to (c) of each of the FIG. 6.11 to FIG. 6.13. The left and right hand side panels (a) and (c) of each of these figures present the absorbance spectra of the separate models of the core (S) and of the branch (B), while in the middle panels (b) the absorbance spectra of the core-and-branch union (S1B) models are shown, all resulting from illumination with plane polarized light with the electric field $\vec{E}$ parallel to the branch axis Oz and the propagation vector $\vec{k}$ normal to the plane of the paper.

The shift of the plasmon bands is due to the EM interaction of the plasmons generated in each component part of a AuNS structure. The interaction has been interpreted in a theory that is analog to the electron hybridization of molecular orbital

theory [Hao, 2007; Prodan, 2003; Brandl, 2007]. Similar to bonding of dissimilar atoms to form the stable molecule of a new compound, plasmons of different structural parts of a nanostructure interact electromagnetically with a strength that depends on the distance between the parts and on the surrounding dielectric medium. The plasmonic interaction results in two possible coupling modes:

1) a symmetric or bonding plasmon of low energy and

2) an antisymmetric or antibonding plasmon of high energy.

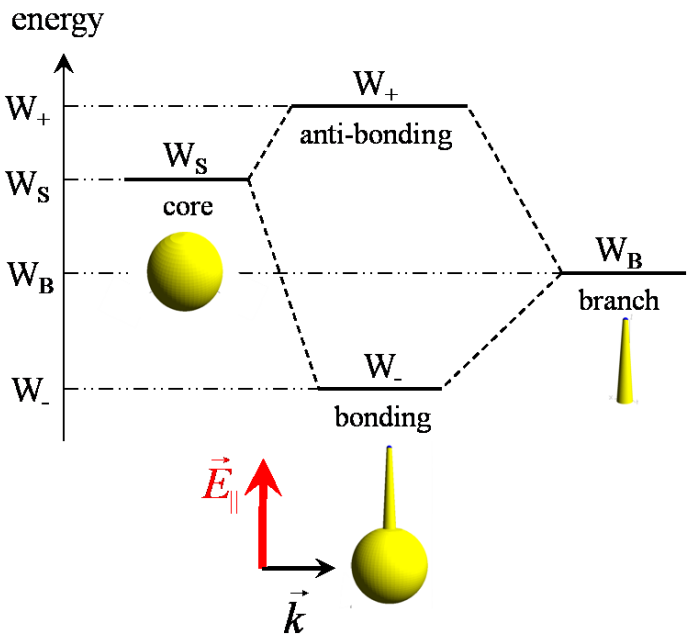

FIG. 6.10 The energy level diagram of the hybridization theory of plasmons.

The hybridization theory of plasmons is analog to the orbital molecular theory. Elementary plasmons induced in the core and branches of a NS hybridize with the formation of two possible plasmons: bonding of low energy W_- and antibonding of higher energy W_+ which correspond to electron sharing between bonding atoms.

Applying this theory to the AuNSs of FIG. 6.11, it is seen that the separated branch of semi-aperture angle of 3° and 100 nm length has its SPR band positioned at 1.75 eV. In the branch & sphere model S1B, the plasmon of the branch interacts with the plasmon of the core of 2.31 eV and they strongly couple forming a binding plasmon of lower energy of 1.57 eV.

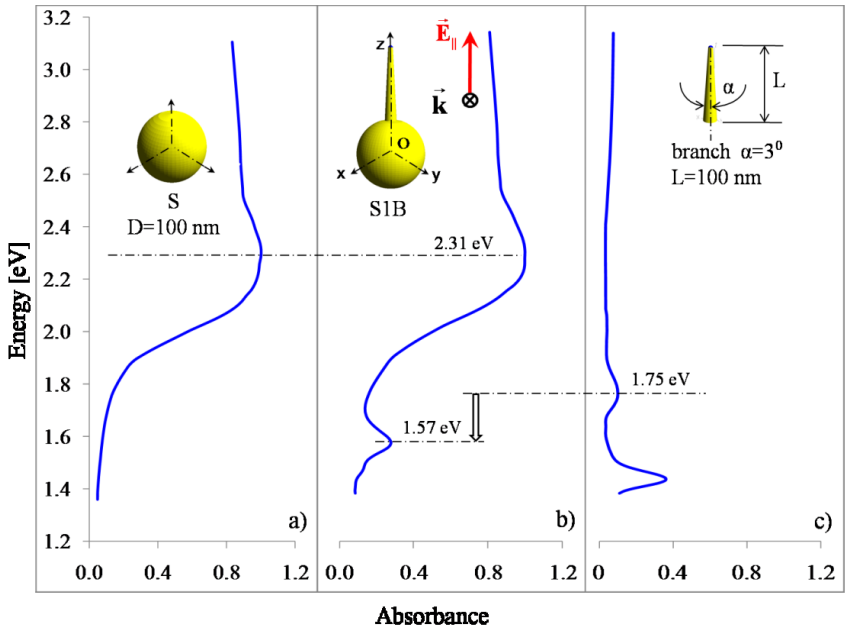

FIG. 6.11 Energy diagram of plasmon interaction in AuNS, model S1B where the branch parameter values are α=3° and L=100 nm.

In FIG.6.11, the core and branch are detached from each other and plasmons are induced separately in each one, as shown in panel (a) and (c) at specific wavelengths, corresponding to their fundamental excitation. However, if the branch is attached to the sphere and the joint system is excited, the excitation wavelengths will be different for each part, as seen in panel (b). this is because the two plasmons generated in each part is affected by the EM field irradiated by the other plasmon.

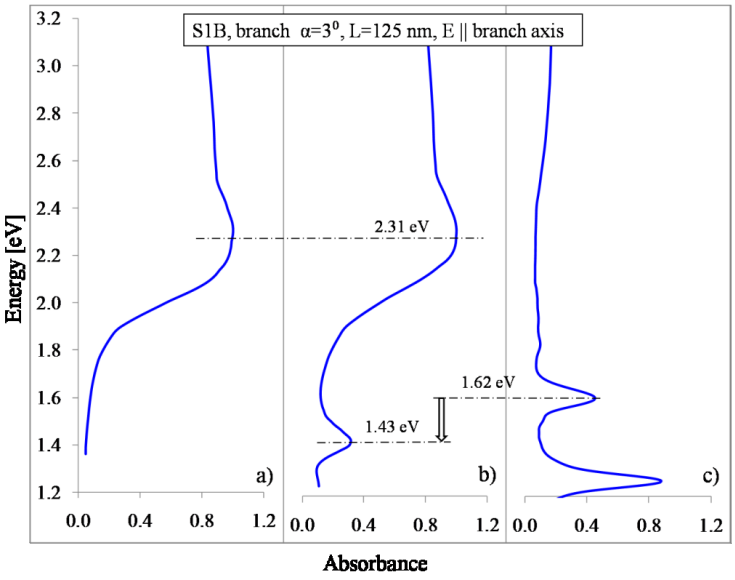

FIG. 6.12 Energy diagram of plasmon interaction in AuNS. Plasmons are induced separately in the spherical core (a) and in the branch of α=3° and L=125 nm (c) at specific wavelengths that change when the plasmons are induced in the same parts but are allowed to interact within the NS structure (c).

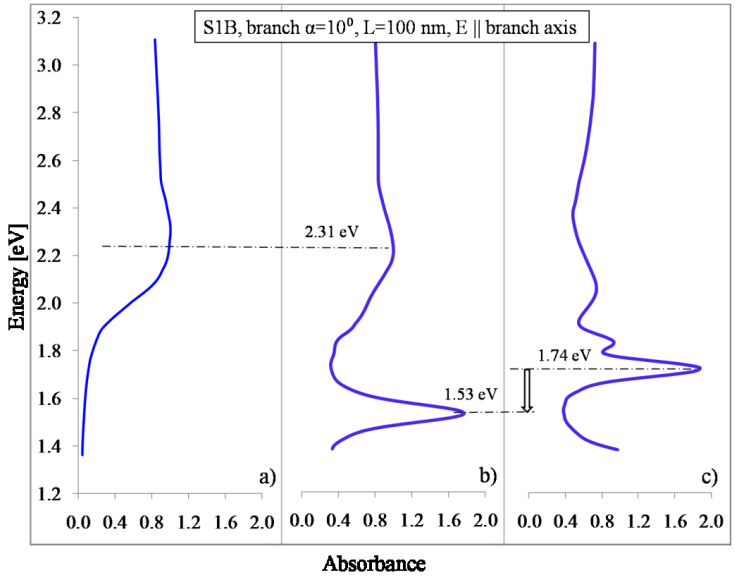

FIG. 6.13 Energy diagram of plasmon interaction in AuNR. Plasmons are induced separately in the spherical core (a) and in the branch of α=10° and L=100 nm (c) at specific wavelengths that

change when the plasmons are induced in the same parts but are allowed to interact within the NS structure (c).

In all the above cases, the plasmons induced in the spherical cores are much less sensitive to the plasmons of the branches and its spectral position changes a negligible amount. The plasmons induced in the branches are more sensitive to the surrounding EM fields and their spectral position always changes much more significantly toward lower energies.

7. Conclusions and suggestions for future work

Chapter outline

7.1. Summary
7.2. Conclusions
7.3. Suggestions for further research
7.4. Contributions

7.1. Summary

Chapter 1 introduced the topic of this research, as a particular aspect of light-matter interaction in which the intensity of light is controlled to achieve a certain useful goal. This goal was specified by using two application examples**,** to suggest the practical importance of and present the motivation that has driven this research.

In the first application example, incident light through its EM field was modulated in magnitude and direction by being allowed to pass through a stretched AuNR-PVA composite film. As a result, the transmitted light had the electric field component parallel to the transmission axis (TA) of the film, or, perpendicular to the stretch direction of the film, while the component orthogonal to TA was cut off by the EM field induced in the nanorods embedded in the film. The intensity of the transmitted EM radiation was proportional to the cosine squared of the relative orientation angle θ between the vibration plane of the incident electric field and the plane of the film. It was expected that a high enough concentration of the rods density would allow for coupling of the EM fields induced in neighboring rods and leading to possibly nonlinear effects, if the intensity of the incident light is high enough.

In the second application example, nanostars of a certain morphology of its branches could be designed such that the peak excitation wavelength could be spectrally positioned most conveniently, from the standpoint of the biological tissue studied or of the laser source available

Chapter 2 prepared the theoretical background necessary to present the work of this thesis, presented in the rest of the chapters. Main definitions were stated and the relevant physical phenomena were presented, along with the physical and mathematical models used to study them.

Chapter 3 presented the method used for achieving highly aligned AuNRs embedded in polymer film by the film stretching method. The purpose was to enable the simultaneous and maximum excitation of the longitudinal SPR throughout the ensemble of rods. The good alignment induced by stretch ratios as high as seven, was succeeded by using the highest molecular weight PVA and mixing a small amount of plasticizer in the polymer solution prior to the dispersion of the rods in the polymer solution. Finally the composite film was stretched by using a stretch device especially designed to avoid the fracture of the composite film.

Chapter 4 presented the optical characterization of the resulting composite film. A first statistical quantification of the alignment of the embedded rods showed an orientational order parameter of 0.92 or only 8% off the perfect alignment and an average orientational angle of 3.5°, the angle origin being 0 (zero), which was the direction of stretching. Optical characterization followed with spectroscopic measurements using polarized light and computational simulations that successfully matched the experimental ones. It was thus proved that the stretching process had induced almost perfect dichroic

optical properties in the composite film. This demonstrated the important fact that the nanoscopic anisotropy of each individual AuNR can and had been expanded to the macroscopic scale of the composite film and of all potential applications based on this type of film.

Chapter 5 looked back at the statistical quantification method based on the experience accumulated during the measurements, to note that the statistical method based on SEM micrographs requires destructive testing and the results are time consuming and only very approximate. Instead, a novel non-destructive quantification method is presented and suggested as a method to replace the statistical one. This new method is based on a probabilistic approach, computational simulations and spectroscopic measurements and was applied to the same stretched composite film for the validation of the results.

The commonly used method based on statistical estimations is considered as the reference method, because its uncertainty resides in the degree of accuracy of its SEM measurements. The average orientation angle of the rods obtained by the new and untested method is shown to have a difference of 8.6% compared to the result of the reference method. Taking into account that the reference method is itself an estimation, the accuracy of the proposed method may actually be better and inspires confidence in the principle and implementation of the new method. In addition, the new method had been explained by applying it to AuNRs for the sake of concreteness, but the method can be applied to any dichroic particles of well defined geometry and polydispersity.

Chapter 6 characterizes optically a AuNS by computational simulations of absorbance spectra. The numerical model was built up by decomposing a AuNS into

parameterized structural elements to allow for the systematic study of its optical properties. As a result, this structure was shown to have highly tunable fundamental SPR, which can be achieved by adjusting the geometry, orientation and number of their branches. The most effective way of tuning the resonant excitation of a AuNS is determined. This study also reveals the absorptive contribution of each element, which may be useful in designing a NS of desired performance if the synthesis process could be controlled at the level of detail required. Using numerical simulations of absorbance spectra of AuNSs in plane polarized light, it was shown that the geometric parameters that define the branches are important factors for tuning the absorbance peak of the overall nanostructure.

7.2. Conclusions

1. It is possible to quantify the alignment of the nanorods embedded in polymer films by using the non-destructive method proposed in this thesis.
2. The alignment of the nanorods was achieved after an improvement of the film matrix at an average angle of 3.5° according to a statistical quantification and at an average angle of 3.8° according to the non-destructive quantification method.
3. The alignment was also quantified by an orientational order parameter of 0.92.
4. The modeling proposed in this thesis is able to accurately capture the optical anisotropic nature of the nanostructures. The simulation results are in good agreement with the spectroscopic measurements.
5. The spectral position of the peak wavelength and the intensity of absorbance SPR of the AuNS structure can be adjusted by varying the length, aperture angle and number

of its branches. The most influential factor is the length, followed by aperture and finally their number.

7.2. Suggestions for further research

Aligning anisotropic NPs such the AuNRs embedded in a polymer film was shown to be a successful method. This was demonstrated by the slight deviation of the optical properties of the stretched composite film from the dichroic properties of the idealized system of identical, perfectly aligned and electromagnetically non-interacting AuNRs simulated by FDTD computations. As well, the statistically significant sample (SSS) collected from the SEM micrographs showed only a very small number of misaligned or electromagnetically coupled rods, or rods reshaped to spheres. And the SSS also showed undoubtedly that the rods were dispersed non-uniformly, which allowed for the small number of coupled rods. Therefore, the uniformity of the rod distribution is desired to be improved.

The following steps for improving the method can be taken in future research:

a) It was noticed during the preparation of the polymer solution and dispersion of the AuNRs that the degree of mixing of the rods by sonication, however energetic and prolonged in time, cannot insure a perfect uniform dispersion. It is suggested that means other than pure mechanical mixing should be used. For example, chemically binding macromolecules may be allowed to bind to the surface of the rods, to function as mechanical spacing elements that connect the rods, maintaining a relatively constant separating distance and preventing them from coming to close to

each other. There is a high likelihood that a uniform distribution of the rods can be achieved only chemically.

b) After the uniformity of the rod distribution is succeeded, it will be important to study the influence of the rod concentration on the electric field enhancement, especially by using ultra fast laser pulses to generate nonlinear effects as it was shown in the schematic diagram of FIG.1.3 of the introduction. Due to the risk of rod reshaping as heat is transferred to the rods during laser irradiation, the intensity and duration of the laser pulses needs to be carefully tested. The temperature threshold triggering the atomic rearrangement of the rods that was determined in Chapter 4 is a good starting point to estimate the amount of heat a rod can absorb without experiencing alteration of the optical properties.

c) Quantifying the alignment of the rods by the proposed non-destructive method requires an accurate knowledge of the polydispersity of the rods, as shown in Chapter 5. It is therefore recommended that TEM analyses be carried out prior to mixing of the rods in the polymer solution.

d) It is also desired that the calculation procedure of the non-destructive method can be improved by increasing its accuracy and speeding up several of its steps. For example, it is suggested writing a script for the FDTD software (in this case RSoft) such that the required absorbance simulations of the dimensionally representative rods can be run in batch mode. This much faster simulation of absorbance spectra would allow increasing the number of steps used for the discretization of the dimensional range between the minimum and maximum aspect ratio.

e) The chart of FIG.5.9 (chapter 5) shows curves of the FWHM of the composite film vs. the polydispersity of the rods for constant B values as being very closely approximated by second order degree polynomials. This would be interesting to be proved analytically, if possible.

7.3. Contributions

As solutions to the difficulties encountered during my attempt to accomplish the objectives stated in this thesis, this work has:

1. Developed a novel method to non-destructively quantify the alignment of nanorods embedded in polymer film, by deriving an equation based on a probabilistic approach combined with numerical simulations of absorbance spectra, mathematical modeling and spectrometric measurement of the composite film. The results of this method agreed with the results of the statistical method and were also confirmed by the demonstrated dichroic properties of the composite film.

2. Innovated on the standard preparation of a composite film by:

a) determining a maximum allowable heating temperature and duration during the stretching process of the AuNR-PVA composite films to prevent thermal reshaping and consequent alteration of optical properties of the AuNRs;

b) analyzing the physics of polymer stretching and as a result selected a polymer of the highest molecular weight as the matrix of the composite film to allow for higher stretch ratios of the composite films;

c) mixing a small amount of glycerin as plasticizer in the composition the polymer matrix to compensate for the higher glass transition temperature required by the high molecular weight polymer;

d) designing a device for stretching polymer films with reduced risk of fraction of the polymer.

Refereed Journal & Proceedings papers

1. **S. Stoenescu,** V.V. Truong, M. Packirisamy, "*Non-Destructive Quantification of Alignment of Nanorods Embedded In Uniaxially Stretched Polymer Films"* submitted to: Journal of Applied Physics, November 22, 2013, currently under review

2. **S. Stoenescu,** V.V. Truong, M. Packirisamy, "*Improved Alignment of Gold Nanorods Embedded in Polymer Films*", Int. J. Theoretical & Applied Nanotechnology, in press, December 2013

3. **S. Stoenescu,** V.V. Truong, M. Packirisamy, "*Dichroic Optical Properties of Uniaxially Oriented Gold Nanorods in Polymer Films",* published online by Plasmonics, Oct. 2013, DOI 10.1007/s11468-013-9623-x

4. N. Anand, S Venkatesh, P Putta, **S. Stoenescu**, S. Badilescu, M. Packirisamy, V.-V.Truong "*Fabrication of a Gold Nanostar - Embedded Porous Poly(dimethylsiloxan) Platform for Sensing Applications",* published by Sensors & Transducers, 149, 2, 20, (2013) My contribution: FDTD simulations of absorbance of nanostar

5. **S. Stoenescu**, S. Badilescu, V.V. Truong, M. Packirisamy, "Enhanced Anisotropy of Gold Nanorod-Polymer Composite Films for Optical Applications", Proc. SPIE 8412, Photonics North 2012, 84121T (October 23, 2012); doi:10.1117/12.2001172

6. **S. Stoenescu,** S. Badilescu, V.V. Truong, M. Packirisamy, "Synthesis and Optical Properties of Anisotropic Gold Nanoparticles", Proc. SPIE 7386, Photonics North 2009, 73862V (August 04, 2009); doi:10.1117/12.839605

Conference presentations

1. **S. Stoenescu,** V.V. Truong, M. Packirisamy, "*Improved Alignment of Gold Nanorods Embedded in Polymer Films*", Int. Conf. on Nanotechnology: Fundamentals & Applications, presentation, Toronto, August 12-14, (2013)

2. **S. Stoenescu,** S. Badilescu, V.V. Truong, M. Packirisamy, "Enhanced Anisotropy of Gold Nanorod-Polymer Composite Films for Optical Applications", Photonics North, Montreal, poster, June 6-8, (2012)

3. **S. Stoenescu,** S. Badilescu, V.V. Truong, M. Packirisamy, "Aligned Gold Nanorods in Polymer Films", Nano-Quebec, Montreal, poster, March 20-21, (2012)

4. **S. Stoenescu,** S. Badilescu, V.V. Truong, M. Packirisamy, "Synthesis and Optical Properties of Anisotropic Gold Nanoparticles", Photonics North, presentation, City, May 24-27, (2009) Quebec

Appendix A: The size and shape adapted dielectric functions

For the wavelengths of interest (400-900 nm) and at room temperature the mean free path (MFP) of the free conduction electrons of bulk gold is within the range $10 \leq \text{MFP} \leq 42$ nm (Kreibig et al., 1995; Zhukov et al., 2006) and therefore larger than the smallest dimension of the rods (diameter d=10 nm). This determines that the dielectric function of gold depends on the size and shape of the particles (Genzel et al., 1975; Noguez 2007), which was treated classically by considering a reduced effective MFP, denoted by L_{eff}, of the free conduction electrons, as follows (Coronado et al. 2003; Liu et al., 2004):

$$Leff(\eta, d) = \frac{2\eta}{1+2\eta} d \qquad (A1)$$

where η = L/d is the aspect ratio of a rod. The damping constant affected by the reduced MFP and scattering from the particle surface (Genzel et al. 1975), is written as:

$$\gamma_{eff} = \gamma(L_{eff}) = \gamma_0 + \alpha v_F / L_{eff} \qquad (A2)$$

where γ_0 = 1.075 10^{14} s^{-1} is the damping constant of the bulk material (Johnson & Christy, 1972), v_F = 1.39 10^6 m/s is the Fermi velocity of electrons and α=0.33 is the electron-surface scattering parameter, a dimensionless constant (Sönnichsen et al., 2002; Berciaud et al.2005; Novo et al., 2006) . The following dielectric function is obtained:

$$\varepsilon(\omega, L_{eff}) = \varepsilon_{bulk}(\omega) + \frac{\omega_P^2}{\omega^2 + i\gamma_0\omega} - \frac{\omega_P^2}{\omega^2 + i\gamma_{eff}\omega} \qquad (A3)$$

in which ω_P^2 is the plasma frequency of the electron gas [33]. The deviations of the refractive index and extinction coefficient from the bulk values due to size and shape

effects are shown in FIG.A1, panels (a) and (b), respectively. The multiple charts shown in the insets correspond to the seven dimensional categories η of the discretized model.

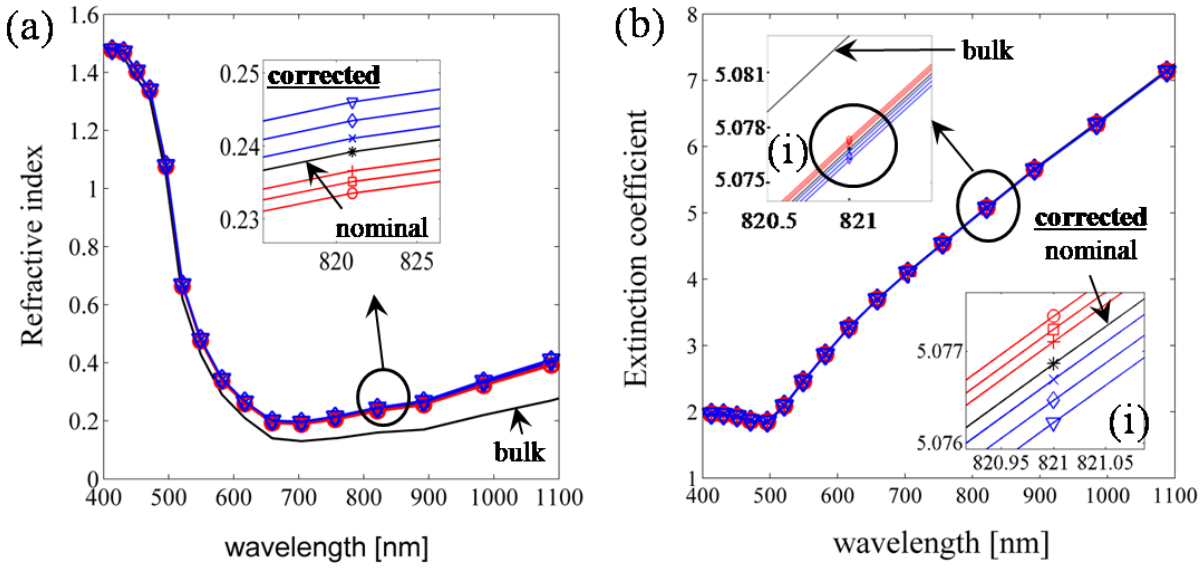

FIG. 5.A.1 (a) Bulk and corrected refractive index; (b) Extinction coefficient of gold.

The dimensionless correction factor A = 0.33 takes into account both particle size and shape effects. Each inset of the panels zooms in at a point of the curves to highlight the difference between the dielectric functions of the seven dimensional categories $(\eta, r)_k$. In each inset of the panels, the curves marked by an asterisk * represent the coefficients of the nominal rod, in the middle of the other six dimensional categories, the red and blue curves, which are marked with the symbols shown in Table 5.A1:

Table 5.A.1 Line markers used in FIG. 5.A1 for dimensional categories "η"

Aspect ratio η	3.11	3.34	3.57	3.80	4.03	4.26	4.49
Marker	red "○"	red "□"	red "+"	black "✱"	blue "×"	blue "◊"	blue "▽"

Appendix B: The cosine-squared law

A polarized light beam in interaction with the AuNRs of a composite film may induce a transition from a lower energy W_1 to a higher energy W_2 state of the gold atoms that make up the rods. The excited atoms may then relax by spontaneously emitting photons with a probability P_{21} that - according to Fermi's golden rule - is proportional to the square of the matrix element M_{21} that describes the light-matter interaction, that is: $P_{21} \propto |M_{21}|^2$. The interaction between light and atoms takes place between the electric field $\vec{E}$ of the incident light and the electric dipole $\vec{p}$ of an atom, which in the case of visible EM-radiation is given by $\vec{p} = -e\vec{r}$. Finally, the matrix element M_{21} can be expressed as (Thulstrup & Thulstrup, 2005):

$$M_{21} = -\int \Psi_1^* \left(\vec{p} \bullet \vec{E}_0\right) \Psi_2 d^3\vec{r} = -\vec{\mu}_{21} \bullet \vec{E}_0 \propto \cos(\theta - \varphi) \qquad \text{(B.1)}$$

where Ψ_1 and Ψ_2 are the wave functions of the relaxed and excited state, respectively, $\vec{\mu}_{21} = -e \int \Psi_2 \vec{r} \Psi_1 a\ \vec{r}$ is the electric dipole moment of the transition 2→1 and $\vec{E}_0$ is the incident electric field. Since the wavelength of the electric field in the visible range is much larger than the size of the gold atoms, the variation of the electric field is negligibly small over the space occupied by an atom. Therefore, $\vec{E}_0$ was approximated as constant and taken outside the integral in (3). It results that the excited atoms relax by emitting photons with a probability P_{21} proportional to the cosine-squared:

$$P_{21} \propto |M_{21}|^2 \propto \cos^2(\theta) \qquad (B.2)$$

The emitted photons are further captured by the detector of the spectrophotometer such that the recorded absorbance spectrum exhibits a cosine-squared dependence on the polarization angle θ, as well.

References

Ahmed W., Kooij ES, van Silfhout A, Poelsema B., Quantitative Analysis of Gold Nanorod Alignment after Electric Field-Assisted Deposition, (2009), Nano Letters, Vol. 9, No. 11, 3786-3794

Alkilany, A. M., Thompson, L.B., Boulos, S.P., Sisco, P. N., Murphy, C. J., "Gold nanorods: Their potential for photothermal therapeutics and drug delivery, tempered by the complexity of their biological interactions", Advanced Drug Delivery Reviews, 64, 190–199, (2012)

Anker J. N., Hall W.P., Lyandres O, Shah N.C. , Zhao J., and Van Duyke R.P., "Biosensing with plasmonic nanosensors", Nature Materials, Vol 7 , June 2008

Ashcroft N. W., Mermin N. D, Solid State Physics, (1976), (Philadelphia, Pennsylvania: Saunders College)

Berciaud S., Cognet L., Tamarat P. and Lounis B., "Observation of Intrinsic Size Effects in the Optical Response of Individual Gold Nanoparticles", Nano Letters, Vol. 5, No. 3, 515-518, (2005)

Bérenger J.-P., "A perfectly matched layer for the absorption of electromagnetic waves, Journal of Computational Physics", 114 (1994) 185–200.

Bohren C. F., Huffman D.R., (1983). Absorption and Scattering of Light by Small Particles, John Wiley & Sons, Inc.

Boyd R., "Non-linear Optics", Academic Press, 2008

Brandl D. W. and Nordlander P.," Plasmon modes of curvilinear metallic core/shell particles", The Journal of Chemical Physics 126, 144708 (2007)

Brioude A., Jiang X. C., and Pileni M. P., "Optical Properties of Gold Nanorods: DDA Simulations Supported by Experiments", J. Phys. Chem. B 109, 13138 (2005).

Callister W.d. and Rethwisch D. G., (2010), Materials Science and Engineering - An Introduction, John Wiley & Sons, Inc.

Coronado E.A. and Schatz G.C., "Surface plasmon broadening for arbitrary shape nanoparticles: A geometrical probability approach", J. Chem. Phys. Vol. 119, Nr 7, (2003)

Devore J.L., (2012), Probability and Statistics for Engineering and the Sciences, Brooks/Cole

Fei Pei F., Song Wu, Gang Wang, Ming Xu, Song-You Wang and Liang-Yao Chen, "Electronic and Optical Properties of Noble Metal Oxides M2O, (M = Cu, Ag and Au): First-principles Study", J. Korean Phys. Soc., Vol. 55, No. 3, September 2009, pp. 1243-1249

Finch C. A., (1973), Polyvinyl alcohol, properties and applications, Wiley, New York

Genzel L., Martin T.P., Kreibig U., "Dielectric Function and Plasma Resonances of Small Metal Particles", Z. Physik B 21, 339- 346, (1975)

Guo C., Yin S., Yu H., Liu S., Dong Q., Goto T., Zhang Z., Li Y., and Sato T., "Photothermal ablation cancer therapy using homogeneous Cs_xWO_3 nanorods with broad near-infrared absorption", Nanoscale, 5, 6469, (2013)

Greffet J.J., Ch.4 in "Plasmonics. From Basics to Advanced Topics", Edited by Enoch, S; Bonod, N., Springer, 2012

Hagan D. J., Handbook of Optics, The McGraw-Hill Companies, Inc. , 3-rd Ed., Vol. IV, Ch. 13 (2010)

Hao F., Nehl C. L., Hafner J. H., and Nordlander P., "Plasmon Resonances of a Gold Nanostar", Nano Letters, Vol. 7, No. 3, 729-732, (2007)

Hecht E., "Optics", Pearson Education, 2002

Hu Z., Fischbein M.D., Querner C., and Drndic M., Electric-Field-Driven Accumulation and Alignment of CdSe and CdTe Nanorods in Nanoscale Devices, Nano Letters, Vol. 6, No. 11, 2585-2591, (2006)

Huang X, Neretina S, and El-Sayed M.A., (2009), Adv. Mater., 21, 4880–4910

Huang, X., El-Sayed, I. H., Qian, W. and El-Sayed, M.A., "Cancer Cell Imaging and Photothermal Therapy in the Near-Infrared Region by Using Gold Nanorods", J. Am. Chem. Soc. 128, 21152120, (2006)

Hutter E. & Fendler J.H., ''Expoitation of Localized Surface Plasmon Resonance'', Adv. Mater. 16, No.19, 2004;

Johnson P.B. and Christy R.W., "Optical Constants of the Noble Metals", Phys. Rev. B 6, 4370–4379, (1972)

Kittel C., (2005) "Introduction to Solid state physics", John Wiley & Sons, Inc.
Sönnichsen C., Franzl T., Wilk T., von Plessen G., and Feldmann J., (2002), Physical Review Letters, Vol 88, Nr 7, (5)

Klar T., Perner M., Grosse S., von Plessen G., Spirkl W., and Feldmann J., "Surface-Plasmon Resonances in Single Metallic Nanoparticles", Physical Review Letters, Vol. 80, 19, 4249-52, (1998)

Kreibig U., Gartz M., Hilger A. and Neuendorf R., "Interfaces In Nanostructures: Optical Investigations On Cluster-Matter", NanoStructured Materials, Vol. 11, No. 8, pp. 1335 (1999)

Kreibig U., "Interface-Induced Dephasing Of Mie Plasmon Polaritons", Appl Phys B 93: 79 (2008)

Kreibig U. and Vollmer M., "Optical properties of metal clusters", Springer-Verlag Berlin Heidelberg p. 22, (1995)

Kumar P.S., Santos P.I., Gonzalez B.R, de Abajo F J G and Liz-Marzan L.M., High-yield synthesis and optical response of gold nanostars, Nanotechnology, 19, doi:10.1088/0957-4484/19/01/015606, 1-5, 2008

Kumar R., Singh A.P., Kapoor A., Tripathi K.N., (2004) SPIE Proceedings, Optical Engineering 43(09), Vol. 43, 2134-2142, September

Li J., Liu S., Liu Y., Zhou F., and Lia Z-Y.," Anisotropic and enhanced absorptive nonlinearities in a macroscopic film induced by aligned gold nanorods", Applied Physics Letters 96, 263103-1 (2010)

Link S., Mohamed M. B., and El-Sayed M. A., "Simulation of the Optical Absorption Spectra of Gold Nanorods as a Function of Their Aspect Ratio and the Effect of the Medium Dielectric Constant" J. Phys. Chem. B, 103, 3073 (1999)

Link S. and El-Sayed M. A., "Additions and Corrections", J. Phys. Chem. B, Vol. 109, No. 20, 10531, (2005)

Liu M. and Guyot-Sionnest P., "Synthesis and Optical Characterization of Au/Ag Core/Shell Nanorods", J. Phys. Chem. B, 108, 5882-5888, (2004)

Liu Y., Mills E.N. Composto R.J., Tuning optical properties of gold nanorods in polymer films through thermal reshaping, (2009), J. Mater. Chem., 19, 2704–2709

Maier S.A., "Plasmonics: fundamentals and applications", Springer-Verlag New York, LLC, p.11, (2007)

Mieszawska A.J., Slawinski G.W, and Zamborini F.P., Directing the Growth of Highly Aligned Gold Nanorods through a Surface Chemical Amidation Reaction, J. Am. Chem. Soc., 128, 5622-5623(2006),

Mohr F., editor, “Gold Chemistry - Applications and Future Directions in the Life Sciences”, Wiley-VCH, p. 327, 2009

Murphy C. J., Sau T.K., Gole A.M., Orendorff C.J., Gao J., Gou L., Hunyadi S.E., and Tan Li (2005), J. Phys. Chem. B, 109, 13857-13870

Myroshnychenko V., -Fernandez J. R., Santos I.P., Funston A. M., Novo C., Mulvaney P., Liz-Marzan L.M. and F. Javier Garcıa de Abajo, Modeling the optical response of gold nanoparticles, Chem. Soc. Rev., 2008, 37, 1792–1805, DOI: 10.1039/b711486a

Noguez C., ”Surface Plasmons on Metal Nanoparticles: The Influence of Shape and Physical Environment”, J. Phys. Chem. C, 111, 3806-3819, (2007)

Novo C., Gomez D., Perez-Juste J., Zhang Z., Petrova H., Reismann M., Mulvaney P. and Hartland G. V., “Contributions from radiation damping and surface scattering to the linewidth of the longitudinal plasmon band of gold nanorods: a single particle study”, Phys. Chem. Chem. Phys., 8, 3540–3546, (2006)

Padilha L.A., Fontana J, Kohlgraf-Owens D, Moreira M, Webster S, Palffy-Muhoray P, Kik P.G, Hagan D. J, and Van Stryland E.W., “Linear and Nonlinear Optical Response of Aligned Gold Nanorods”, OSA/CLEO/IQEC, (2009)

Pelton M., Liu M., Park S., Scherer N. F., and Guyot-Sionnest P., Physical Review B 73, 155419 (2006)

Perez-Juste J., Pastoriza-Santos I., Liz-Marzan L. M., Mulvaney P., (2005), Optical control and patterning of gold-nanorods-poly(vinyl alcohol) films, Adv. Funct. Mater., 15, 1065-1071

Perez-Juste J., Pastoriza-Santos I., Liz-Marzan L. M., Mulvaney P., “Gold nanorods: Synthesis, characterization and applications”, Coordination Chemistry Reviews 249, 1870–1901, (2005)

Pollack G.L. and Stump D.R., “Electromagnetism”, (2002), Pearson Education Inc.

Prodan E. and Nordlander P., “Structural Tunability of the Plasmon Resonances in Metallic Nanoshells”, Nano Letters, Vol. 3, No. 4, 543-547, (2003)

Rodrıguez-Lorenzo L., Alvarez-Puebla R.A., Pastoriza-Santos I., Mazzucco S., Stephan O., Kociak M., Liz-Marzan L.M., and Garcıa de Abajo F. J., “Zeptomol Detection Through Controlled Ultrasensitive Surface-Enhanced Raman Scattering”, J. Am. Chem. Soc. 2009, 131, 4616–4618

Sabatini D. editor, “Leading edge nanotechnology. Research developments”, Nova Science Publishers Inc., 2007

Sandu T., (2012), Springer Science+Business Media B.V. 2012, J. Nanopart. Res. 14:905

Steele J.M., Grady N.K., Nordlander P. and Halas N.J., "Plasmon Hybridization in Complex Nanostructures", in "Surface Plasmon Nanophotonics" by Brongersma M. L. & Kik P. G. (eds), Springer, p. 183, 2007

Sönnichsen C., Franzl T., Wilk T., von Plessen G., Feldmann J., Wilson O. and Mulvaney P., "Drastic Reduction of Plasmon Damping in Gold Nanorods", Physical Review Letters, Vol 88, Nr 7, (2002)

Taflove A. and Hagness S.C.," Computational Electrodynamics: The Finite-Difference Time-Domain Method", Norwood, MA: Artech House, 2005

Thulstrup E.W., Thulstrup P.W., "Polarization Spectroscopic Studies of Ordered Samples", Acta Chim. Slov., 52, 371–383, (2005)

Torres J. M., Bakken N., C.M. Stafford, Jian Li and Bryan D. Vogt, Thickness dependence of the elastic modulus of tris(8-hydroxyquinolinato)aluminium, Soft Matter, 2010, 6, 5783–5788.

Trigari S., Alessio Rindi, Giancarlo Margheri, Stefano Sottini, Giovanna Dellepiane and Emilia Giorgettia, Synthesis and modelling of gold nanostars with tunable morphology and extinction spectrum, J. Mater. Chem., 21, 6531- 6540, 2011

Truong V.V. and Scott G. D., "Optical constants of aggregated gold films", J. Opt. Soc. Am., Vol. 66, No. 2, (1976)

van der Zande B. M. I., Page L, Hikmet R.A.M., van Blaaderen A, (1999), "Optical Properties of Aligned Rod-Shaped Gold Particles Dispersed in Poly(vinyl alcohol) Films", J. Phys. Chem. B, 103, 5761-5767, (1999)

van der Zande B. M. I., Koper G. J. M., and Lekkerkerker H.N.W., (1999), Alignment of Rod-Shaped Gold Particles by Electric Fields, J. Phys. Chem. B, 103, 5754-5760

Zhang, Z., Wang, J., Chen C., "Gold Nanorods Based Platforms for Light-Mediated Theranostics", Theranostics, Vol. 3, Issue 3, 223-238, (2013)

Zhu J., Bai S-W., Zhao J-W., Li J-J, "Tunable optical limiting of gold nanorod thin films", Appl. Phys. A 97: 431–436, (2009)

Zhukov V. P., Chulkov E. V. and Echenique P. M., "Lifetimes and inelastic mean free path of low-energy excited electrons in Fe, Ni, Pt, and Au: Ab initio GW+T calculations", Phys. Rev. B, 73, 125105, (2006).

Yan B., Yang Y., and Wang Y., "Comments", J. Phys. Chem. B, 107, 9159, (2003)

Yee, K.S., “Numerical solution of initial boundary value problems involving Maxwell’s equations in isotropic media”, IEEE transactions on antennas and propagation, Vol. AP-14, no. 3, 1966

Yu C. and Irudayaraj J., (2007), Biophysical Journal, Volume 93, 3684–3692

Yuan H., Khoury C., Hwang H, Wilson C. M., Grant G. A and Vo-Dinh T, “Gold nanostars: surfactant-free synthesis, 3D modelling, and two-photon photoluminescence imaging”, Nanotechnology 23, 075102 (9pp) (2012)

Wang X., Neff C., Zijlstra P., Chon J. W. M., Gu M., ” Five-dimensional optical recording mediated by surface plasmons in gold nanorods”, Nature, Vol 459, 410-413, (2009)

Wang Y., Teitel S., Dellago C, (2005), Nano Letters, Vol. 5, No. 11, 2174-2178

Willets, K. A. and Van Duyne, R. P., “Localized Surface Plasmon Resonance Spectroscopy and Sensing”, Annu. Rev. Phys. Chem. **58**:267-297 (2007).

Wilson O., Wilson G.J.and Mulvaney P., “Laser Writing in Polarized Silver Nanorod Films”, Adv. Mater. 14, No. 13 (2002)